

Molecular Electronics

20010226036

DISTRIBUTION STATEMENT A
Approved for Public Release
Distribution Unlimited

MATERIALS RESEARCH SOCIETY
SYMPOSIUM PROCEEDINGS VOLUME 582

Molecular Electronics

Symposium held November 29–December 2, 1999, Boston, Massachusetts, U.S.A.

EDITORS:

Sokrates T. Pantelides
Vanderbilt University
Nashville, Tennessee, U.S.A.

Mark A. Reed
Yale University
New Haven, Connecticut, U.S.A.

James S. Murday
Naval Research Laboratory
Washington, D.C., U.S.A.

Ari Aviram
IBM T.J. Watson Research Center
Yorktown Heights, New York, U.S.A.



Materials Research Society
Warrendale, Pennsylvania

20010226 036

This work was supported in part by the Office of Naval Research under Grant Number
ONR: N00014-00-1-0143. The United States Government has a royalty-free license throughout
the world in all copyrightable material contained herein.

Single article reprints from this publication are available through
University Microfilms Inc., 300 North Zeeb Road, Ann Arbor, Michigan 48106

CODEN: MRSPDH

Copyright 2001 by Materials Research Society.
All rights reserved.

This book has been registered with Copyright Clearance Center, Inc. For further information, please
contact the Copyright Clearance Center, Salem, Massachusetts.

Published by:

Materials Research Society
506 Keystone Drive
Warrendale, PA 15086
Telephone (724) 779-3003
Fax (724) 779-8313
Web site: <http://www.mrs.org/>

Library of Congress Cataloging-in-Publication Data

Molecular electronics / editors Sokrates T. Pantelides, Mark A. Reed, James S. Murday, Ari Aviram
p.cm.—(Materials Research Society symposium proceedings,
ISSN 0272-9172 ; v. 582)
Includes bibliographical references and indexes.
ISBN 1-55899-490-4
1. Molecular electronics. I. Pantelides, Sokrates T. II. Reed, Mark A. III. Murday, James S. IV. Aviram, Ari V. Materials Research Society symposium proceedings ; v. 582
TK7874.8 .M6533 2000
621.381—dc21 00-053384

Manufactured in the United States of America

CONTENTS

Preface	vii
Abstracts	ix
Materials Research Society Symposium Proceedings	xx
Organometallic Synthesis And Spectroscopic Characterization	
Of Manganese Doped CdSe Nanocrystals.....	H2.4
F.V. Mikulec, M. Kuno, M. Bennati, D.A. Hall, R.G. Griffin, and M.G. Bawendi	
Artificial Atoms Of Silicon	H2.5
J.D. Holmes, K.J. Ziegler, K.P. Johnston, R.C. Doty, and B.A. Korgel	
Room Temperature Negative Differential Resistance In	
Nanoscale Molecular Junctions.....	H3.2
J. Chen, W. Wang, M.A. Reed, A.H. Rawlett, D.W. Price, and J.M. Tour	
*Transport Calculations In Molecular Devices From	
First Principles	H3.3
M. Di Ventra, N.D. Lang, and S.T. Pantelides	
*Electronic Structure Of Organic/Metal Interfaces Studied	
By UPS And Kelvin Probe.....	H6.4
K. Seki, H. Oji, E. Ito, D. Yoshimura, N. Hayashi, Y. Ouchi, and H. Ishii	
*Molecular Scale Electronics	H9.2
A.M. Rawlett, E.T. Mickelson, W.A. Reinerth, L. Jones II, M. Kozaki, T.P. Burgin, J.M. Tour, J. Chen, C-W. Zhou, C.J. Muller, M.R. Deshpande, M.A. Reed, L.A. Bumm, M.T. Cygan, T.D. Dunbar, P.S. Weiss, and D.L. Allara	
End-Grafted Semiconducting Polymer–Candidate	
For Molecular Wire	H10.2
K. Furukawa, K. Ebata, and M. Fujiki	
Fabrication And Transport Properties Of Te-Doped	
Bi Nanowire Arrays	H10.3
Y.M. Lin, X. Sun, S.B. Cronin, Z. Zhang, J.Y. Ying, and M.S. Dresselhaus	

*Invited Paper

Transport Measurements Of Individual Bi Nanowires..... H10.4
S.B. Cronin, Y.M. Lin, T. Koga, J.Y. Ying, and M.S. Dresselhaus

**Plasmonics: Electromagnetic Energy Transfer And Switching
In Nanoparticle Chain-Arrays Below The Diffraction Limit..... H10.5**
M.L. Brongersma, J.W. Hartman, and H.H. Atwater

**Nanoscale Patterns Of Metal Nanoparticles Chemically-Assembled
On Biomolecular Scaffolds: Assembly, Stability And Electron
Transport Properties** H11.1
J.E. Hutchison, L.O. Brown, J.L. Mooster, S.M. Reed, M.E. Schmidt,
L.I. Clarke, and M.N. Wybourne

**Synthesis Of Ultra-Small Si Nano Particle Colloids And Thin
Films-High Temperature Single Electronics** H11.4
J.M. Therrien, G. Belomoin, and M.H. Nayfeh

**Unimolecular Electrical Rectification Down To 105 K, And
Spectroscopy Of Hexadecylquinolinium Tricyanoquinodimethanide..... H12.2**
R.M. Metzger

Fabrication Methods For Au Nanocluster Devices H12.5
A.W. Snow, M.G. Ancona, W. Kruppa, D. Park, J.B. Boos,
and G.G. Jernigan

**Room Temperature Single Electron Charging In Gold
Nanoparticle Networks Formed On Biopolymer Templates..... H13.4**
M.N. Wybourne, L. Clarke, C.A. Berven, J.E. Hutchison,
L.O. Brown, and J.L. Mooster

Author Index

Subject Index

PREFACE

This volume contains papers presented at Symposium H, "Molecular Electronics," held November 29–December 2 at the 1999 MRS Fall Meeting in Boston, Massachusetts.

As Si-based microelectronics marches to ever-smaller feature sizes, the point is rapidly approaching when conventional MOSFETs will no longer operate. Such devices depend on the concept of "doped regions" which can be envisioned to be ever so small until you get to the point where there is only a handful of dopant atoms. Tunneling across ultra-thin films is another major issue.

Single molecules as active device elements is a concept that goes back to the 1970's, but in recent years very substantial progress has been made in synthesizing molecules suitable for such purposes. Carbon nanotubes have been a prime candidate for both nanowires and active devices. Molecules as small as single benzene rings, and larger, more complex molecules have been synthesized and measured, showing reproducible current-voltage characteristics. Unusual features are large negative differential resistance and large shifts of resonant peaks as functions of temperature.

The symposium featured many invited talks and a fair number of contributed talks; unfortunately many of the invited speakers did not contribute a paper to the proceedings. The interested reader may refer to relevant recent journals where original publications can be found.

The Symposium was extremely well attended by overflow crowds to the point that a closed-circuit TV had to be setup in an adjacent room. It was a very diverse audience, mainstream Si engineers, chemists, physicists, materials scientists—it was a truly interdisciplinary celebration of an exciting emerging field.

We gratefully acknowledge support from the Office of Naval Research.

Sokrates T. Pantelides
Mark A. Reed
James S. Murday
Ari Aviram

September 2000

SESSION H1:
Chair: Sokrates T. Pantelides
Monday Morning, November 29, 1999
Cape Cod/Hyannis (M)

8:30 AM *H1.1
OPPORTUNITIES FOR MOLECULAR ELECTRONICS IN HIGH-PERFORMANCE COMPUTER SYSTEMS. Rick Lyle, Howard Davidson, Nyles Nettleton, Sun Microsystems, Palo Alto, CA.

Silicon-based VLSI continues to scale to smaller dimensions and higher performance. This scaling should continue for about ten more years. At that point, new approaches for designing and fabricating CPU and memory devices will be required. This opens the door for the introduction of new technologies based upon molecular chemistry and solid-state physics. But such opportunities exist now in select areas, such as large, fast cache memories. This talk will review the scaling behavior of modern computer systems, will describe opportunities for molecular electronics within the next decade of Silicon scaling, and will examine possible designs for future computing machines based upon molecular electronics.

9:00 AM *H1.2
WIRES, SWITCHES, AND WIRING: TOWARD A CHEMICALLY ASSEMBLED ELECTRONIC NANOCOMPUTER. J. Heath, Dept. of Chemistry and Biochemistry, University of California at Los Angeles, Los Angeles, CA.

Researchers at UCLA, Hewlett Packard, and UC Berkeley have begun to fabricate a molecular based computational machine. Architectural schemes and rationale for this machine will be presented. The fabrication and characterization of electronically configurable logic gates and logic circuits based on molecular-scale switches and nano-scale wires will be presented. Fundamental issues related to these devices will be discussed, including interface issues, switching times, and molecular structure optimization.

9:30 AM *H1.3
NANOTUBE DOTS, WIRES, AND CROSSES. Paul L. McEuen, Dept. of Physics, Univ. of Calif. -Berkeley, and Materials Sciences Division, LBNL.

Carbon nanotubes are a new class of one-dimensional conductors that can be either metallic or semiconducting, depending upon their structural details. In this talk, I will discuss experiments to probe the electrical properties of these fascinating systems. Wires are attached to individual tubes and a nearby gate is used to control the charge per unit length of the tube. If the tube is semiconducting, the device operates as the world's smallest transistor. For a metallic tube, a correlated electron state known as a Luttinger liquid is found. Short tubes act like one-dimensional quantum dots whose discrete energy levels and spin states can be probed. Crossed metal and semiconducting tubes act as ultra-small Schottky diodes. As these experiments show, nanotubes offer an unprecedented opportunity to explore the physics and technology of 1D conductors.

SESSION H2:
Chair: Sandra J. Rosenthal
Monday Morning, November 29, 1999
Cape Cod/Hyannis (M)

10:30 AM *H2.1
NANOCRYSTALS AS BUILDING BLOCKS FOR ELECTRICAL DEVICES. Paul Alivisatos, Univ. of California, Berkeley, Dept of Chemistry, Berkeley, CA.

Nanometer size crystals of inorganic semiconductors display a wealth of size dependent optical and electrical characteristics. Such nanocrystals (CdS, CdSe, InP, InAs), with well controlled interfaces, can now be fabricated by colloidal chemistry techniques. The resulting particles are extremely flexible chemically, and may be thought of as a class of molecule. These nanocrystals can in turn be incorporated into electrical devices. Three examples will be described: LEDs, photovoltaics, and single nanocrystal transistors. Finally, efforts will be described to use biological molecules, such as DNA, to design complex patterns of nanocrystals.

11:00 AM H2.2
ELECTRONIC TRANSPORT IN COLLOIDAL CdSe QUANTUM DOT ARRAYS. N.Y. Morgan, I. Praaad, M.A. Kastner, M.I.T., Dept. of Physics, Cambridge, MA; C.A. Leatherdale, M.G. Bawendi, M.I.T., Dept. of Chemistry, Cambridge, MA.

We present results for dark current measurements on large close-packed arrays of CdSe nanocrystals. The nanocrystals are

chemically synthesized in solution and then deposited between gold electrodes onto a silicon substrate which has a 350 nm oxide grown on its surface. The Si substrate is degenerately doped and can be used as a gate. In response to an applied voltage step, we observe a power-law decay of the current over five orders of magnitude in time and four orders of magnitude in current. Furthermore, we do not observe a steady-state dark current for fields up to 1×10^8 V/cm and times out to 5×10^4 seconds. We see clear evidence for the injection of electrons into the array, but do not observe hole injection. The number of electrons in the array can be increased by cooling the sample with a positive gate voltage. However, as the number of electrons is increased, the magnitude of the current transient decreases substantially. We believe our results can be understood in the context of the Coulomb glass model, where transport is dominated by the long-range electrostatic interactions between electrons at different sites.

11:15 AM H2.3
PRESSURE-INDUCED INTERDOT INTERACTIONS IN CdSe NANOCRYSTAL ARRAYS. Boaeng Kim, Mohammad A. Islam, Louis E. Brus and Irving P. Herman, Columbia Radiation Laboratory, Columbia University, New York, NY.

Three-dimensional arrays of organically-passivated CdSe nanocrystals were investigated under hydrostatic pressure using photoluminescence and absorption spectroscopy. In some arrays, such as those composed of CdSe dots capped by tri-n-octylphosphine oxide, the first excitonic level of the absorption spectrum monotonically moves to the blue with increasing pressure until the structural phase transition is reached, reflecting the increasing band gap of bulk CdSe and the increasing confinement energy. This dependence was also seen in dilute solutions of CdSe nanocrystals. For arrays composed of CdSe dots capped with some smaller molecules, the energy of the first excitonic peak in absorption does not increase with pressure above ~ 40 kbar. This may be evidence of interdot coupling. This work was supported by the MRSEC Program of the National Science Foundation under Award Number DMR-9809687 and the JSEP Program under Contract No. DAA-G55-97-1-0166.

11:30 AM H2.4
ORGANOMETALLIC SYNTHESIS AND SPECTROSCOPIC CHARACTERIZATION OF Mn DOPED CdSe NANOCRYSTALS. Frederic V. Mikulec, Masaru Kuno, Moungi G. Bawendi, MIT, Dept. of Chemistry, Cambridge, MA; Marina Bennati, Dennis A. Hall, Robert G. Griffin, MIT, Dept. of Chemistry and Center for Magnetic Resonance, Francis Bitter Magnet Laboratory, Cambridge, MA.

The synthesis of II-VI semiconductor nanocrystals doped with transition metals has proved to be particularly difficult. In the case of CdSe quantum dots produced via high temperature pyrolysis in tri-n-octylphosphine oxide (TOP), specially designed precursors used in this study appear to be necessary to successfully incorporate low levels of Mn. Combining a simple etching experiment and electron paramagnetic resonance (EPR) measurements reveals that most of the dopant atoms reside inside the surface layers of the inorganic lattice. The dopant dramatically affects Cd-113 magic angle spinning (MAS) NMR spectra; the observed paramagnetic shift and decreased longitudinal relaxation time reproduce bulk material behavior. Results from fluorescence line narrowing (FLN) studies on Mn doped CdSe nanocrystals mirror previous findings on undoped nanocrystals in an external magnetic field. Experimental fitting of photoluminescence excitation (PLE) spectra of doped nanocrystals reveals that the effective absorption lineshape contains a new feature which is believed to be a previously unobserved - but theoretically predicted - optically dark fine structure state.

11:45 AM H2.5
ARTIFICIAL ATOMS OF SILICON. Justin D. Holmes, Kirk Ziegler, Keith P. Johnston, Chris Doty, Brian A. Korgel, Dept of Chemical Engineering and the Texas Materials Institute, The University of Texas, Austin, TX.

Highly size monodisperse, sterically-stabilized silicon nanocrystals ~ 13 Å in diameter were synthesized using a new solution-phase synthetic approach that utilizes a capping solvent heated and pressurized above its critical point to control particle growth. The precursor diphenylsilane was thermally degraded in octanol at temperatures (773 K) and pressures (340 atm) well above the critical point for octanol: 34 atm and 658 K. These nanocrystals represent the first examples of silicon artificial atoms that exhibit discrete optical transitions in the room temperature absorbance and photoluminescence excitation spectra with efficient band edge photoemission (quantum yield = 23%). Infra-red and chemical ionization mass spectroscopies indicate that the stabilizing C8 hydrocarbon chains bind to surface-exposed silicon atoms through an Si-O-C link at the particle surface. These silicon clusters, on the lower size limit, reveal that silicon does not undergo the transition to a direct band gap semiconductor and furthermore, that excitons in

these very small clusters remain strongly coupled to phonons, resulting in broad luminescence at room temperature.

SESSION H3:
Chair: Norton D. Lang
Monday Afternoon, November 29, 1999
Cape Cod/Hyannis (M)

1:30 PM *H3.1
NANOASSEMBLED SELF-ASSEMBLED MONOLAYERS FOR MOLECULAR ELECTRONICS. Chongwu Zhou, M.R. Deshpande and M.A. Reed, Dept of Electrical Engineering, Yale University, New Haven, CT; L. Jones II, J. Seminario and J.M. Tour, Dept of Chemistry, Univ of South Carolina, Columbia, SC.

The measurements of electronic transport in organic molecular wires are experimentally challenging and intriguing. We present the investigation of novel metal / self-assembled monolayer of molecular wires / metal heterostructures with nanoscale device areas. Diode-like I-V characteristics is observed for devices consisting of 4-thioacetyl biphenyl and variable temperature measurements reveals the transport mechanism. A sharp decrease in conductivity is observed around 35 K for devices consisting of molecules with triple bonds in the conjugated backbone. Theoretical simulations suggest it can be explained through thermally excited bond rotations at the triple bonds. Results with other molecules will also be presented.

2:00 PM H3.2
NEGATIVE DIFFERENTIAL RESISTANCE IN NANOSCALE MOLECULAR JUNCTIONS. Jia Chen, Mark A. Reed, Yale University, Dept of Electrical Engineering, New Haven, CT; Adam M. Rawlett, James M. Tour, Rice University, Center for Nanoscience and Technology, Houston, TX.

We report the first observations of negative differential resistance (NDR) with giant peak-to-valley ratio (PVR) in nanoscale molecular junctions. We have measured a record 1000:1 PVR in a 1-thioacetyl-4-(4-(phenylethynyl)-2-aminino-5-nitro-1-(ethynyl) phenyl) benzene self-assembled monolayer (SAM) between metal contacts. Variable temperature measurements show that the junction develops NDR below 320 K, reaching a maximum negative differential conductivity of .5 Ks / cm² at 2 V, and an associated PVR of 1000:1 at 60 K. The role of the internal redox dipole of the molecule on the conduction, and methods to engineer the operation for 300 K, will be discussed. The device exhibits the largest PVR known for any structure with useful (>> kT) operating voltages.

2:15 PM *H3.3
TRANSPORT CALCULATIONS IN MOLECULAR DEVICES FROM FIRST-PRINCIPLES. M. Di Ventra¹, N.D. Lang², and S.T. Pantelides¹; ¹Department of Physics and Astronomy, Vanderbilt University, Nashville, TN; ²IBM Research Division, Thomas J. Watson Research Center, Yorktown Heights, NY.

For molecular electronics, Boltzmann's equation is no longer valid for simulating device characteristics. We present the first fully ab-initio simulation of a molecular device that has already been studied experimentally by Reed et al. [1], namely a benzene-1,4-dithiolate molecule between gold electrodes. The theoretical I-V curve has the same overall shape as the experimental curve - reflecting the electronic structure of the molecule in the presence of the electric field - but the absolute value of the current is very sensitive to contact chemistry and geometry. In particular the presence of a single gold atom between the molecule and the electrode surface reduces the conductance by about two orders of magnitude. Replacement of the single gold atom by an aluminum atom, whose p orbitals couple more effectively to the molecule's p orbitals, increases the conductance by about an order of magnitude. We also show the polarization induced by a third terminal (gate) on the above device. Current gain due to the gate bias can be achieved at reasonable gate fields. Finally, the effect of current-induced forces on the device will be discussed. [1] M.A. Reed et al., Science 278, 252 (1997)

Work supported in part by DARPA.

2:45 PM H3.4
ELECTRICAL TRANSPORT MEASUREMENTS THROUGH A METAL-MOLECULE(S)-METAL JUNCTION. J.P. Bourgoin¹, C. Kergueris¹, S. Palacín¹, D. Esteve², C. Urbina², M. Magoga³, C. Joachim³, ¹Service de Chimie Moléculaire, CEA Saclay, FRANCE; ²Service de Physique de l'Etat Condensé, CEA Saclay, FRANCE; ³SCEMES/LOE CNRS Toulouse, FRANCE.

In order to measure the transport properties of molecules we have used microfabricated break junctions as metallic tweezers with a nanometer scale adjustable gap. [1] Specifically designed molecules,

bisthiololigothiophene in particular, were self-assembled in the gap to form metal-molecule(s)-metal junctions. The current-voltage characteristics recorded at room temperature are non-linear with step-like features and can be strongly modified by gap size changes of 0.4 Å [2]. These results can be qualitatively accounted for by a model which assumes that a single molecule is involved and that takes explicitly into account its discrete electronic levels. Finally, we will compare theoretically thiol and isocyanide binding groups in terms of their electrical transport efficiency. [1] M.A. Reed, C. Zhou, C.J. Muller, T.P. Burgin, J.M. Tour, Science 5336 (1997) 252 [2] C. Kergueris, J.P. Bourgoin, S. Palacín, D. Esteve, C. Urbina, M. Magoga, C. Joachim, Phys. Rev. B 59 (1999) 12505

SESSION H4:
Chair: Mark A. Reed
Monday Afternoon, November 29, 1999
Cape Cod/Hyannis (M)

3:30 PM H4.1
NANOMETER SIZED GAPS IN METALLIC WIRES. M. Radosavljevic, J. Lefebvre, A.T. Johnson, Dept. of Physics, University of Pennsylvania, Philadelphia, PA.

We report on the details of a new method for production of nanometer sized breaks (nanogaps) in metallic wires. Our method, based on standard lithographic techniques, offers possibility of parallel production in an industrial setting. In addition, we can accurately tune the size of individual nanogaps: from 100nm to below 5nm. Such small separations exceed the limits of conventional electron beam lithography, and compare favorably to other, more involved, schemes. Preliminary spectroscopic data on SWNTs bridging a nanogap are presented and analyzed in the single electron charging picture.

3:41 PM H4.2
NANOELECTRODE FABRICATION AND SELF-ASSEMBLY OF SINGLE ELECTRON TRANSISTOR. Magnus Persson, Linda Olsson, Chalmers University of Technology, Dept. of Microelectronics and Nanoscience, Gothenburg, SWEDEN; Charles M. Marcus, Alberto Morpurgo, Stanford University, Dept. of Physics, CA.

Angle evaporation and controlled electrodeposition of electrodes have been used to fabricate very small well-defined gaps between two gold electrodes. The size of the gap can be controlled between 1-10 nm or less, which is much smaller than one could achieve by only using angle evaporation and lift-off technique. The conductance is measured during the process and conductance quantization is observed indicating nanobridges with only single or few gold atoms. The electrodes have been used for connecting ligand stabilized gold clusters, with 2-5 nm diameter, which are self-assembled in the electrode gap. Coulomb blockade was observed at room temperature and single electron transistor effect was observed at 4.2 K, in such devices. The well-controlled gap can also be used for contacting self-assembling conducting oligomers. The electrodes are made on thin Silicon-nitride membranes and are studied with a transmission electron microscope.

4:00 PM *H4.3
STM PROBING OF QUANTUM AND MOLECULAR MECHANICS OF INDIVIDUAL MOLECULES. James K. Gimzewski, IBM Research Division, Zurich Research Laboratory, SWITZERLAND.

On the scale of individual molecules adsorbed on surfaces both mechanics and quantum effects combined with thermal fluctuations can play a determining role in their electronic transport properties and their dynamics. These effects, rather than limit future electronic devices, may provide unique opportunities to design and build new machines. The nanoscale science underlying electronic and mechanical properties of single molecules is at an early stage of development. Nevertheless the capabilities of designer chemical synthesis opens new opportunities to design experiments within a single molecule. In this talk we will discuss two molecules that were designed to: (1) Understand the role of a molecule in extending a metallic wavefunction and thereby providing electrical conduction at low voltages and (2) Demonstrate the rotation of a single molecule operating within a supramolecular bearing. We extend both of these concepts with a new proposal for a type of electronic device that utilises quantum electronic transport modulated by Brownian rotation fluctuations. The redirection of the fluctuations is achieved by the application of either coloured noise or by an external static perturbation.

4:30 PM *H4.4
THE CONDUCTANCE OF A MOLECULAR WIRE. Christian Joachim, University of Toulouse, CEMES-CNRS, Toulouse, FRANCE.

The conductance of a molecular wire is a decreasing exponential function of its length. This defines the tunnel transport regime where the homo-lumo gap of the molecular wire is different from zero and the I-V characteristic is linear at low voltage. We will first show how to optimize the chemical structure of the molecular wire to reach a tunneling inverse damping length lower than 0.1 Ång-1. Then, we will report an STM experiment to measure this damping length on molecular wires 0.3 nm in width, 1.4 and 4 nm in length in a planar configuration using the STM tip like a stub scanned along the molecular wire. The properties of intramolecular circuits will be discussed in conclusion.

SESSION H5:
Chair: Bruce E. Gnade
Tuesday Morning, November 30, 1999
Cape Cod/Hyannis (M)

8:30 AM H5.1
NOVEL STRATEGIES FOR PREPARATION OF ORDERED ARRAYS OF ORGANIC MOLECULES ON SEMICONDUCTOR SURFACES. Robert J. Hamers, University of Wisconsin, Dept. of Chemistry, Madison, WI.

We have developed a new strategy for forming ordered, oriented organic layers on (001) surfaces of group IV semiconductors. Our strategy is based on the transfer of directional bonding from a solid inorganic substrate into an attached array of organic molecules. Si(001), Ge(001), and C(001)(diamond) surfaces consist of Si=Si, Ge=Ge, or C=C dimers, with the atoms within each dimer held together by a strong sigma and weak pi bond. Unsaturated organic compounds (containing one or more double or triple bonds) occurs rapidly on these surfaces, producing well-defined, atomically-sharp organic-inorganic interfaces. One important property of organic layers formed using this chemistry is that the molecules are oriented. This orientation arises because the bonding of the molecule to the surface involves two bonds; thus, the orientation of the Si=Si dimers of the underlying substrate is transferred into the orientation of the organic monolayer films. The orientation of the surface dimers can be controlled by using vicinal surfaces. For example, on silicon (001) miscut by 4 degrees toward <110>, a single domain surface is formed in which all the dimers are aligned along the same direction; the molecules in the organic film are also therefore aligned. The alignment of organic molecules provides anisotropy in their physical properties such as optical absorption and, in principle, electrical conductivity. STM measurements of the apparent height of individual molecules also provides insight into the mechanisms of electrical conductivity and the effects of various substituent groups on transport properties. By understanding the chemistry of the attachment process, one can control the selectivity of the reaction toward particular functional groups; this permits the formation of novel structures that may have unusual chemical, optical and/or electrical properties by virtue of their spatial orientation. This talk will discuss our recent efforts at fabrication of highly-controlled organic monolayers and the characterization of these layers using atomic-resolution Scanning Tunneling Microscopy, infrared vibrational spectroscopy, and x-ray photoelectron spectroscopy. Prospects for use of these layers in molecular electronics and molecular optics will be presented.

9:00 AM H5.2
STM-INDUCED PHOTON EMISSION FROM SINGLE PORPHYRIN MOLECULES ON Cu(100). Z.-C. Dong, T. Ohgi, D. Fujita, T. Yakabe, H. Nejoh, T. Terui, S. Yokoyama, M.-N. Zhou, S. Mashiko, T. Okamoto, Natl Research Inst for Metals, Ultrahigh Vacuum Station, Tsukuba, JAPAN.

Positioning of a scanning tunneling microscopy tip above a single Cu-TBP porphyrin molecule on Cu(100) was found to induce photon emission when electrons are injected and bias voltages are above ± 2 V. The emitted light appears orange by the naked eyes, in agreement with a broad spectral peak around 660 nm. Amazingly, this broad peak features several shoulder-peaks with a peak spacing of ca. 800 cm^{-1} , an implication of the fine structure related to the vibrational excitation of the molecule. The intensity of light emission is measured to be about 10^{-9} cps, resulting in a quantum efficiency in the order of 10^{-3} . A new approach for producing strong light emission with control will be proposed.

9:15 AM H5.3
FABRICATION AND CHARACTERIZATION OF MONOMOLECULAR SIGMA/PI HETEROSTRUCTURES. J. Collet, S. Lenfant, D. Vuillaume, Institut d'Electronique et de Micro-Électronique du Nord, CNRS, Villeneuve d'Ascq, France. O. Boulouss, F. Rondelez, Physicochimie Curie, Institut Curie, CNRS, Paris, FRANCE; J.M. Gay, Centre de Recherche sur les Mécanismes de la Croissance Crystalline, CNRS, Marseille, FRANCE; K. Khan, C. Chevrot, Laboratoire de Recherche sur les Polymères et Matériaux

Electro-actifs, Univ. Cergy-Pontoise, FRANCE.

Molecular-scale Electronics is envisioned as a promising bottom-up strategy to nanoscopic electronic devices. The use of self-assembly technique is an invaluable strategy to fabricate such structures. Self-assembled monolayers (SAM) of saturated alkyl chains for instance are known to present a very good insulating behavior. Here, we have used a chemical functionalization of the end-groups of such organic SAM's to fabricate insulator/semiconductor heterostructures (hereafter called sigma-pi SAM) at a molecular level. By attaching pi-electron moieties at the top of previously formed insulating monolayers, we obtain a reasonably large in-plane conductivity without hampering the insulating behavior in the perpendicular direction. The ratio between the parallel and perpendicular conductivities is found to be very large, up to 189 for s-p monolayers terminated by various pi moieties like Phenyl, Retinol, Pyrene, thiophene, anthracene and Carbazole. Two chemical routes are described to build these structures. FTIR, wettability, ellipsometry and X-ray reflectivity carefully characterized the structural properties of these SAMs before electrical measurements. The in-plane conductivities in these SAMs were analyzed versus temperature and frequency. Variations of the in-plane conductivities as function of the pi end-groups are discussed versus the size and versus the electronic structures of the pi end-groups. Nature of the conduction mechanisms will be discussed. In many proposals for molecular-scale devices, the sigma-pi interface is proposed as a way to modulate the electron transfer (blocking barrier). This concept is demonstrated here at the monolayer level. Such insulator/semiconductor heterostructures with a relatively high anisotropic conductivity open powerful opportunities to build future nanoscopic molecular devices.

9:30 AM H5.4
ELECTRONIC STRUCTURE OF THIENYLENEVINYLINE OLIGOMERS: APPLICATION TO THEIR ADSORPTION ON SILICON (100) SURFACE. C. Krzeminski, C. Delerue, G. Allan, V. Haquet, B. Grandidier, J.P. Nys, D. Stévenard, ISEM, Dept ISEN, Lille, FRANCE; P. Frère, E. Levillain, J. Roncali, Ingénierie Moléculaire et Matériaux Organiques, Université d'Angers, Angers, FRANCE.

Conjugated oligomers have attracted considerable interest as possible molecular wires. Investigation of the interaction of these molecules with the silicon (100) surface is therefore useful to gain insight into the way the oligomers could be connected to the silicon surface. We present combined experimental and theoretical studies on such a system. Theoretically, ab initio calculations based on the local density approximation and semi-empirical tight binding calculations are applied to thielenylenevinylene oligomers up to the hexadecamer stage ($n=16$). The results correctly describe the experimental variations of the gap versus size, the optical spectra and the electrochemical redox potentials. We propose a simple model to deduce from the band structure of the polymer chain the electronic states of the oligomers close to the gap. We analyze the evolution of the gap as a function of the torsion angle between consecutive cells: the modifications are found to be small up to a $\sim 30^\circ$ angle. We show that these oligomers possess extensive pi-electron delocalization along the molecular backbone which supports their interest for future electronic applications such as molecular wires. Experimentally, the adsorption of different thielenylenevinylenes on silicon (100) 2x1 have been studied by scanning tunneling microscopy in ultra high vacuum. The current constant images of the thielenylenevinylenes are strongly bias dependent and allow the determination of the adsorption sites. The reaction involves the thiophene ring with a single Si atom of the Si=Si dimer. Ab initio calculations are performed to better characterize the chemical nature of the bonding.

9:45 AM H5.5
SELF-ASSEMBLY GROWTH OF MOLECULAR WIRES BY MOLECULAR BEAM DEPOSITION. Chengzhi Cai, Johannes Barth, Jens Weckesser, Martin Boesch, Christian Böshard, L. Buergi, O. Jeandupeux, Peter Guenter, Klaus Kern, ETH, Inst of Quantum Electronics, Zurich, SWITZERLAND; EPFL, Inst of Experimental Physics, Lausanne, SWITZERLAND.

The combination of properly designed supramolecular assemblies and molecular beam deposition is an efficient way to fabricate nanostructures such as molecular wires for potential applications in molecular electronics. We have designed a series of supramolecular polymers in which the monomeric units are linked in a linear and head-to-tail fashion via strong hydrogen bonding. One example is 4-trans-2-(pyrid-4-yl-vinyl)benzoic acid (PVBA). The strong head-to-tail hydrogen bonding was indicated by solid state ^{15}N -NMR studies. Thin films of PVBA can be easily grown on glass substrates by organic molecular beam deposition (OMBD) with an oblique incidence. As shown by second harmonic generation experiments, the films have a directional order that is parallel to the projection of the molecular beam direction on the substrate surface. Moreover, the

directional order is independent of film thickness at least up to 400 nm, and thermally stable up to 190°C. OMID of PVBA molecules on Ag(111) surface was studied by low temperature STM. The results reveal that PVBA molecules self-assemble into 1-dimensional wires of 1 nm width along <112> directions of the Ag-lattice with mesoscopic ordering at the micrometer scale. The individual 'molecular wires' consist of twinned PVBA rows stabilized by H-bonding. Distance between the parallel wires is at least up to 10 nm. Therefore, we have shown a new way to fabricate micrometer-long molecular wires.

SESSION H6:
Chair: Supriyo Datta
Tuesday Morning, November 30, 1999
Cape Cod/Hyannis (M)

10:30 AM **H6.1**
SCANNING POTENTIOMETRY STUDIES OF CHARGE TRANSPORT IN ORGANIC SEMICONDUCTOR-BASED FETS USING CONDUCTING PROBE ATOMIC FORCE MICROSCOPY (CP-AMF). Kannan Seshadri, C. Daniel Frisbie, Department of Chemical Engineering and Materials Science, University of Minnesota, Minneapolis, MN.

Investigation of charge transport mechanisms in organic semiconductors is of immense importance to development of devices such as thin film transistors and organic-based LEDs. Of particular interest are α -sexithiophene (6T) and pentacene, with hole mobilities high enough for flexible, all plastic devices. Conducting Probe Atomic Force Microscopy (CP-AMF) has been used to measure electrical transport characteristics of 6T. The semiconductor was deposited as crystals, ranging from 1 to 6 molecules (2-14 nm) in thickness and from 1-2 μ m in diameter by vacuum sublimation onto $\text{SiO}_2/\text{p-Si}$ substrates, with lithographically defined Au contacts. The semiconductor crystallite grows across the gap between two electrodes, with a capacitively coupled gate electrode, so as to achieve a field-effect transistor configuration (FET). An Au-coated conducting AFM probe is brought into contact with the electrically biased 6T crystallite, and the potential is measured as a function of position. This is a scanning potentiometry experiment, involving mapping the local potential over the surface of the organic semiconductor. Pentacene based FETs were also studied by fabricating contacts atop pentacene films on Si substrates, representing a top-down approach in FET configuration. Mesoscopic transport measurements, in combination with AFM imaging, are a useful strategy for elucidating charge transport across grain boundaries, charge trapping, and other structure-transport relationships in organic materials.

10:45 AM **H6.2**
CONTACT RESISTANCE MEASUREMENTS ON INDIVIDUAL GRAINS OF α SEXITHIOPHENE. Anna Chwang, C. Daniel Frisbie, University of Minnesota, Dept of Chemical Engineering and Materials Science, Minneapolis, MN.

We describe four point probe measurements on individual grains of the molecular semiconductor sexithiophene (6T). These measurements utilize thin 6T grains (2-14 nm in thickness and 1-2 μ m in length and width) deposited by vacuum sublimation onto SiO_2/Si substrates previously patterned with sets of four closely spaced (<400 nm) Au electrodes. The 6T grains grow between the four contacts and their electrical behavior is probed as a function of temperature and gate voltage applied to the substrate. From these data, we extract the Au-6T contact resistance and determine its sensitivity to both gate field and temperature.

11:00 AM **H6.3**
METAL-ORGANIC INTERFACE INTERACTIONS. L.C. Feldman^{1,2}, M. Huang³, M. Morales¹, K. McDonald¹, S. J. Rosenthal², R. A. Weller^{3,1}. ¹Dept of Physics and Astronomy, Vanderbilt University, Nashville TN; ²Dept of Chemistry, Vanderbilt University; ³Dept of Electrical Engineering, Vanderbilt University; ⁴Solid State Division, Oak Ridge National Lab., Oak Ridge, TN.

Interfaces formed by the combination of organic materials and metal contacts will undoubtedly prove to be a problematic aspect of employing molecular electronics. Much of the information on this important interface originates in the field of organic light emitting diodes (OLEDs), where the interplay between the structural aspects of the interface and the electronic aspects of the organic materials are revealed. This talk will focus on the metal/organic interactions encountered in systems designed for organic light emitting operation. Such systems may be models for the molecular electronic systems envisioned for the future. Structural studies, employing a high-resolution ion scattering apparatus, will be described for the aluminum/Alq system. Evidence for metal-organic penetration, at very moderate temperatures, is correlated with the deteriorating

electronic/optical properties of the system. Our experiments, along with earlier reports, show that penetration can be curtailed through the use of an intermediate oxide, although the final device configuration must then be optimized with respect to the balance of carrier tunneling through the oxide and interface protection. Other examples of metal/organic interfaces will be reviewed and the impact of these materials studies with respect to molecular electronics will be discussed.

11:30 AM ***H6.4**
ELECTRONIC STRUCTURE OF ORGANIC/METAL INTERFACES STUDIED BY UPS AND KELVIN PROBE. Kazuhiko Seki, Nagoya Univ, Res. Center for Materials Science and Dept of Chemistry, Nagoya, JAPAN; Hiroshi Oji, Eisuke Ito, Eisuke Yoshimura, Naoki Hayashi, Yukio Ouchi, and Hisao Ishii, Nagoya Univ, Dept of Chemistry, Nagoya, JAPAN.

The interfaces of organic materials with other solids play important roles in the function of various organic devices such as organic light-emitting diodes (OLEDs), spectral sensitization in photography, organic solar cells, and electrophotography. Also they should be important in future molecular devices, both in the central part of the device and at the connection with outside circuits. However, serious experimental examination of such interfaces has started only recently [1,2]. In this talk we focus our attention on the organic/metal interfaces, and summarize our understanding about (1) the energy level alignment right at the interface, and (2) possible band bending within an organic layer, mainly using the techniques of UV photoemission spectroscopy (UPS) and Kelvin probe method [3]. As for (1), the formation of electric dipole layer was observed in most organic/metal interfaces, and its origin is discussed. As for (2), recent examination of the existence/absence of band bending in ultrahigh vacuum will be reported. It is also pointed out that there can be much effects of (i) atmosphere at sample preparation and measurements, and (2) chemistry and interdiffusion at the interface.
[1] K. Seki, H. Yanagi, Y. Kobayashi, T. Ohta, Phys. Rev. B49, 2760 (1994) [2] S. Narooka, H. Ishii, D. Yoshimura, M. Sei, Y. Ouchi, K. Seki, S. Hasegawa, T. Miyazaki, Y. Harima, K. Yamashita, Appl. Phys. Lett., 67, 1899 (1995). [3] For a recent review, H. Ishii, K. Sugiyama, E. Ito, K. Seki, Adv. Materials, 11, 605 (1999).

SESSION H7:
Chair: James Murday
Tuesday Afternoon, November 30, 1999
Cape Cod/Hyannis (M)

1:30 PM ***H7.1**
CARBON NANOTUBE INTRAMOLECULAR DEVICES. Zhen Yao, Henk Postma and Cees Dekker, Dept of Applied Physics and DIMES, Delft Univ of Technology, THE NETHERLANDS.

Single-wall carbon nanotubes promise to be ideal candidates for the ultimate miniaturization of electronic devices. Single-electron transistors employing metallic nanotubes and field-effect transistors employing semiconducting nanotubes have been demonstrated. We will focus on the more fascinating intramolecular devices. In particular, by introducing a single pentagon-heptagon topological defect pair into the hexagonal carbon bond network, two pieces of nanotubes with different atomic and electronic structures can be seamlessly fused together, thereby creating metal-metal, metal-semiconductor, or semiconductor-semiconductor junctions. We will show the electrical measurements of well-defined nanotube intramolecular junctions. A metal-semiconductor junction is found to act like a rectifying diode, that is, it exhibits nonlinear transport characteristics that are strongly asymmetric with respect to bias polarity. The conductance across a metal-metal junction appears to be strongly suppressed, which is consistent with tunnelling between the ends of two Luttinger liquids. We will also discuss transport measurements on intramolecular devices created by mechanical deformation.

2:00 PM ***H7.2**
CARBON NANOTUBES: ELECTRICAL TRANSPORT PROPERTIES AND DEVICES. Phaedon Avouris, Richard Martel and Herbert R. Shea, IBM Research, T.J. Watson Research Center, Yorktown Heights, NY.

Single-walled nanotubes (SWNTs) are nearly ideal one-dimensional systems with unique electrical, mechanical, and thermal properties, which make them promising candidates for nanoelectronic device applications. We will discuss several aspects of nanotube behavior, transport properties, and device applications. We will show that strong nanotube-substrate interactions allow the manipulation, with scanning probe microscope (SPM) tips, of both position and shape of NTs at room temperature. Manipulation by SPM tips facilitates the

measurement of the nanotube electrical properties and allows the fabrication of simple devices. An example of a field effect transistor (NT-FET) involving a single 1.5 nm diameter semiconducting nanotube as its channel will be discussed. This NT-FET behaves as a p-channel MOSFET, and the Si back-gate can modulate the current by 5 orders of magnitude. The high electrode-NT contact resistance acts as a tunnel barrier at low temperatures transforming the NT FET to a single electron transistor (SET). We will then discuss how one can produce SWNT rings from straight SWNTs, and how these rings can be used to elucidate the transport mechanisms in SWNTs taking advantage of electron interference effects. We will show that low temperature magneto-resistance measurements on the rings allow the measurement of the coherence length in SWNTs. From the temperature dependence of the coherence length we determine that the dominant dephasing mechanism, at low temperatures, involves Nyquist electron-electron interactions, and that the SWNT ring is a state of weak localization in the temperature range of 3-60 K. At the same time strong electron correlation produces a Fermi level singularity. Below about 1 K we observe a transition from the weakly localized to a strongly localized state where transport is thermally activated and, finally, below about 0.7 K a weak anti-localization behavior is seen.

2:30 PM **H7.3**

DEFECTS AND TRANSPORT IN CARBON NANOTUBES.
Steven G. Louie, Department of Physics, University of California at Berkeley, and Materials Sciences Division, Lawrence Berkeley National Laboratory, Berkeley, CA.

The nanometer dimensions of the carbon nanotubes together with the peculiar electronic structure of a graphene sheet make these quasi-one-dimensional structures have highly unusual electronic properties. In this talk, I will briefly review some theoretical work on the relation between the atomic structure and the electronic and transport properties of the carbon nanotubes. In particular, results on the quantum conductance of carbon nanotube junctions and tubes with defects will be presented. Calculations have been carried out using both *ab initio* and tight-binding methods. Metal-semiconductor, semiconductor-semiconductor, and metal-metal junctions have been studied. Other defects such as vacancies, substitutional impurities, and pentagon-heptagon defect pairs on tube walls are shown to produce interesting effects on the conductance. The effects of long-range vs. short-range disorders on the transport properties of metallic and electrostatically doped semiconducting carbon nanotubes are also examined, with the metallic tubes being much less affected by long-range disorders. This rich interplay between the atomic/structural properties and the electronic properties of the carbon nanotubes gives rise to new phenomena and the possibility of nanoscale device applications.

SESSION H8:

Chair: Mark A. Ratner
Tuesday Afternoon, November 30, 1999
Cape Cod/Hyannis (M)

3:30 PM **H8.1**

PHYSICS OF THE METAL-CARBON NANOTUBE INTERFACES: CHARGE TRANSFERS, FERMI-LEVEL "PINNING" AND APPLICATION TO THE SCANNING TUNNELING SPECTROSCOPY. Yongqiang Xue, Supriyo Datta, Purdue University, School of Electrical and Computer Engineering, West Lafayette, IN.

Recent experiments on the single-wall carbon nanotube (SWNT) field-effect transistors and the scanning tunneling spectroscopy (STS) of supported SWNT show distinct behavior regarding the interface Fermi-level positions. This raises the important question of whether the Fermi-level positioning depends on the contact geometry and/or the interface coupling. In this work we present a theory of the scanning tunneling spectroscopy of a single-wall carbon nanotube supported on the Au(111) substrate. The main results of our work are: (1) the work function difference between the gold substrate and the nanotube leads to charge transfers across the interface, which induce a local electrostatic potential perturbation on the nanotube side. This atomic-scale interfacial potential perturbation shifts the energy levels of the nanotube relative to the gold Fermi-level, and gives rise to the observed Fermi-level shift in the STS current-voltage characteristics. (2) for transport in the direction parallel to the nanotube axis, as in the case of nanotube transistors, the local potential perturbation at the interface is not important in determining the Fermi-level position if the coupling between the metal and the nanotube is strong (i.e., low resistance contact). Any discrepancy between the metal Fermi-level and the nanotube "charge-neutrality level" should be screened out rapidly by the metal-induced gap state (MIGS) in the nanotube side,

leading to the "pinning" of the Fermi-level around the mid-gap position at low temperature. (3) we have taken the localized 5d orbitals of the platinum tip into account in our treatment of the STS which are responsible for the atomic resolution imaging of the nanotube.

3:45 PM **H8.2**

SWNT BASED CIRCUIT: THE DOUBLE QUANTUM DOT.
J. Lefebvre, M. Radosavljevic, A.T. Johnson, Dept of Physics and Astronomy and LRSMS, University of Pennsylvania, Philadelphia, PA.

We present data obtained on multiple SWNTs (single-wall carbon nanotubes) circuits. In particular, SWNTs put on top of one another behave as two quantum dots in series. Calculations show that the junction is responsible for the tunnel barrier between the two dots. The tunneling amplitude of the barrier can be tuned electrostatically.

4:00 PM **H8.3**

QUANTUM TRANSPORT AND DATA STORAGE IN NANOTUBE DEVICES. David Tománek, Department of Physics and Astronomy, Michigan State University, East Lansing, MI.

Carbon nanotubes and related fullerene structures are investigated for their usefulness as memory and logic elements, as well as manipulation tools, in molecular electronics. Multi-wall carbon nano-capsules containing charged fullerene ions, such as $K@C_{70}^+$, behave as tunable two-level systems. Transitions between the two states can be induced by applying an electric field between the end caps of the outer capsule. Since the position of the encapsulated fullerene can be associated with a bit value, these systems can be used as nonvolatile memory elements [1]. Due to their small size and absence of incoherent scattering, nanotubes themselves behave as quantum conductors. Whereas the conductance of ballistic conductors is an integer multiple of the conductance quantum in most systems, the weak inter-wall interactions in multi-wall nanotubes may block some of the quantum conductance channels and redistribute the current non-uniformly over the individual tubes. These results provide a natural explanation for the unexpected non-integer conductance values observed for multi-wall nanotubes [2].

Nanotubes may also be used for a precise, semi-continuous deposition of atoms on nanostuctures. Such atoms, when intercalated in nanotubes, are dragged by an electric current, which may be induced and controlled by the relative phase shift between two laser beams, irradiating the tubes at frequencies ω and 2ω [3]. Supported by the Office of Naval Research under Grant Number N00014-99-1-0252.

Young-Kyun Kwon, David Tománek, and Sumio Iijima, "Bucky-Shuttle" Memory Device: Synthetic Approach and Molecular Dynamics Simulations, *Phys. Rev. Lett.* **82**, 1470 (1999).

Stefano Sanvito, Young-Kyun Kwon, David Tománek, and Colin J. Lambert, Fractional quantum conductance in carbon nanotubes (submitted for publication).

Petr Král and David Tománek, Laser driven atomic pump, *Phys. Rev. Lett.* **82**, 5373 (1999).

4:30 PM **H8.4**

NOVEL BEHAVIOR IN NANOTUBE-JUNCTION DEVICES
F. Leonard and J. Tersoff, IBM T.J. Watson Research Center, Yorktown Heights, NY.

Carbon nanotubes (NTs) hold great promise for nanoscale electronic devices. Though only a nanometer across, they have exceptional strength and stability, and they can be either metallic or semiconducting. An exciting possibility lies in devices fabricated on a single tube, which in principle permit extremely small size and high density. In this talk, we present results on the properties of p-n junctions, n-i junctions, and Schottky barriers made on a single-wall carbon NT. We find that NT devices differ dramatically from classic planar bulk devices. In contrast to bulk junctions, the depletion width for NTs varies exponentially with inverse doping. In addition, there is a very long-range (logarithmic) tail in the charge distribution, extending over the entire tube. Another major difference is that, for typical metallic contacts to NTs, Fermi-level pinning is weak or nonexistent. Even when there is strong pinning, the barrier seen in transport will be radically different from that expected based on the traditional picture of pinning. Our general conclusions should apply to a broad class of NT heterojunctions, and to other quasi-one-dimensional "molecular wire" devices.

SESSION H9:
Chair: Ari Aviram
Wednesday Morning, December 1, 1999
Cape Cod/Hyannis (M)

8:30 AM **H9.1**

THEORY OF ELECTRONIC TRANSPORT IN MOLECULAR

JUNCTIONS. S.N. Yaliraki and Mark A. Ratner, Dept. of Chemistry and Materials Research Center, Northwestern University, Evanston, IL.

Chemical synthesis, whether based on molecular self-assembly techniques or end atom modifications, combined with advances in measurement probes such as scanning probe microscopy or break junction techniques have made the measurement of current through single molecules or molecular strands possible. We study theoretically the electronic transport in such molecular wire circuits. We present a time-independent scattering formalism, based on the Landauer formula of mesoscopic physics, that includes a descriptor of the molecule and the metallic contact electrodes. The molecular as well as the molecule/metal coupling description is obtained from ab-initio methods. The conductance of junctions of experimentally relevant systems is obtained. Effects of chemical bonding, geometry, dimensionality and neighboring molecules in adlayers on the conductance are discussed. Our results show that the description of the isolated molecular system is not sufficient to capture the behavior of the whole junction. Finally, we comment on another determining factor for the conductance of these systems, namely the location of the Fermi energy of the metallic contact relative to the molecular energy levels. To test the prevailing assumption that the Fermi energy occurs at mid-gap, we study the electronic structure of the molecule of interest attached to gold clusters and find that the Fermi level lies closer to the molecular HOMO than the LUMO. This renders our theory free of adjustable parameters and shows that the consistent approach fixes E_F at the bulk metal work function, but requires shifting the molecular levels to account for the molecule-metal interaction. Differences and similarities with dots, tubes and Luttinger liquids will be emphasized.

9:00 AM *H9.2
MOLECULAR SCALE ELECTRONICS. James M. Tour, Department of Chemistry and Center for Nanoscale Science and Technology, Rice University, Houston, TX.

Synthetic organic routes to precisely defined conjugated macromolecules (molecular scale wires) will be described using solution and solid phase approaches. The molecular scale wires are based on poly(phenylene ethynylene)s and poly(thiophene ethynylene)s and they possess thiol, selenol, and tellurol end groups to function as molecular scale alligator clips. Several molecular based resonance tunneling diodes (RTD) have been demonstrated. Potential routes to molecular based CPUs will be outlined wherein electrostatic potentials are used as the information-carrying packets. A route to overcoming the detailed need for nanolithography will be described using self-assembling molecular systems possessing logic and memory within a molecular-based CPU.

9:30 AM *H9.3
SELF-ASSEMBLY OF NANOSCALE COMPONENTS FOR MOLECULAR ELECTRONICS. Theresa S. Mayer, Thomas N. Jackson, Michael J. Natan, Thomas E. Mallouk, Department of Electrical Engineering, Pennsylvania State University, University Park, PA

Nanoscale and molecular electronics promise to deliver ultra high-density memory and logic circuits that can be realized with dimensions well below the scaling limits of conventional microfabrication techniques. To realize this promise, considerable attention has been devoted to developing molecular-level devices that function as nonlinear circuit elements and nanowires that interconnect these circuit elements. In this talk, we will provide a review of recent research activities related to the fabrication and characterization of nanoscale components including segmented metal rods and diodes, and the development of techniques that can be used to assemble these components into two- and three-dimensional networks. In particular, we are using membrane replication methods to make high aspect ratio, segmented metal rods consisting of alternating layers of Au, Pt, Ag, and Pt that are well suited for orthogonal self-assembly strategies. We have observed using fluorescence microscopy of Au-Pt-Au tipped rods that the Au regions of the rods can be derivatized selectively relative to the Pt with chain-terminating groups such as amines, carboxylates, or single-strand DNA. Using a combination of field- and chemical-assisted assembly techniques, we have aligned and attached 100 nm diameter segmented rods with good uniformity and reproducibility onto templated SiO_2 substrates. This has allowed us to characterize electrically simple segmented metal rods as well as more complex rods containing active components at the interface between the metal layers.

SESSION H10:
Chair: Mildred S. Dresselhaus
Wednesday Morning, December 1, 1999
Cape Cod/Hyannis (M)

10:30 AM H10.1
SYNTHESIS AND CHARACTERIZATION OF CONJUGATED MOLECULAR WIRES THREADED BY INSULATING TUBULES. Intae Kim, Yadong Yin, Younan Xia, University of Washington, Department of Chemistry, Seattle, WA.

We have demonstrated a self-assembly approach for the synthesis of conjugated organic polymers threaded by molecular tubules, with poly(p-phenylenevinylene) (PPV) and cyclodextrin rings as the example. In water, beta-cyclodextrin and stilbenoid compounds terminated in sulphonium end groups were self-assembled (as driven by hydrophobic interactions) into stable inclusion complexes; these complexes were subsequently polymerized into precursor polymers to PPV by addition of NaOH. Finally, the as-synthesized precursor polymers were converted into conjugated polymer PPV by thermal elimination of sulphonium groups. The potential use of this new type of molecular wires will also be discussed.

10:45 AM H10.2
END-GRAFTED SEMICONDUCTING POLYMER—CANDIDATE FOR MOLECULAR WIRE. Kazuaki Furukawa, Keisuke Ebata, Michiya Fujiki, NTT Basic Research Laboratories, Kanagawa, JAPAN.

Molecular wire, a nanoscale lead, is attracting considerable attention not only for key technology to realize molecular devices in the next century but also for basic research to reveal intrinsic optoelectronic properties at the single molecular level. For the macromolecules directed to molecular wire use, prerequisites are (1) conductivity, (2) connectivity, and (3) rigidity. Here we report on polysilanes, a synthetically accessible silicon-catenated polymer with such semiconducting properties as photoconductivity, high hole drift mobility, and electroluminescence, as a candidate for a molecular wire. We demonstrate an end-grafted rodlike polysilane, covalently bonded onto a Si(111) surface at one end and stretched more than 500 nm in length on the surface. We developed a unique "end-graft" technique to fix individual polysilane molecules homogeneously and extensively with a controllable density on a substrate surface. This was achieved by chemical reaction between a reactive anchor of alkylbromide built on the surface and an end-lithiated polysilane. The substrate was prepared by photochemical reaction of $\text{Br}(\text{CH}_2)_2\text{CH}=\text{CH}_2$ with Si-H on an atomically flat SiH(111) surface. The latter was prepared by either living radical polymerization of masked dienes or scission reaction of the polysilane by a lithium reagent. Polysilane are also unique in that the backbone rigidity is extensively varied depending on the steric effects of the organic substituents. The persistence length of rigid polysilanes reaches ca. 90 nm in solution at room temperature (longer than DNA ~60 nm!). We applied the above "end-graft" technique to the rodlike polysilane poly[n-decy{[(s)-2-methylbutyl]}silane]. Atomic force microscopy visualizes the end-grafted rodlike polysilane as "macromolecular ropes" lying on the surface. Because the density of the end-grafted polysilane is controllable by using substrates with different reactive anchor densities, we can place single polysilane molecules in a desired area, for instance between electrodes. A project to measure the I-V characteristics of end-grafted polysilanes is now in progress.

11:00 AM H10.3
FABRICATION AND TRANSPORT PROPERTIES OF Te-DOPED Bi NANOWIRE ARRAYS. Y.M. Lin, Dept. of Electrical Engineering and Computer Science; X. Sun, S.B. Cronin, Dept. of Physics; M.S. Dresselhaus, Dept. of Electrical Engineering and Computer Science, Dept. of Physics; J.Y. Ying, Dept. of Chemical Engineering, Massachusetts Institute of Technology, Cambridge, MA.

Bi nanowire arrays with wire diameters ranging from 10 nm to 120 nm have been fabricated by pressure injection of liquid bismuth into porous anodic alumina template. Because of the small electron effective mass and the highly anisotropic Fermi surface of Bi, the nanowire system is predicted to be a promising material for the study of the quasi one-dimensional (1D) electronic system and possibly for thermoelectric applications. The contributions from electrons and holes can be decoupled by altering the Fermi level so that the nanowire system becomes either n-type or p-type. Using similar fabrication techniques, Te-doped Bi nanowires with different doping concentrations are prepared providing a n-type nanowire system. The XRD study of the doped nanowire arrays shows that the crystallinity of the bulk Bi is preserved and the wires exhibit a preferred (101) orientation. The semimetal-semiconductor transition of the nanowires due to quantum confinement for this wire orientation is calculated to occur at a diameter of 49 nm. In this paper, we report the dependences of the transport properties, such as electrical resistance, magnetoresistance on temperature, wire diameter and the doping concentration. Based on the band structure of the bulk Bi and the 2-band Lax model, the theoretical transport properties of the quasi 1D system for various carrier concentrations are calculated and compared with the experimental results. Preliminary experimental

results of the Seebeck coefficient will also be discussed. We gratefully acknowledge the support of MURI subcontract 0205-G-7A114-01, NSF grant CTS-9257223 and DMR-98-04734, and the US Navy contract N00167-92-K0052.

11:15 AM H10.4

TRANSPORT MEASUREMENTS OF INDIVIDUAL Bi NANOWIRES. S.B. Cronin^a, Y.M. Lin^a, X. Sun^a, Z. Zhang^a, J.Y. Ying^a, M.S. Dresselhaus^{a,b}; ^aDepartment of Physics, ^bDepartment of Electrical Engineering and Computer Science, and ^cDepartment of Chemical Engineering, Massachusetts Institute of Technology, Cambridge, MA.

The extremely small effective mass of Bi makes Bi nanowires an interesting system for studying quantum behavior. Determination of the electronic transport properties of Bi nanowires using a 4 point measurement method is essential in understanding the electronic structure of these nanowires. The absolute resistivity attained by this 4 point method is also important in evaluating the potential value of Bi nanowires for thermoelectric applications. The Bi nanowires used in this work are single crystal with nearly the same crystal structure and lattice constant as bulk Bi. The Bi nanowires are prepared by nonlithographic means (self-assembly), by first filling a porous alumina template with molten Bi or with Bi vapor and then dissolving the template leaving a solution of free standing wires. Individual wires from the solution are then used for the I-V measurement. For practical applications it may be desirable to leave the wires in the template, however in order to perform a 4 point measurement it is necessary to remove the wires from the template. The technique and methodology for affixing four electrodes on a single free standing Bi nanowire are discussed in detail. Attention will be given to various difficulties in the experiment such as oxidation of the Bi nanowires, unfavorable mechanical properties of Bi, such as low melting point, and static discharge. The nanowires studied in this work range from 70 to 200 nm in diameter. We plan to extend the measurements to wires of much smaller diameters. Theoretical predictions of quantum effects on the electronic structure and transport properties of Bi nanowires will be given. We gratefully acknowledge the support of MURI subcontract 0205-G-7A114-01, NSF grants CTS-9257223 and DMR-9400334, and the US Navy contract N00167-92-K0052.

11:30 AM H10.5

PLASMONICS: ELECTROMAGNETIC ENERGY TRANSFER AND SWITCHING IN NANOPARTICLE CHAIN ARRAYS BELOW THE DIFFRACTION LIMIT. M.L. Brongersma, J.W. Hartman, and H.A. Atwater, Thomas J. Watson Laboratory of Applied Physics, California Institute of Technology, Pasadena, CA.

Integrated optics faces a fundamental problem in guiding, switching, and amplification of light in that structures must have dimensions comparable to the wavelength of the guided light. Recently, it was theoretically shown that this problem might be circumvented by transporting electromagnetic energy along linear chains of metal nanoparticles below the optical diffraction limit. Our models show that this transport is coherent and relies on the near-field electrodynamic interaction between closely spaced nanoparticles that sets up coupled plasmon modes in the chain. We have modeled power flow through such "plasmon wires" and three-terminal "plasmon switches" consisting of linear chains and tee-junctions or crosses. These structures could form the prototypical circuit building blocks of a nanoparticle architecture. The energy dispersion relations for linear chains have been computed; two branches are found corresponding to the transverse and longitudinal modes of the chain. The propagation wavelength, bandwidths and group velocities can be estimated as functions of metal particle size, interparticle distance, polarization, and the dielectric properties of the host matrix. Model calculations were performed for 25 nm Ag nanoparticles in dielectric host materials such that the plasmon energy is $\hbar\omega_p < E_g$, the host material bandgap. It was shown that the group velocity in linear chains was $v_g \approx 0.01$ for 50 nm center-to-center particle spacing and the 1/4 propagation length was 500 nm implying the possibility of energy transport over several microns. Plasmon switches are structures in which the power flow through a plasmon wire can be modulated at a tee-junction by changes in the field amplitudes or the input polarization in the "control wire". We will discuss the advantages and limitations of these structures for use as future nano-optical switches and interconnects.

11:45 AM H10.6

FABRICATION AND CHARACTERIZATION OF EXTREMELY NARROW METALLIC WIRES. D. Nataleau, R.L. Willett, L.N. Pfeiffer, K.W. West, Bell Laboratories, Lucent Technologies, Murray Hill, NJ.

We have developed a general method for producing electrically continuous metal wires greater than one micron in length with widths below 5 nm, the size scale of multiwalled carbon nanotubes. These

wires can be made singly or in arrays, from a variety of materials, and should allow us to study normal metals, magnetic materials, magnetic multilayers, and superconductors in a previously inaccessible size regime. We present preliminary conductance measurements on normal metal wires of several diameters less than 20 nm, from 300 K to below 100 mK in fields up to 8 Tesla.

SESSION H11/G6: JOINT SESSION:
NANO TO MOLECULAR SCALE ELECTRONICS OF
ORGANIZED STRUCTURES

Chairs: Samson A. Jenekhe and Jane Shaw
Wednesday Afternoon, December 1, 1999
Salon E (M)

1:30 PM H11.1/G6.1

NANOSCALE PATTERNS OF METAL NANOPARTICLES
CHEMICALLY-ASSEMBLED ON BIOMOLECULAR SCAFFOLDS:
ASSEMBLY STRUCTURE, STABILITY AND ELECTRON
TRANSPORT PROPERTIES. James E. Hutchison, Leif O. Brown,
Jana Mooster, Scott M. Reed, Mary E. Schmidt, Dept of Chemistry
and Materials Science Inst, Univ of Oregon, Eugene, OR; Laura I.
Clarke, Martin N. Wybourne, Dept of Physics and Astronomy,
Dartmouth College, Hanover, NH.

The novel electronic properties (e.g., Coulomb blockade) of nanometer scale assemblies of metal nanoparticles make them potentially useful in nanoelectronic devices and extremely sensitive chemosensors. To date, no straightforward and reproducible methods are available for the fabrication of low-dimensional nanoparticle assemblies. The fabrication of nanoscale lines is a particularly challenging, yet important goal. Our method for nanofabrication of linear nanoparticle arrays involves the assembly of functionalized metal nanoparticles onto rigid biomolecular scaffolds cast upon an insulating substrate and bridged between narrowly spaced electrodes. Our previous investigations of unpatterned nanoparticle thin films provided clear evidence of Coulomb blockade at room temperature, but the response was unstable over time. In this paper we present a wet chemical approach to preparing one- and two-dimensional arrays of gold nanoparticles assembled onto a polypeptide (poly-L-lysine) scaffold layer. The assembly process provides a simple, chemical method to immobilize the particles and is found to stabilize the electrical response (Coulomb blockade) of the array compared with unpatterned samples. A striking feature of the electrical properties is that the electron transport properties are dominated by transport through one-dimensional chains within the sample. Structural studies by AFM and XPS will be presented that support the transport findings and provide evidence for the formation of one-dimensional assemblies within the arrays.

1:41 PM H11.2/G6.2

CHARGE TRANSPORT IN SEMICONDUCTOR QUANTUM DOT SOLIDS. C.A. Leatherdale, N.Y. Morgan, I. Prasad, M.G. Bawendi, and M.A. Kastner, Departments of Chemistry and Physics, Massachusetts Institute of Technology, Cambridge, MA.

Close-packed arrays of semiconductor quantum dots represent a model system in which to study the evolution of electronic structure in an artificial solid. We study photoconductivity in close-packed solids of nearly monodispersed CdSe semiconductor nanocrystals. We observe quantum dot size and surface passivation dependent photoconductivity that can be qualitatively understood by considering the energy required to overcome the Coulomb energy of the initial electron-hole pair. The temperature dependence of the photocurrent indicates that tunneling processes dominate both charge separation and charge transport. We model the initial charge separation step using simple tunneling calculations. Simultaneous fluorescence quenching and photoconductivity measurements suggest that many more charge separated pairs are created than reach the electrodes. Measurements of the fluorescence intensity as a function of charge in the film, reveal that excess charge causes reversible photodarkening of the quantum dot solid accounting for some of the discrepancy. Hysteretic behaviour and long time transients, observed in both the photoconductivity and conductivity measurements, suggest that charge is easily trapped in the solid. Strong electron-electron interactions between charges on different sites in the lattice may be limiting the carrier mobility.

2:00 PM H11.3/G6.3

OPTICAL PROPERTIES OF SEMICONDUCTOR QUANTUM-DOT PHOTONIC CRYSTALS. Yu. A. Vlasov, M. Deutsch and D.J. Norris, NEC Research Institute, Princeton, NJ.

We explore the optical properties of semiconductor quantum-dot photonic crystals. These materials are made by combining colloidal chemistry with two steps of hierarchical self-assembly. First,

monodisperse sub-micron silica spheres slowly settle onto a flat substrate and self-organize as a face-centered cubic lattice that is periodic on an optical length scale. Second, this template serves as a three-dimensional scaffolding for the self-assembly of colloidal CdSe nanocrystals into densely packed arrays, referred to as quantum-dot solids. Subsequently, the silica template can be removed by selective etching and a three-dimensionally patterned material consisting solely of semiconductor quantum dots is obtained. The resulting material is particularly interesting as a photonic crystal since we control several key parameters that determine its final behavior. First, we control the unique optical properties of individual semiconductor quantum dots. They have discrete optical transitions, efficient luminescence, high gain and optical nonlinearities, which are tunable with the size of the nanocrystal. Second, we control the structure of the silica template. By adjusting the size, spacing, and arrangement of the silica spheres, we determine how the quantum-dot solid is patterned on an optical-length scale. This structure modifies the internal electromagnetic environment and influences the propagation of photons through the material. Here we study the optical properties of such semiconductor quantum-dot photonic crystals by transmission, reflection and diffraction. We present results that show the strong influence of the periodic structure of the photonic crystal on the photoluminescence of the semiconductor quantum-dot solid.

2:15 PM H11.4/G6.4

SYNTHESIS OF LUMINESCENT ULTRA-SMALL Si NANO PARTICLE COLLOIDS AND THIN FILMS. Munir H. Nayfeh, J. Therrien, O. Akcasir, G. Belomoin, Z. Yamani, N. Barry, E. Grattan, University of Illinois at Urbana-Champaign, Department of Physics, Urbana, IL.

We describe a procedure for conversion of solid porous silicon into a dispersed colloid of ultra-small (~1 nm) silicon nano particles. When the colloid is excited at 355 nm, blue emission is observable with the naked eye, in room light. The luminescence is dominated by an extremely strong deep blue band at 390 nm, with a structureless weak orange/red tail, and a weak infrared band at 760 nm. We recorded, using two-photon infrared femto second excitation, the auto-correlation of the blue luminescence of a few particles in the laser interaction volume (of one pico cubic centimeter) including single particles. The measurements yield a particle's diffusion, size, and excitation efficiency comparable to those of fluorescein dye molecules, one of the top efficient dyes in the blue. Thin films of particles are formed on device quality silicon substrates by gentle evaporation from a volatile (acetone) particle colloid, without compromising the blue emission. Two-terminal I-V spectra of the deposited film, taken using a scanning tunneling microscope, will be presented.

2:30 PM H11.5/G6.5

HIGHER-ORDER SYNTHESIS OF MOLECULAR MAGNETS. Sébastien Vaucher and Stephen Mann, School of Chemistry, University of Bristol, Bristol, UNITED KINGDOM.

A major goal in contemporary materials science is the synthesis of molecular based materials that exhibit spontaneous magnetisation. Previously, research approaches have been focused on the synthesis of new types of compounds, essentially by engineering at the unit cell level. A wide range of synthetic pathways to molecular magnets with appealing properties (high T_c, photoinduced magnetisation, etc.) are now available. Whereas it has been shown that inorganic materials, such as silica or titania, can be synthesised across a range of length scales by constructional, morphological and hierarchical coding of precipitation reactions, the analogous control of the higher-order structural features of molecular magnets has to our knowledge not been investigated. In this presentation, we illustrate how it is possible to use similar approaches to control the growth and organization of molecular magnets at the nano- and mesoscale. Several synthetic methods have been investigated and the products characterised by SEM and TEM. The general application of higher-order synthesis of functional molecular systems will be discussed.

2:45 PM H11.6/G6.6

ELECTROCHEMICAL METAL DEPOSITION CONTROLLED BY SELF-ASSEMBLED MONOLAYERS AND POLYMERS. Andrea D. Wells, John T. McDevitt, William B. Murray, University of Texas at Austin, Chemistry & Biochemistry Dept., Austin, TX.

To more effectively process materials, new procedures were developed to anchor molecular reagents atop samples using self-assembled monolayers (SAM's) and polymers. Just as end group functionality allows specific ligands to interact with charged metal centers, appropriate choice of terminal functional group allows certain organics to interact strongly with metallic ions in the electrolyte solution. Through this interaction, organic layers can exert control over the electrochemical deposition of metal layers on high-T_c superconductors. Nucleation and growth of metal deposits on the surface are monitored by various electrochemical techniques. Electron

microscopy, scanning probe and surface science methods are used to characterize the metal/superconductor assemblies.

3:30 PM H11.7/G6.7

NANOSCALE PROCESSING OF ELECTROACTIVE MATERIALS. Michael Rubner, Department of Materials Science and Engineering, MIT, Cambridge, MA.

Nanoscale processing techniques have been utilized to manipulate a variety of electroactive materials such as light emitting Ru(II) complexes, inorganic nanoparticles and conjugated polymers into thin film devices. Control at the nanoscale level has made it possible to dramatically improve the performance of these thin films. Details concerning the processing and electrical/optical properties of these new nano-composites will be discussed.

4:00 PM H11.8/G6.8

LAYER-BY-LAYER ASSEMBLY OF NANOPARTICLES. Arif Mamedov, John Ostrander, Oklahoma State University, Chemistry Department, Stillwater, OK; Farkhad Aliev, Departamento de Física de la Materia Condensada, Universidad Autónoma de Madrid, Madrid, SPAIN; Miguel Correa-Duarte, Luis Liz-Marzan, Departamento de Química Física, Universidad de Vigo, Vigo, SPAIN; Nicholas Kotov, Oklahoma State University, Chemistry Department, Stillwater, OK.

The layer-by-layer assembly (LBL), i. e. the cyclic deposition of monolayers of oppositely charged materials, has been applied to the preparation of hybrid polyelectrolyte/nanoparticle thin films. This technique affords combining mechanical properties of polymers and unique physical characteristics of size-quantized clusters. Other advantages of the LBL processing of nanoparticulate films include simplicity, universality, tolerance to the substrate's shape, accurate control over the size, size distribution and structure of nanoparticles being assembled. Selection of nanoparticles defines the properties and the area of application of the produced assemblies. LBL films of CdS, CdSe, magnetite, yttrium iron garnet (YIG), cobalt nanoparticles, and aluminosilicate sheets yielded coatings with interesting light-emitting, electrical, magnetic, magnetoresistive, and magnetooptical properties. Importantly, the LBL technique opens a possibility to design sophisticated stratified structures. In particularly, the layer sequence was demonstrated to affect the coercivity, ion-sieving effect, magnetooptical properties of magnetite/aluminosilicate/polyelectrolyte, CdSe/aluminosilicate/polyelectrolyte, and YIG/polyelectrolyte assemblies respectively. The LBL deposition was also applied to the preparation of films from naked and silica-coated nanoparticles of magnetite. The insulating SiO₂ coating affords isolation of individual magnetic grains and prevention of the exchange coupling between the nanoparticles. It was shown that the assembly of coated particles has a potential to reduce the noise of magnetic storage media and increase its storage capacity.

4:15 PM H11.9/G6.9

PHOTOVOLTAIC RESPONSES IN POLYMER-FULLERENE IONICALLY SELF-ASSEMBLED NANOSTRUCTURES. P.J. Neyman, W. Graupner, J.R. Heflin, Virginia Tech, Dept. of Physics, Blacksburg, VA; D. Marciu, M. Miller, A. Drake, Luna Innovations, Inc., Blacksburg, VA; H. Wang, H.W. Gibson, H.C. Dorn, Virginia Tech, Dept. of Chemistry, Blacksburg, VA; R.M. Davis, Virginia Tech, Dept. of Chemical Engineering, Blacksburg, VA.

The ultrafast photoinduced electron transfer from conjugated polymers to fullerenes has allowed the production of efficient organic photovoltaic devices. Since the exciton diffusion distance is on the order of 10 nm, however, the charge transfer cannot occur unless the fullerene acceptor is within this distance of any given optically-excited electron-hole pair. We have recently fabricated polymeric photovoltaic devices from ionically self-assembled monolayers (ISAMs) and variations thereof. The ISAM nanostructure fabrication method simply involves the alternate dipping of a charged substrate into aqueous cationic and anionic solutions at room temperature. Each monolayer is fully formed within a couple minutes of immersion, and the bilayer thickness can be controlled from 0.3 to greater than 5.0 nm by variation of the solution parameters. Large-area, conformal, flexible, optoelectronic thin films can thus be fabricated with detailed structural and thickness control at the sub-nanometer level combined with ease of fabrication and low cost. We have employed several approaches to combine the tetraphenylphosphonium precursor of poly(p-phenylene vinylene) (PPV) with fullerenes. As two examples, hydroxylated C₆₀ forms direct ionic bonds with the cationic PPV precursor while pristine C₆₀ forms covalent bonds with the amine groups of a second polycation incorporated into the ISAM films. Comparison of the short-circuit currents, open-circuit voltages, and energy conversion efficiencies are presented for photovoltaic devices made from these and other novel polymer-fullerene self-assembled nanostructures.

4:30 PM H11.10/G6.10

CHARGE TRANSPORT AND ELECTROLUMINESCENCE IN NOVEL HETEROCYCLIC LIQUID CRYSTALS. Rong Fan, George G. Malliaras, Cornell University, Dept. of Materials Science and Engineering, Ithaca, NY; L. Sukhomlinova, S. Gu, R.J. Twieg, Kent State University, Chemistry Dept., Kent, OH.

We have investigated charge transport in a family of novel liquid crystals containing five member ring heterocycles (oxadiazoles, thiadiazoles, etc.). Efficient electron transport was observed in the smectic phase. The electric field and temperature dependence of the electron mobility was studied. Apart from being able to simultaneously function as liquid crystals and charge transport agents, these materials are highly fluorescent, allowing the fabrication of organic light emitting diodes. Their electroluminescent properties in devices with various electrode materials were studied.

4:45 PM H11.11/G6.11

SOL-GEL SYNTHESIS AND NONLINEAR OPTICAL PROPERTY OF SILICA THIN FILMS DOPED WITH CYANINE DYE J AGGREGATES. Takashi Watanabe, Keisuke Asai, Kenichiro Ishigure, The University of Tokyo, Dept. of Quantum Engineering and Systems Science, Tokyo, JAPAN; Hao-Shen Zhou, Itaru Honma, Electrotechnical Laboratory, Tsukuba, JAPAN; Akhira Mito, National Research Laboratory of Metrology, Tsukuba, JAPAN; Makoto Furuki, Osamu Wada, FESTA Laboratory, Tsukuba, JAPAN; Satoshi Tatsura, Corporate Research Laboratories, Fuji Xerox Co. Ltd., JAPAN.

It is widely known that J aggregates formed by cyanine dyes show strong nonlinear optical properties. In order to apply them to practical devices such as an optical switching device, many J aggregate material morphologies have been suggested. However, since the J aggregates are unstable in many matrices, it has been difficult to realize such applications. We tried to embed cyanine dyes such as 1,4-diethyl-2,2'-cyanine bromide into thin silica films by simple sol-gel processing and succeeded in making the dye molecules to form stable J aggregates in the films. The films were prepared in the following way; tetraethylorthosilicate was mixed with ethanol and stirred. The solution was added with dilute HCl solution and stirred. And then, the dye was added to it and the sol-solution was stirred. Finally, the sol-solution was used for film deposition on glass substrates by spin casting. In spite of containing plenty of the J aggregates, these films are transparent, homogeneous in thickness and stable at room temperature. The J aggregation depends on both of the dye concentration in the sol-solutions and the spinning speed during spin casting. The third order susceptibility $|\chi^{(3)}|$ of the films was measured by Z-scan method with sub-ps pulse laser. The films were irradiated with the beam at 77 K in vacuum environment ($<10^{-5}$ Torr). The $|\chi^{(3)}|$ of the film doped with dye till saturated concentration is 5×10^{-7} esu at on-resonant wavelength of 577 nm, which is larger than that of other organic materials. In addition, according to measurement of the response time τ of the optical nonlinearity by pump-probe method with fs pulse laser at 577nm, it was found that the τ is sub-ps. Thus, stability of the J aggregates, large $\chi^{(3)}$ and fast τ can be expected on the silica film doped with the J aggregates, simultaneously.

SESSION H12:

Chair: Shashi P. Karnaa
Thursday Morning, December 2, 1999
Cape Cod/Hyannis (M)

8:30 AM H12.1

CONTROLLING THE LOCAL ENVIRONMENT AND CHEMICAL STATES OF ELECTRONICALLY ACTIVE MOLECULES IN SELF-ASSEMBLED MONOLAYER STRUCTURES. D. Allara, T. Dunbar, A. Hooper, P. Weiss, M. Cygan, L. Bumm, A. Brose, Dept. of Chemistry, Pennsylvania State University, University Park, PA.

There is accelerating interest in harnessing the electronic properties of individual molecules for new generations of devices. Among the critical issues in making such devices are how to control the positioning of electronically active molecules and how to control their chemical and electronic states. This talk will discuss recent work directed towards the placement of electronically active molecules into defects in pre-assembled monolayers and on the characterization of the geometry and the local environment of the molecules. In addition, recent results will be discussed on the effects of metal atom deposition with respect to making contacts and to alteration of the electronic states (doping) of molecules.

9:00 AM H12.2

UNIMOLECULAR RECTIFICATION DOWN TO 105 K, AND SPECTROSCOPY OF HEXADECYLQUINOLINUM

TRICYANOQUINODIMETHANIDE. Robert M. Metzger, Laboratory for Molecular Electronics, Chemistry Department, The University of Alabama, Tuscaloosa, AL.

Hexadecylquinolium tricyanoquinodimethanide, 1, was first synthesized by Ashwell and co-workers for non-linear optical applications, and was studied by Sambles and co-workers for rectification in Langmuir-Blodgett multilayers between dissimilar metal electrodes. We have recently confirmed that 1 is a one-molecule rectifier of electrical current, between Al electrodes, as a Langmuir-Blodgett monolayer [Metzger et al., *J. Am. Chem. Soc.* 119:10455 (1997)]. The rectification persists down to 105 K [Chen & Metzger, *J. Phys. Chem. B* 103: 4407(1999)]. The dipole moment is large in the ground state (43 Debyes) but much smaller in the excited state (3 to 9 Debyes): this helps explain how the rectification works, in a slightly modified Aviram-Ratner fashion. The spectroscopy (Vis-UV, NMR, FTIR, XPS) is consistent with a zwitterionic ground state and a much less polar excited state. [Baldwin et al., *J. Phys. Chem. B* 103: 4269 (1999)]. Experiments at 4.2 K (to detect IETS) are in progress, and may be reported if successful.

9:15 AM H12.3

ELECTRONIC STRUCTURE AND RECTIFYING BEHAVIOR OF $M/C_{16}H_{33}-Q_3CNQ/M$ JUNCTIONS. C. Krasinski, C. Delerue, G. Allan, D. Vuillaume, IEMN Dept. ISEN, Lille, FRANCE; R.M. Metzger, Univ. of Alabama, AL.

A well-known paper of Aviram and Ratner [Chem. Phys. Lett. 29, 277 (1974)] proposed that a molecule which has a good electron donor and a good acceptor separated by a sigma-bonded bridge could act as a molecular rectifier. Inspired by this proposal, recent experimental papers [Metzger et al., JACS (1998); Vuillaume et al., Langmuir (1999)] have presented measurements of the electrical response of $C_{16}H_{33}-Q_3CNQ$ contacted by two metallic electrodes which for several samples is characterized by a clear rectifying behavior. In this work, we model this structure using first principles density calculations and semi-empirical tight binding calculations. We show that the electronic states closer to the gap of the molecule are fully delocalized in spite of the presence of a large permanent dipole: this effect results from the presence of the pi-bonded bridge between the donor and the acceptor. We calculate the electrical response of the system and we show that it is particularly important to perform a self-consistent calculation of the full structure, including the molecular layer and the electrodes. We obtain that the electrical rectification observed experimentally could come from an anisotropy of the electric field in the structure.

9:30 AM H12.4

I-V MEASUREMENTS ON MOLECULAR SHEETS AND STACKS. C. Daniel Frisbie, University of Minnesota, Dept of Chemical Engineering and Materials Science, Minneapolis, MN.

Our research group is performing several different types of current-voltage (I-V) measurements on sheets and stacks of organic molecules. The sheet and stack structures consist of extremely thin, vapor-deposited lamellar crystals of organic semiconductors or spontaneously adsorbed organic monolayers. In one approach, we use a conducting atomic force microscopy (AFM) probe as a positionable electrical contact to a molecular sheet contacted by a fixed electrode at the other end. This configuration allows I-V measurements as a function of the probe-electrode separation, yielding sheet resistivity of single monolayers and an estimation of the organic-metal contact resistance. The I-V characteristics in these two-terminal measurements are generally extremely non-linear and can be interpreted in terms of both a charge injection barrier and space charge limited transport. Conducting AFM tips may also be used to probe vertical charge transport through self-assembled monolayers on gold, and the I-V traces in these measurements show some differences from recently reported STM studies on the same systems. In a second approach, we employ electron beam lithography to fabricate fixed source and drain contacts to molecular sheets grown on SiO_2/Si substrates. We use the resulting metal/organic/metal structures in a transistor geometry to probe the field effect conductance of the sheet (the doped Si substrate serves as a gate electrode). These three-terminal measurements allow determination of the carrier mobility as a function of temperature (5-300 K) and the number of discrete molecular layers in the sheets. Importantly, we find metal-coated AFM tips may be used as potentiometric sensors to map voltage distributions in the molecular sheets used in these transistor experiments. The potential maps show the distribution of current and allow estimation of charge distributions in the sheets. An important theme in all of these experiments is the conjunction of AFM imaging with transport measurements, facilitating correlation of transport properties with specific, well-defined supramolecular structures.

9:45 AM H12.5

FABRICATION METHODS FOR GOLD NANoclUSTER DEVICES. A. Snow, M.G. Ancona, W. Kruppa, D. Park, J.B. Boos

and G.G. Jernigan, Naval Research Laboratory, Washington, DC.

The possibility of chemically self-assembling nanoelectronic devices and circuits has attracted wide attention because of its potential simplicity and favorable economics. In this work, a hybrid approach is explored in which pre-patterned nanoscale gold electrodes guide the self-assembly of ligand-stabilized gold nanoclusters. The gold nanoclusters are composed of a gold core (1-5 nm diameter) encapsulated by an alkanethiolate or phenylthiolate monolayer (4-16 nm thick). The deposition chemistry involves functionalizing the gold electrodes and/or the SiO_2 surface with chemical coupling agents. Clusters become immobilized on the surface when the surface-anchored coupling agents displace thiol in the ligand shell. XPS measurements were used to characterize the efficiency and selectivity of this deposition chemistry and to explore methods for enhancing its selectivity by surface passivation. By repeated immersions in cluster and dithiol solutions, multiple cluster layers were deposited forming a uniform resistive coating. The start-up of the deposition is delayed (3 cycles) indicating a spacing of about 10 nm between the "seed" clusters initiating the deposition. With hexanethiol-coated clusters the sheet resistance is found to be $2 \times 10^{11} \Omega/\text{square per nanocluster layer}$. Similar results obtained on macroscopic-sized samples suggest this number is truly characteristic of the film and is not due to contact effects. This value is also consistent with theoretical estimates. When the same experiment is performed with phenylthiol-coated clusters the resistivity is significantly lower and appears limited by the dithiol contacts to the Au electrodes. Discreteness in this conductivity suggests that the numbers of contacts is small and that effects of single molecule conduction are being manifested. Another area of experimentation has been to define narrow lines of clusters between the electrodes using dithiol bridging or lithography. With the former technique Coulomb blockade-like characteristics were observed at room temperature.

SESSION H13:

Chair: Robert M. Metzger
Thursday Morning, December 2, 1999
Cape Cod/Hyannis (M)

10:30 AM *H13.1

CONJUGATED ORGANIC "MOLECULAR WIRES" - CONDUCTION CHARACTERISTICS AND INCORPORATION INTO METAL AND METAL/SEMICONDUCTOR NANOSTRUCTURES. R. Reifenberger, Purdue University, W. Lafayette IN.

Key advances in the molecular electronics arena will require a better understanding of the electronic conduction mechanism in organic molecules and the coupling of suitable molecules into local circuit nodes. It will also be necessary to interface these "molecular circuit elements" with macroscopic structures. With these issues in mind, we will discuss recent experiments and theoretical models that provide some answers to these important questions.[1-8] The conduction properties of conjugated organic molecules will be reviewed and prototypical metal and metal/semiconductor nanostructures which exploit molecular conduction will be described.

[1] M. Dorogi, et al., *Phys. Rev. B* **52**, 9071 (1995) and R.P. Andres, et al., *Science* **272**, 1323 (1996).

[2] M. Samanta, et al., *Phys. Rev. B* **53**, 7626 (1996) and S. Datta, et al., *Phys. Rev. Lett.* **79**, 2530 (1997).

[3] W. Tian, et al., *Physica E* **1**, 304 (1997).

[4] W. Tian, et al., *J. Chem. Phys.* **109**, 2874 (1998).

[5] Y. Xue, et al., *Phys. Rev. B* **59**, R7852 (1999).

[6] T. Lee, et al., *Appl. Phys. Lett.* **74**, 2869 (1999).

This work was sponsored by the Army Research Office under Grant No. DAAL-03-92-C-0144 and NSF Grant No. 9708107-DMR.

11:00 AM H13.2

FORMATION OF Au_{13} NANOWIRES AND HOLES BY ATOMIC FORCE MICROSCOPY. R. Houbertz, Institute of Experimental Physics, Saarbruecken, GERMANY and Sandia National Labs, Livermore, CA; U.E. Volmar, R. Stein Kampf, Institute of Experimental Physics, Saarbruecken, GERMANY.

Atomic force microscopy (AFM) was used to generate Au_{13} cluster wires from thick Au_{13} cluster layers adsorbed on highly oriented pyrolytic graphite (HOPG) under ambient conditions. The wires were generated with and without applied bias. The extent of the resulting structures is dependent on the size of the applied bias. For zero or positive bias at the probe, the formation of cluster nanowires is observed, whereas for negative probe bias holes are generated. This observation is also confirmed by force-distance-curves. Particularly, the formation of holes cannot be understood by simply regarding van der Waals forces. It is shown, that the data can be understood in the framework of single-electron tunneling (SET) if a bias is applied.

Additionally, the interaction forces are calculated using a simple model. The calculated Coulomb forces between probe and sample are of the order of several hundred pN which is far above the acting van der Waals forces, thus being large enough to account for the generated structures.

11:15 AM H13.3

THE FORMATION, OPTICAL AND ELECTROPHYSICAL PROPERTIES OF THE POLYMER LANGMUIR-BLODGETT FILMS WITH LEAD AND MANGANESE SULPHIDES. Yu.N. Savin, S.I. Gordeev, A.V. Tolmachev Institute for Single Crystals, Kharkov, UKRAINE.

The optical and electrotransport properties of semiconductor nanoparticles in dielectric matrices draw attention now because quantum dimension effects can be observed here and such structures can be used in photonics, micro- and nanoelectronics. The organized molecular assemblies such as polymer Langmuir-Blodgett films evoke particular interest due to possibility to obtain the ordering molecular structures controlled in size. In this communication the investigation results of the formation processes of aromatic polyamic acid LB films, as well as the nucleation and growth PbS and MnS nanoparticles in these films are reported. LB films containing semiconductor nanoparticles were obtained by two stages. At first, Langmuir monolayers of polyamic acid were formed at the subphase containing $\text{Pb}(\text{NO}_3)_2$ or MnSO_4 salts and then were transferred on the quartz and silicon substrates. At the second stage LB films were exposed in water solution of Na_2S to obtain the nanoparticles of lead or manganese sulfides. Absorption of Pb^{2+} and Mn^{2+} ions on the Langmuir monolayers depending on pH of subphase are studied by XPS method. The nucleation and growth kinetics of nanoparticles depending on parameters determining the thermodynamics of polymer monolayers (pH, concentration of Pb , Mn and S ions, temperature, surface pressure) as well the duration of exposition in Na_2S solution are investigated. It is found the spectral component in UV-VIS absorption spectra is appeared after the exposition of LB films in Na_2S solution. This component is due to nanoparticles of PbS or MnS in quantum-restricted state (Q-state). The effects of a temperature and duration of exposition in Na_2S solution on the location of peak adsorption, long wave absorption edge and the nanoparticle sizes are studied. The photoconductivity and capacity-voltage characteristics are investigated versus the sizes and concentrations of a nanoparticles.

11:30 AM H13.4

ROOM TEMPERATURE SINGLE ELECTRON CHARGING OSCILLATIONS IN GOLD NANOPARTICLE NETWORKS FORMED UPON A BIOPOLYMER TEMPLATE. Laura I. Clarke, Martin N. Wybourne, Dept of Physics and Astronomy, Dartmouth College, Hanover, NH; Jana L. Mooster, Leif O. Brown, Scott M. Reed, and James E. Hutchison, Dept of Chemistry and Materials Science Institute, University of Oregon, Eugene, OR.

The past two decades have seen phenomenal growth in the study of artificially fabricated mesoscopic structures. Typically constraints imposed by the patterning technique have limited lateral feature size to around 20 nm. To prepare structures below this size, attention is being focused on intrinsic nanostructures, such as metal nanoparticles and single molecules. Metal nanoparticles that contain less than about one hundred atoms have a small enough inherent capacitance to make the charging energy at least an order of magnitude larger than the thermal energy at room temperature. While room temperature charging effects in single nanoparticles have been observed, a remaining challenge is to create arrays and architectures of metal nanoparticles that exhibit single electron charging behavior. Although the electrical properties of a few, recently reported arrays of nanoparticles have been studied, there are no reports of extended nanoparticle chains that show single electron charging effects at room temperature. We have prepared networks of one-dimensional metal nanoparticle arrays made by casting a film of the biopolymer poly-L-lysine onto metal electrodes with subsequent exposure to 11-mercaptoundecanoic acid stabilized gold nanoparticles. The current voltage (I-V) characteristics of gold nanoparticle - biopolymer networks show extremely stable, Coulomb blockade dominated transport effects at room temperature. Above a threshold voltage, the I-V behavior is almost linear. In some samples, periodic structure in the conductance is observed. We argue that these features arise from transport through one-dimensional regions of the network and show that the periodicity is consistent with the estimated capacitance of the nanoparticles. We will discuss the disorder in these systems and the probable number of nanoparticles involved in the transport.

11:45 AM H13.5

QUANTUM-DOT LEAD IODIDE FILMS FOR OPTICAL AND X-RAY IMAGING APPLICATIONS. Krishna C. Mandal, Bryce K. Dille, David Rauh, EIC Laboratories, Inc., Norwood, MA; O. Savadogo, Materials Engineering Department, Ecole Polytechnique, Montréal, Canada; Raghu N. Bhattacharya, National Renewable

Energy Laboratory, Golden, Colorado; U. Sengupta, Jin Z. Zhang,
Department of Chemistry, University of California, Santa Cruz, CA.

This paper describes our recent research in developing large-area (4x4 sq. inch) lead iodide (PbI₂) quantum dot (Q-dot) films for highly sensitive optical and X-ray imaging applications. The colloidal PbI₂ nanocrystals were first synthesized in the solution phase reaction (80 v/o ethanol) of Pb-based precursors in the temperature range 25-55 degrees celcius. The synthesized nanocrystals were then isolated in sizes ranging from 12-120 Å in diameter and used for well-defined Q-dot film preparation. Free standing Q-dot PbI₂ films of thickness approximately 25 micron were deposited on ITO-coated glass substrates by the colloidal spin-casting technique and were then thoroughly investigated by X-ray diffraction, electron probe microanalysis, transmission electron microscopy, UV-Vis spectroscopy, X-ray photoelectron spectroscopy, electrical resistivity, and charge transport property measurements. A large number of X-ray and photo-detectors were fabricated using lithographic masked metallization technique. The detection properties of signal amplitude for a given X-ray energy have been measured and was found to be about 6-8 times larger as compared to standard phosphor screens used for X-ray imaging. Charge transport characteristics and timing behavior of these nanocrystalline Q-dot films under bias operation have been measured, and the results demonstrated for the first time that these films are highly promising for real-time optical and X-ray imaging applications.

MATERIALS RESEARCH SOCIETY SYMPOSIUM PROCEEDINGS

Volume 578— Multiscale Phenomena in Materials—Experiments and Modeling, I.M. Robertson, D.H. Lassila, R. Phillips, B. Devincre, 2000, ISBN: 1-55899-486-6

Volume 579— The Optical Properties of Materials, J.R. Chelikowsky, S.G. Louie, G. Martinez, E.L. Shirley, 2000, ISBN: 1-55899-487-4

Volume 580— Nucleation and Growth Processes in Materials, A. Gonis, P.E.A. Turchi, A.J. Ardell, 2000, ISBN: 1-55899-488-2

Volume 581— Nanophase and Nanocomposite Materials III, S. Komarneni, J.C. Parker, H. Hahn, 2000, ISBN: 1-55899-489-0

Volume 582— Molecular Electronics, S.T. Pantelides, M.A. Reed, J. Murday, A. Aviram, 2000, ISBN: 1-55899-490-4

Volume 583— Self-Organized Processes in Semiconductor Alloys, A. Mascarenhas, D. Follstaedt, T. Suzuki, B. Joyce, 2000, ISBN: 1-55899-491-2

Volume 584— Materials Issues and Modeling for Device Nanofabrication, L. Merhari, L.T. Wille, K.E. Gonsalves, M.F. Gyure, S. Matsui, L.J. Whitman, 2000, ISBN: 1-55899-492-0

Volume 585— Fundamental Mechanisms of Low-Energy-Beam-Modified Surface Growth and Processing, S. Moss, E.H. Chason, B.H. Cooper, T. Diaz de la Rubia, J.M.E. Harper, R. Murti, 2000, ISBN: 1-55899-493-9

Volume 586— Interfacial Engineering for Optimized Properties II, C.B. Carter, E.L. Hall, S.R. Nutt, C.L. Briant, 2000, ISBN: 1-55899-494-7

Volume 587— Substrate Engineering—Paving the Way to Epitaxy, D. Norton, D. Schlom, N. Newman, D. Matthiesen, 2000, ISBN: 1-55899-495-5

Volume 588— Optical Microstructural Characterization of Semiconductors, M.S. Unlu, J. Piqueras, N.M. Kalkhoran, T. Sekiguchi, 2000, ISBN: 1-55899-496-3

Volume 589— Advances in Materials Problem Solving with the Electron Microscope, J. Bentley, U. Dahmen, C. Allen, I. Petrov, 2000, ISBN: 1-55899-497-1

Volume 590— Applications of Synchrotron Radiation Techniques to Materials Science V, S.R. Stock, S.M. Mini, D.L. Perry, 2000, ISBN: 1-55899-498-X

Volume 591— Nondestructive Methods for Materials Characterization, G.Y. Baaklini, N. Meyendorf, T.E. Matikas, R.S. Gilmore, 2000, ISBN: 1-55899-499-8

Volume 592— Structure and Electronic Properties of Ultrathin Dielectric Films on Silicon and Related Structures, D.A. Buchanan, A.H. Edwards, H.J. von Bardeleben, T. Hattori, 2000, ISBN: 1-55899-500-5

Volume 593— Amorphous and Nanostructured Carbon, J.P. Sullivan, J. Robertson, O. Zhou, T.B. Allen, B.F. Coll, 2000, ISBN: 1-55899-501-3

Volume 594— Thin Films—Stresses and Mechanical Properties VIII, R. Vinci, O. Kraft, N. Moody, P. Besser, E. Shaffer II, 2000, ISBN: 1-55899-502-1

Volume 595— GaN and Related Alloys—1999, T.H. Myers, R.M. Feenstra, M.S. Shur, H. Amano, 2000, ISBN: 1-55899-503-X

Volume 596— Ferroelectric Thin Films VIII, R.W. Schwartz, P.C. McIntyre, Y. Miyasaka, S.R. Summerfelt, D. Wouters, 2000, ISBN: 1-55899-504-8

Volume 597— Thin Films for Optical Waveguide Devices and Materials for Optical Limiting, K. Nashimoto, R. Pachter, B.W. Wessels, J. Shmulovich, A.K-Y. Jen, K. Lewis, R. Sutherland, J.W. Perry, 2000, ISBN: 1-55899-505-6

Volume 598— Electrical, Optical, and Magnetic Properties of Organic Solid-State Materials V, S. Ermer, J.R. Reynolds, J.W. Perry, A.K-Y. Jen, Z. Bao, 2000, ISBN: 1-55899-506-4

Volume 599— Mineralization in Natural and Synthetic Biomaterials, P. Li, P. Calvert, T. Kokubo, R.J. Levy, C. Scheid, 2000, ISBN: 1-55899-507-2

Volume 600— Electroactive Polymers (EAP), Q.M. Zhang, T. Furukawa, Y. Bar-Cohen, J. Scheinbeim, 2000, ISBN: 1-55899-508-0

Volume 601— Superplasticity—Current Status and Future Potential, P.B. Berbon, M.Z. Berbon, T. Sakuma, T.G. Langdon, 2000, ISBN: 1-55899-509-9

Volume 602— Magnetoresistive Oxides and Related Materials, M. Rzchowski, M. Kawasaki, A.J. Millis, M. Rajeswari, S. von Molnár, 2000, ISBN: 1-55899-510-2

Volume 603— Materials Issues for Tunable RF and Microwave Devices, Q. Jia, F.A. Miranda, D.E. Oates, X. Xi, 2000, ISBN: 1-55899-511-0

Volume 604— Materials for Smart Systems III, M. Wun-Fogle, K. Uchino, Y. Ito, R. Gotthardt, 2000, ISBN: 1-55899-512-9

MATERIALS RESEARCH SOCIETY SYMPOSIUM PROCEEDINGS

Volume 605— Materials Science of Microelectromechanical Systems (MEMS) Devices II, M.P. deBoer, A.H. Heuer, S.J. Jacobs, E. Peeters, 2000, ISBN: 1-55899-513-7

Volume 606— Chemical Processing of Dielectrics, Insulators and Electronic Ceramics, A.C. Jones, J. Veteran, D. Mullin, R. Cooper, S. Kaushal, 2000, ISBN: 1-55899-514-5

Volume 607— Infrared Applications of Semiconductors III, M.O. Manasreh, B.J.H. Stadler, I. Ferguson, Y-H. Zhang, 2000, ISBN: 1-55899-515-3

Volume 608— Scientific Basis for Nuclear Waste Management XXIII, R.W. Smith, D.W. Shoesmith, 2000, ISBN: 1-55899-516-1

Volume 609— Amorphous and Heterogeneous Silicon Thin Films—2000, R.W. Collins, H.M. Branz, S. Guha, H. Okamoto, M. Stutzmann, 2000, ISBN: 1-55899-517-X

Volume 610— Si Front-End Processing—Physics and Technology of Dopant-Defect Interactions II, A. Agarwal, L. Pelaz, H-H. Vuong, P. Packan, M. Kase, 2000, ISBN: 1-55899-518-8

Volume 611— Gate Stack and Silicide Issues in Silicon Processing, L. Clevenger, S.A. Campbell, B. Herner, J. Kittl, P.R. Besser, 2000, ISBN: 1-55899-519-6

Volume 612— Materials, Technology and Reliability for Advanced Interconnects and Low-k Dielectrics, K. Maex, Y-C. Joo, G.S. Oehrlein, S. Ogawa, J.T. Wetzl, 2000, ISBN: 1-55899-520-X

Volume 613— Chemical-Mechanical Polishing 2000—Fundamentals and Materials Issues, R.K. Singh, R. Bajaj, M. Meuris, M. Moinpour, 2000, ISBN: 1-55899-521-8

Volume 614— Magnetic Materials, Structures and Processing for Information Storage, B.J. Daniels, M.A. Seigler, T.P. Nolan, S.X. Wang, C.B. Murray, 2000, ISBN: 1-55899-522-6

Volume 615— Polycrystalline Metal and Magnetic Thin Films—2000, L. Gignac, O. Thomas, J. MacLaren, B. Clemens, 2000, ISBN: 1-55899-523-4

Volume 616— New Methods, Mechanisms and Models of Vapor Deposition, H.N.G. Wadley, G.H. Gilmer, W.G. Barker, 2000, ISBN: 1-55899-524-2

Volume 617— Laser-Solid Interactions for Materials Processing, D. Kumar, D.P. Norton, C.B. Lee, K. Ebihara, X. Xi, 2000, ISBN: 1-55899-525-0

Volume 618— Morphological and Compositional Evolution of Heteroepitaxial Semiconductor Thin Films, J.M. Millunchick, A-L. Barabasi, E.D. Jones, N. Modine, 2000, ISBN: 1-55899-526-9

Volume 619— Recent Developments in Oxide and Metal Epitaxy—Theory and Experiment, M. Yeadon, S. Chiang, R.F.C. Farrow, J.W. Evans, O. Auciello, 2000, ISBN: 1-55899-527-7

Volume 620— Morphology and Dynamics of Crystal Surfaces in Complex Molecular Systems, J. DeYoreo, W. Casey, A. Malkin, E. Vlieg, M. Ward, 2000, ISBN: 1-55899-528-5

Volume 621— Electron-Emissive Materials, Vacuum Microelectronics and Flat-Panel Displays, K.L. Jensen, W. Mackie, D. Temple, J. Itoh, R. Nemanich, T. Trottier, P. Holloway, 2000, ISBN: 1-55899-529-3

Volume 622— Wide-Bandgap Electronic Devices, R.J. Shul, F. Ren, M. Murakami, W. Pletschen, 2000, ISBN: 1-55899-530-7

Volume 623— Materials Science of Novel Oxide-Based Electronics, D.S. Ginley, D.M. Newns, H. Kawazoe, A.B. Kozyrev, J.D. Perkins, 2000, ISBN: 1-55899-531-5

Volume 624— Materials Development for Direct Write Technologies, D.B. Chrisey, D.R. Gamota, H. Helvajian, D.P. Taylor, 2000, ISBN: 1-55899-532-3

Volume 625— Solid Freeform and Additive Fabrication—2000, S.C. Danforth, D. Dimos, F.B. Prinz, 2000, ISBN: 1-55899-533-1

Volume 626— Thermoelectric Materials 2000—The Next Generation Materials for Small-Scale Refrigeration and Power Generation Applications, T.M. Tritt, G.S. Nolas, G. Mahan, M.G. Kanatzidis, D. Mandrus, 2000, ISBN: 1-55899-534-X

Volume 627— The Granular State, S. Sen, M. Hunt, 2000, ISBN: 1-55899-535-8

Volume 628— Organic/Inorganic Hybrid Materials—2000, R.M. Laine, C. Sanchez, E. Giannelis, C.J. Brinker, 2000, ISBN: 1-55899-536-6

Volume 629— Interfaces, Adhesion and Processing in Polymer Systems, S.H. Anastasiadis, A. Karim, G.S. Ferguson, 2000, ISBN: 1-55899-537-4

Volume 630— When Materials Matter—Analyzing, Predicting and Preventing Disasters, M. Ausloos, A.J. Hurd, M.P. Marder, 2000, ISBN: 1-55899-538-2

Molecular Electronics

Organometallic Synthesis and Spectroscopic Characterization of Manganese Doped CdSe Nanocrystals

Frederic V. Mikulec,¹ Masaru Kuno,¹ Marina Bennati,² Dennis A. Hall,^{1,2} Robert G. Griffin,^{1,2} Moungi G. Bawendi¹

¹Department of Chemistry; ²Center for Magnetic Resonance, Francis Bitter Magnet Laboratory; Massachusetts Institute of Technology, Cambridge, MA 02139

ABSTRACT

For CdSe quantum dots (QDs) produced via high temperature pyrolysis in trioctylphosphine oxide (TOPO), a MnSe precursor such as $Mn_2(\mu\text{-SeMe})_2(CO)_8$ appears to be necessary to successfully incorporate low levels of Mn. A simple etching experiment and electron paramagnetic resonance (EPR) measurements reveal that most of the dopant atoms reside in the surface layers of the inorganic lattice. The dopant dramatically affects ^{113}Cd solid state NMR spectra; the observed paramagnetic shift and decreased longitudinal relaxation time reproduce bulk material behavior. Paramagnetic atoms in QDs generate large effective magnetic fields, which implies that magneto-optical experiments can be performed simply by doping. Results from fluorescence line narrowing (FLN) studies on Mn doped CdSe QDs mirror previous findings on undoped QDs in an external magnetic field. Experimental fitting of photoluminescence excitation (PLE) spectra of doped QDs reveals that the effective absorption lineshape contains a new feature which is believed to be a previously unobserved – but theoretically predicted – optically dark fine structure state.

INTRODUCTION

Although there is a large body of literature concerning transition metal doped semiconductors [1] – also called diluted magnetic semiconductors (DMS) – and there has been a flurry of activity investigating semiconductor quantum dots [2] (QDs), only recently have there been reports describing research occurring at the intersection of these two fields [3]. Of the work detailing the synthesis of DMS QDs, the majority rely on photoluminescence (PL) spectroscopy to determine if the materials have been successfully doped: below bandgap energy emission at the wavelength corresponding to the bulk material is the primary litmus test for doped nanocrystals. However, this emission only implies that electronic coupling exists between the nanocrystal and the Mn excited states. A recent report from Ladizhansky and co-workers concludes that the dopant in their CdMnS samples – prepared by the popular co-precipitation method – is either in the solvent/ligand matrix or bound to the surface of the particles [4]. In light of this result, any thorough characterization of doped QDs must include convincing structural evidence – or numerous purification steps and control experiments – that determines the true location of the dopant atoms.

By incorporating manganese into the QD one can investigate the effects of a paramagnetic dopant – and the effective magnetic field it generates – on the semiconductor properties.

EXPERIMENTAL

Synthesis. $Mn_2(\mu\text{-SeMe})_2(CO)_8$ was synthesized by adapting Coleman's procedure for making the analogous tellurium compound [5]. The product (75% yield) has an IR spectrum (carbonyl region) and a 1H NMR spectrum that match literature values for $Mn_2(\mu\text{-SeMe})_2(CO)_8$ [6]. Undoped CdSe quantum dots were synthesized according to previously described literature methods [7]. Doped nanocrystals were prepared in a similar fashion by dissolving (sonication) a small amount of precursor (2-200 mg) into the TOP injection solution. For example, the injection solution used to prepare the FLN/PLE sample consisted of 200 μL CdMe₂, 3 mL 1M TOPSe, 30 mg $Mn_2(\mu\text{-SeMe})_2(CO)_8$, and 16 mL TOP. Surface ligand exchange is performed as previously described [7b].

Electron Paramagnetic Resonance (EPR). Room temperature (300 K, 9.77 GHz) and low temperature (4.2 K, 9.44 GHz) EPR spectra were obtained using a Bruker ESP 300 instrument. Microwave powers employed were below saturation levels. Quantitative standards were prepared by adding known amounts of a manganese (II) cyclohexanobutyrate stock solution to undoped CdSe QDs in toluene. The concentrations of nanocrystals in the standard and the unknown were approximately equal. The amount of manganese added to the reaction which ended up doping the nanocrystals was generally 1% (at.) or less.

Wavelength Dispersive X-ray Spectroscopy (WDS). A JEOL SEM 733 electron microprobe operating at 15 kV was used to determine manganese concentrations. The takeoff angle to the detector was 40° and the magnification was 1000 \times . Samples were prepared by precipitating TOPO/TOPSe capped nanocrystals from solution and washing the material three times with methanol. One drop of a very concentrated pyridine solution of QDs was placed on a silicon (100) wafer, dried under vacuum at 80 °C for 24 hours, and then coated with a thin layer of carbon.

Solid-state NMR. Magic angle spinning (MAS) NMR experiments were performed using a homebuilt 211 MHz NMR spectrometer (47 MHz for ^{113}Cd) and a custom designed, two-channel transmission line probe. The ^{113}Cd $\pi/2$ pulse width was 5 μs . Hahn echo pulse sequences ($\pi/2\text{-}\tau\text{-}\pi\text{-}\tau\text{-}Acq$) were used for all spectra, with the interpulse delay τ equal to the rotor period. A 5 mm Chemagnetics spinning system (Otsuka Electronics USA) was used for MAS, with spinning frequencies of the samples varied from 6.5 to 9 kHz. Spin lattice relaxation times (T_1 values) were estimated from the recycle delays.

Optical Spectroscopy. Variable temperature fluorescence line narrowing (FLN) and photoluminescence excitation (PLE) experiments were conducted on doped and undoped QDs using a SPEX Fluorolog-2 spectrofluorometer. Samples were prepared by loading hexane solutions of TOPO/TOPSe capped nanocrystals between two sapphire flats separated by a 0.5 mm Teflon spacer. The absorbance of the lowest energy feature in all samples was kept below 1.0 to minimize reabsorption of the luminescence. The FLN experiment was conducted by choosing five energies over the full luminescence profile of the nanocrystals. In the PLE experiment the detector was fixed at the peak position of the zero phonon line and the excitation spectrometer was scanned to the blue of this position to reproduce the absorption profile of the nanocrystals.

RESULTS AND DISCUSSION

Testing Mn Precursors. CdSe nanocrystals prepared in the presence of Mn compounds (such as MnMe₂ and Mn(CO)₅Me) and then purified by pyridine ligand

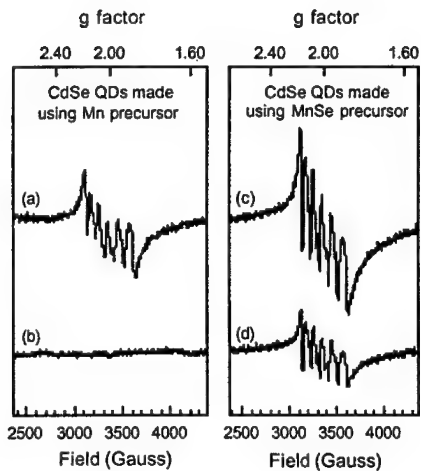


Figure 1. Low temperature (5K) EPR spectra of 40 Å diameter CdSe quantum dots prepared using (a-b) Mn precursor (c-d) the $\text{Mn}_2(\mu\text{-SeMe})_2(\text{CO})_8$ precursor.

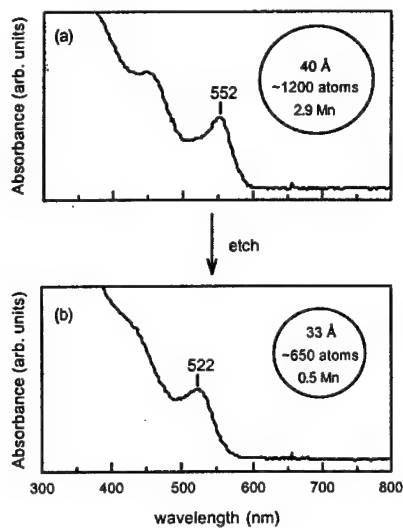


Figure 2. UV/visible absorption spectra of CdMnSe QDs (a) before and (b) after etching with tripyrrolidinophosphine oxide

exchange are not doped to a significant extent, as judged by EPR (Figure 1b). We believe that the initial Mn signals (Figure 1a) originated from loosely bound surface species or decomposition products not removed by size selective precipitation.

Doped CdSe nanocrystals were prepared using $\text{Mn}_2(\mu\text{-SeMe})_2(\text{CO})_8$ as the manganese source. Figure 1c-d displays the EPR spectra of a “MnSe” doped sample before and after the same pyridine ligand exchange purification process used for the previous “Mn” doped sample. The Mn signal of this sample remains after size selective precipitation and surface ligand exchange with pyridine (Figure 1d).

The hyperfine splitting reported for Mn in bulk cubic CdSe is $62 \times 10^{-4} \text{ cm}^{-1}$ [8]. The hyperfine splitting of the Mn doped QDs in Figure 1d is $83 \times 10^{-4} \text{ cm}^{-1}$. A report of the hyperfine splittings of Mn in ZnS nanocrystals found two separate signals, one with a hyperfine splitting $65 \times 10^{-4} \text{ cm}^{-1}$ and the other $89 \times 10^{-4} \text{ cm}^{-1}$ [9]. The smaller value, by comparison with the bulk material, was assigned to internal Mn. The larger value, by analogy to DMS with Mn in more ionic hosts (such as Li_2O), was assigned to Mn in the surface layers of the QD. Since extensive ligand exchange experiments have confirmed that manganese is actually part of the inorganic core of the quantum dots, we conclude that the large hyperfine splitting indicates the dopant atoms generally reside near the more ionic surface layer of the nanocrystals.

To further exclude the possibility that the dopant is simply on the surface of the QDs, we chemically etched a sample of 40 Å diameter CdMnSe (~ 1200 atoms) containing 2.9 Mn atoms per nanocrystal. After 2 hours stirring in neat tripyrrolidinophosphine oxide at 60 °C in air (Figure 2b) the QDs have shrunk to 33 Å, contain approximately 650 core atoms, and now have 0.5 Mn atoms per nanocrystal. Since the Mn concentration falls by 83% upon removal of about half of the outer atoms, most of the dopant atoms reside near the quantum dot surface. This finding agrees with

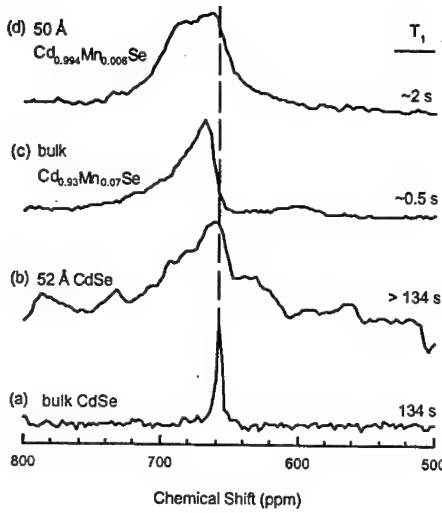


Figure 3. ^{113}Cd MAS SSNMR of (a) bulk CdSe, (b) 52 Å CdSe, (c) bulk $\text{Cd}_{0.93}\text{Mn}_{0.07}\text{Se}$, and (d) 50 Å $\text{Cd}_{0.994}\text{Mn}_{0.006}\text{Se}$.

CdSe in Figure 3a. The distribution in chemical shifts reflects the distribution of Cd atoms around the Mn center and is in excellent agreement with the line shape reported for the ^{113}Cd NMR line in bulk $\text{Cd}_{1-x}\text{Mn}_x\text{Te}$ [10]. Note that the introduction of Mn has decreased T_1 by more than two orders of magnitude. Figure 3d displays the spectrum of $\text{Cd}_{0.994}\text{Mn}_{0.006}\text{Se}$ QDs (~ 7 Mn atoms per dot). The most substantial effect of the Mn is on the spin lattice relaxation time, which has decreased from a value greater than 134 s in undoped QDs to ~ 2 s in the doped sample. The NMR spectrum (not shown) of CdSe quantum dots in which a manganese salt was simply mixed into the sample (and therefore extrinsic to the nanocrystal core) did not display these features.

Optical Spectroscopy. Previous experiments by Nirmal and co-workers have documented the effects of strong external magnetic fields (up to 10 Tesla) on both the fluorescence line narrowed (FLN) spectra and the luminescence lifetimes [11]. To see if the manganese atom has the same effect as an external field, we perform FLN spectroscopy on a doped nanocrystal sample. The complete FLN, PLE, and PL study encompasses five pairs of FLN/PLE spectra taken at each one of five different temperatures (15, 10, 5, 3, 1.75 K). WDS determined the manganese concentration of the doped sample to be 1.5 atoms per quantum dot. To investigate the subtle qualitative differences present in the raw data we employ a fitting routine to extract effective QD absorption and emission lineshapes (so-called “single dot” lineshapes) [12]. These effective lineshapes still contain inhomogeneities inherent in the FLN/PLE experiment and are not the actual lineshapes of a single quantum dot [13,14].

The fitting procedure is based upon a theoretical fine structure model [15], also known as the dark exciton model because it predicts the lowest excited state to be an optically dark exciton with angular momentum projection ± 2 . The fitting results for the undoped CdSe QDs (Figure 4a) show basically no change in the effective single dot

the EPR results (discussed above) which also indicate that the Mn is near the surface.

^{113}Cd MAS NMR. Figure 3 displays the results from MAS solid state NMR experiments [$\delta(\text{Cd}(\text{NO}_3)_2) = 0$ ppm]. Estimated spin lattice relaxation times are given at the right of each spectrum. Note the long T_1 value of 134 s for bulk CdSe powder (Figure 3a). In the case of TOPO capped CdSe QDs (Figure 3b), the line has broadened considerably and the ^{113}Cd relaxation time has increased beyond the bulk value. For the CdSe QDs dispersion in the lineshape is due to a distribution of chemical shifts present in a nanocrystal. The effects of the manganese dopant are evident in the top two spectra of Figure 3. The NMR spectrum of bulk $\text{Cd}_{0.93}\text{Mn}_{0.07}\text{Se}$ powder in Figure 3c displays both a shift and an asymmetric line shape relative to undoped bulk

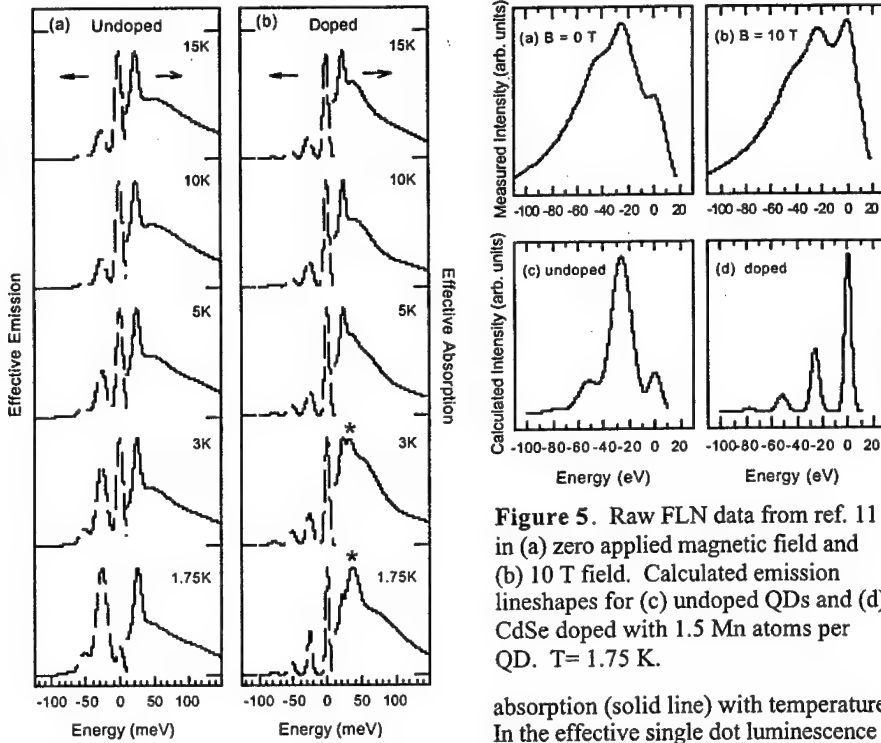


Figure 4. Effective "single dot" emission (dashed lines) and absorption (solid lines) lineshapes for (a) undoped and (b) Mn doped (~ 1.5 atoms/dot) 26 \AA CdSe QDs.

differently from undoped QDs. The effective single dot lineshapes for the doped sample (Figure 4b) display significant differences from the undoped sample in both emission and absorption. As the temperature decreases, the emission (dashed lines) shows no increase in the Huang-Rhys parameter, unlike the undoped sample. The 1PL/ZPL ratio is fairly constant over the full range of temperatures. These results show essentially the same behavior as undoped QDs in an external magnetic field.¹¹ The fact that doping with Mn is equivalent to placing the QDs within a magnetic field is illustrated in Figure 5 which displays FLN spectra and calculated lineshapes of CdSe QDs at 1.75 K under four conditions. The top two graphs of Figure 5 are experimental FLN spectra of 26 \AA CdSe (a) in zero field and (b) in a 10 Tesla field. Components of the external field perpendicular to the nanocrystal c-axis act as a perturbation to the electronic structure, effectively mixing the formally dark ± 2 emitting state with the neighboring $\pm 1^L$ exciton, making fluorescence from the ZPL the dominant pathway for radiative relaxation [11]. Increasing the magnetic field strength increases the intensity of the ZPL. The bottom two graphs of Figure 5 are calculated lineshapes of (c) undoped CdSe and (d) Mn doped CdSe. The act of doping the CdSe has increased the ZPL intensity at the expense of the 1PL. Doping the QD has produced the same effect as a magnetic field.

Figure 5. Raw FLN data from ref. 11 in (a) zero applied magnetic field and (b) 10 T field. Calculated emission lineshapes for (c) undoped QDs and (d) CdSe doped with 1.5 Mn atoms per QD. T= 1.75 K.

absorption (solid line) with temperature. In the effective single dot luminescence (dashed line), however, the ratio of the intensity of the 1PL to the ZPL increases dramatically as the temperature falls.

Doped QDs behave very

As in the emission, the effective single dot absorption spectra (solid lines) of the doped sample (Figure 4b) show different features from the undoped sample (Figure 4a). In order to obtain acceptable fits to the raw data, it was necessary to add an extra state to the standard 3 optically active levels used to model the absorption in the case of the undoped QDs. This new state manifests itself as the feature marked with an asterisk in Figure 4b. We speculate that this transition, which has not been observed before, is the formally dark 0^L exciton. This new feature appears an average of 12.4 meV away from the lowest absorbing state, whereas the calculated spacing is 5.4 meV.

REFERENCES

1. Furdyna, J. K. *J. Appl. Phys.* **1988**, *64*, R29-R64.
2. Alivisatos, A. P. *J. Phys. Chem.* **1996**, *100*, 13226-13239.
3. (a) Wang, Y.; Herron, N.; Moller, K.; Bein, T. *Solid State Commun.* **1991**, *77*, 33-38.
 (b) Dhangra, S.; Kim, K.-W.; Kanatzidis, M. G. *Mat. Res. Soc. Symp. Proc.* **1991**, *204*, 163-168.
 (c) Kim, K.-W.; Cowen, J. A.; Dhangra, S.; Kanatzidis, M. G. *Mat. Res. Soc. Symp. Proc.* **1992**, *272*, 27-33.
 (d) Yanata, K.; Suzuki, K.; Oka, Y. *J. Appl. Phys.* **1993**, *73*, 4595-4598.
 (e) Bhargava, R. N.; Gallagher, D.; Hong, X.; Nurmiikko, A. *Phys. Rev. Lett.* **1994**, *72*, 416-419.
 (f) Yanata, K.; Oka, Y. *Jpn. J. Appl. Phys.* **1995**, *Suppl 34-1*, 164-166.
 (g) Bandaranayake, R. J.; Smith, M.; Lin, J. Y.; Jiang, H. X.; Sorensen, C. M. *IEEE Trans. Magnetics* **1994**, *30*, 4930-4932.
 (h) Sooklal, K.; Cullum, B. S.; Angel, S. M.; Murphy, C. J. *J. Phys. Chem.* **1996**, *100*, 45514555.
 (i) Levy, L.; Hochepied, J. F.; Pilani, M. P. *J. Phys. Chem.* **1996**, *100*, 18322-18326.
 (j) Counio, G.; Esnouf, S.; Gacoin, T.; Boilot, J.-P. *J. Phys. Chem.* **1996**, *100*, 20021-20026.
 (k) Levy, L.; Feltin, N.; Ingert, D.; Pilani, M. P. *J. Phys. Chem. B* **1997**, *101*, 9153-9160.
4. Ladizhansky, V.; Hodes, G.; Vega, S. *J. Phys. Chem. B* **1998**, *102*, 8505-8509.
5. Coleman, A. P.; Dickson, R. S.; Deacon, G. B.; Fallon, G. D.; Ke, M.; McGregor, K.; West, B. O. *Polyhedron* **1994**, *13*, 1277-1290.
6. Welcman, N.; Rot, I. *J. Chem. Soc.* **1965**, 7515-7516.
7. (a) Murray, C. B.; Norris, D. J.; Bawendi, M. G. *J. Am. Chem. Soc.* **1993**, *115*, 8706-8715.
 (b) Kuno, M.; Lee, J. K.; Dabbousi, B. O.; Mikulec, F. V.; Bawendi, M. G. *J. Chem. Phys.* **1997**, *106*, 9869-9882.
8. Ludwig, G. W.; Woodbury, H. H. in *Solid State Physics*, vol. 13, edited by Seitz, F.; Turnbull, D.; Academic Press: New York, 1962; p 297.
9. Kennedy, T. A.; Glasser, E. R.; Klein, P. B.; Bhargava, R. N. *Phys. Rev. B* **1995**, *52*, R14356-R14359.
10. Gavish, M.; Vega, S.; Zamir, D. *Phys. Rev. B* **1993**, *48*, 2191-2199.
11. Nirmal, M.; Norris, D. J.; Kuno, M.; Bawendi, M. G.; Efros, A. L.; Rosen, M. *Phys. Rev. Lett.* **1995**, *75*, 3728-3731.
12. (a) Norris, D. J.; Efros, A. L.; Rosen, M.; Bawendi, M. G. *Phys. Rev. B* **1996**, *53*, 16347-16354.
 (b) Kuno, M. Ph.D. Thesis, Massachusetts Institute of Technology, 1998, pp 229-246.
13. Nirmal, M.; Dabbousi, B. O.; Bawendi, M. G.; Macklin, J. J.; Trautman, J. K.; Harris, T. D.; Brus, L. E. *Nature* **1996**, *383*, 802-804.
14. Empedocles, S. A.; Norris, D. J.; Bawendi, M. G. *Phys. Rev. Lett.* **1996**, *77*, 3873-3876.
15. Efros, A. L.; Rosen, M.; Kuno, M.; Nirmal, M.; Norris, D. J.; Bawendi, M. *Phys. Rev. B* **1996**, *54*, 4843-4856.

Artificial Atoms of Silicon

Justin D. Holmes, Kirk J. Ziegler, Keith P. Johnston, R. Chris Doty, Brian A. Korgel

Department of Chemical Engineering and Texas Materials Institute
The University of Texas at Austin
Austin, TX 78712-1062
Email: korgel@mail.che.utexas.edu

ABSTRACT

Size-monodisperse, stable 15 Å diameter silicon nanocrystals were synthesized in significant quantities using supercritical octanol as a capping ligand. The silicon nanocrystals exhibit an indirect band gap with discrete electronic transitions in the absorbance and photoluminescence excitation (PLE) spectra. The octanol-capped clusters show efficient blue band-edge photoemission with a luminescence quantum yield of 23 % at room temperature.

INTRODUCTION

Semiconductor cluster properties depend on size. For example, quantum confinement effects lead to unique electronic and optical properties, such as size-tunable excitation and luminescence energies with an overall loss of energy level degeneracy [1]. These distinct material properties might be exploited in a variety of new technologies—including, electronic, optical, medical, coatings, catalytic, memory and sensor applications. Because of the appearance of discrete energetic states, semiconductor clusters have been called "artificial atoms" and provide the opportunity to study semiconductor properties as they evolve from atoms to small clusters to a bulk crystal. Examples of size-dependent discrete optical transitions exist for clusters of direct band gap semiconductors, such as CdSe [2] and InAs [3]. Artificial atom behavior, however, has not previously been observed for nanocrystals of the *indirect* semiconductor, silicon—the most technologically important semiconductor [4-8].

In this study, we present the important finding that 15 Å diameter silicon clusters, synthesized in significant quantities using a supercritical (sc) solvent wet chemical approach, exhibit artificial atom qualities at room temperature.

EXPERIMENTAL DETAILS

Organic surface-passivated silicon nanocrystals were prepared by thermally degrading diphenylsilane in octanol ($T_c = 385^\circ\text{C}$, $P_c = 34.5$ bar) well above its critical point at 500 °C and 345 bar in an inconell high-pressure cell under nitrogen, as described in detail elsewhere [9]. The presence of silicon particles was observed by the formation of a yellow solution; no color change was observed in the absence of diphenylsilane. When diphenylsilane was degraded in the presence of sc-ethanol rather than sc-octanol, the solution quickly turned from orange to brown and then clear as polydisperse micron-sized silicon particles formed and settled on the walls of the reaction vessel. This result suggests that, unlike ethanol, the bound octanol chains provide sufficient steric stabilization to prevent aggregation. The sc-octanol quenches

the reaction and passivates the silicon nanocrystal surface. Chloroform was used to extract the silicon nanoparticles from the cell upon cooling and depressurization. The nanocrystal dispersion was subsequently dried and the organic-stabilized silicon nanocrystals could be redispersed in ethanol, hexane, or chloroform.

A JEOL 2010 transmission electron microscope with 1.7 Å point to point resolution operating with a 200 kV accelerating voltage with a GATAN digital photography system was used for transmission electron microscopy (TEM). In situ elemental analysis was performed on the nanocrystals using an Oxford energy dispersive spectrometer. Absorbance spectra were recorded using a Varian Cary 500 UV-Vis-NIR spectrophotometer with silicon nanocrystals dispersed in ethanol or hexane. Luminescence measurements were performed using a SPEX Fluorolog-3 spectrophotometer. Quantum yields were calculated by comparison with 9,10 Diphenylanthracene. FTIR measurements on a dried layer of silicon nanocrystals dispersed onto a zinc selenide window were achieved using a Perkin-Elmer Spectrum 2000 FTIR spectrometer.

DISCUSSION

Figure 1 shows the absorbance spectra for the silicon nanocrystals dispersed in hexane. TEM and wide-angle X-ray scattering (WAXS) indicate that the nanocrystals have a mean diameter of 15 Å [9]. EDS confirms the presence of silicon in great abundance in the sample. The absorbance (A) of the nanocrystals increases quadratically

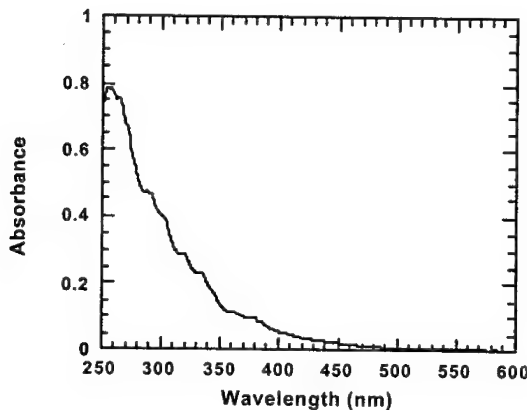


Figure 1. Absorbance spectra of the 15 Å silicon nanocrystals formed by arrested precipitation in supercritical octanol. The spectra was insensitive to solvent polarity, indicating that the absorbance is due to an exciton state and not a charge-transfer transition between bound ligands [10].

with incident energy, $A \sim [h\nu - E_g]^2$, indicating a predominantly indirect transition [11].

Both the absorbance and the photoluminescence excitation (PLE) spectra reveal several closely spaced discrete features. These results sharply contrast experimental findings for slightly larger 20 Å diameter silicon nanocrystals, which exhibited monotonically increasing featureless absorbance and photoluminescence excitation spectra [4-8]. The indirect $\Gamma \rightarrow X$ transition remains the lowest energy transition, increasing from 1.2 eV in bulk silicon to 1.9 eV. The energetic shifts observed in the absorbance spectra are quantitatively consistent with empirical pseudopotential calculations by Ramakrishna and Friesner [12].

Another notable difference in the optical properties of these nanocrystals and those synthesized in Refs. [4-8], is the strong blue band-edge photoluminescence (PL) (Figure 2). The nanocrystals photoluminesce with an overall quantum yield of 23% at room temperature. This PL signal appears to be intrinsic to the core electronic structure of silicon, with a lifetime of 2 ns. The PL is stable and does not degrade over time in the bulk sample PL measurements. In fact, the nanocrystal samples have had shelf lives of several months stored in a dessicator before noticeable changes in their optical properties. FTIR spectroscopy shows that the silicon nanocrystals are most likely alkoxide-terminated (Si-O-C) with C8 hydrocarbon chains exposed to the solvent. This organic layer forms a robust shell that prevents the surface oxidation that so readily occurs on bare silicon surfaces. FTIR of the nanocrystals dried on a CaF_2 window after thorough washing, exhibit the four characteristic methylene and terminal methyl stretching modes

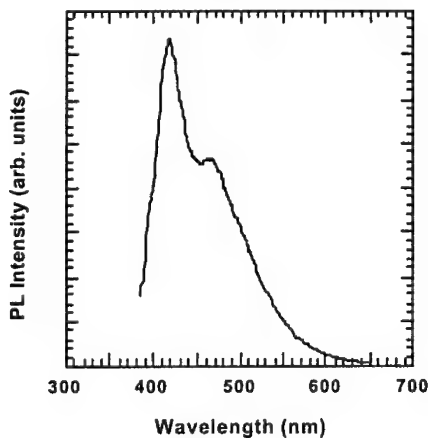


Figure 2. PL ($\lambda_{\text{ex}} = 366 \text{ nm}$) spectra of 15 Å diameter silicon nanocrystals. A very weak PL feature accounting for less than 1% of the total fluorescence quantum yield appears at 760 nm (not shown).

$\tilde{\nu}_{\text{a(CH}_3\text{)}} = 2928 \text{ cm}^{-1}$, $\tilde{\nu}_{\text{a(CH}_2\text{)}} = 2855 \text{ cm}^{-1}$, $\tilde{\nu}_{\text{a(CH}_3\text{,ip)}} = 2954.5 \text{ cm}^{-1}$,
 $\tilde{\nu}_{\text{a(CH}_3\text{,FR)}} = 2871 \text{ cm}^{-1}$, revealing that octanol is indeed adsorbed to the particle surface.
 The notable absence of the $\tilde{\nu}_{\text{(O-H)}} = 3300 \text{ cm}^{-1}$ stretch and the presence of the strong doublet corresponding to the Si-O-CH₂- stretching modes, $\tilde{\nu}_{\text{(s-OCH}_2\text{)}} = 1100-1070 \text{ cm}^{-1}$, suggests covalent bonding of octanol to the silicon nanocrystal surface [13]. The absence of the very strong characteristic aryl-silicon stretching mode, at $\tilde{\nu}_{\text{(s-ph)}} = 1125-1090 \text{ cm}^{-1}$, confirms precursor degradation. Also the lack of siloxane (Si-O-Si) peaks, at 1085 and 1020 cm^{-1} , and the strong $\tilde{\nu}_{\text{(s-cs)}} = 1080-1040 \text{ cm}^{-1}$ stretching mode eliminates the possibility that the nanoparticles are siloxane based polymers or that they consist of a Si-C core. The sc-octanol provides a robust capping ligand layer surrounding these small silicon nanocrystals that stabilizes their structure and helps to eliminate many surface traps and surface oxidation that leads to lower energy luminescence [14].

CONCLUSIONS

In conclusion, sc-octanol serves as an effective capping-solvent for the synthesis of silicon artificial atoms. Significant quantities of stable, well-passivated nanocrystals can be easily produced in each batch reaction. These silicon nanoparticles exhibit previously unobserved discrete electronic absorption and luminescence transitions due to quantum confinement effects. This study also confirms that silicon clusters containing as few as 45 atoms still behave as indirect semiconductors. The precise relationship between the fluid properties of the capping-solvent and the particle size is currently being studied.

ACKNOWLEDGEMENTS

KPJ thanks the Department of Energy and the National Science Foundation for support.

REFERENCES

1. For example, see A. P. Alivisatos, *Science* **271**, 933 (1996), and references contained therein.
2. C. B. Murray, D. J. Norris, M. G. Bawendi, *J. Am. Chem. Soc.* **115**, 8706 (1993).
3. U. Banin, et al. *J. Chem. Phys.* **109**, 2306 (1998).
4. W. L. Wilson, P. F. Szajowski, L. E. Brus, *Science* **262**, 1242 (1993); K. A. Littau, P. J. Szajowski, A. J. Muller, A. R. Kortan, L. E. Brus, *J. Phys. Chem.* **97**, 1224 (1993); L. E. Brus, et al., *J. Am. Chem. Soc.* **117**, 2915 (1995); L. Brus, *J. Phys. Chem.* **98**, 3575 (1994).
5. J. R. Heath, *Science* **258**, 1131 (1992); P. E. Batson and J. R. Heath, *Phys. Rev. Lett.* **71**, 911 (1993).
6. R. A. Bley and S. M. Kauzlarich, *J. Am. Chem. Soc.* **118** 12461 (1996); C.-S. Yang, R. A. Bley, S. M. Kauzlarich, H. W. Lee, G. R. Delgado, *J. Am. Chem. Soc.* **121**, 5191 (1999).

7. T. van Buuren, L. N. Dinh, L. L. Chase, W. J. Siekhaus, L. J. Terminello, *Phys. Rev. Lett.* **80**, 3803 (1998).
8. J. P. Wilcoxon, G. A. Samara, *Appl. Phys. Lett.* **74**, 3164 (1999).
9. J. D. Holmes, K. J. Ziegler, K. P. Johnston, R. C. Doty, B. A. Korgel, submitted for publication.
10. N. Herron, J. C. Calabrese, W. E. Farneth, Y. Wang, *Science* **259**, 1426 (1993).
11. S. M. Sze, *Physics of Semiconductor Devices*, (Wiley, New York, 2nd ed., 1981).
12. M. V. Ramakrishna and R. A. Friesner, *J. Chem. Phys.* **96**, 873 (1992)
13. Pretsch, Clerc, Seibl, Simon, Tables of Spectral Data for Structure Determination of Organic Compounds (Springer-Verlag, Berlin, 1942); G. Socrates, Infrared Characteristic Group Frequencies Tables and Charts (John Wiley & Sons, New York, 1994).
14. M. V. Wolkin, J. Jorne, P. M. Fauchet, G. Allan, C. Delerue, *Phys. Rev. Lett.* **82**, 197 (1999).

Room Temperature Negative Differential Resistance in Nanoscale Molecular Junctions

J. Chen¹, W. Wang¹, M. A. Reed¹, A. M. Rawlett², D. W. Price², J. M. Tour²

¹Department of Electrical Engineering, Yale University, P.O. Box 208284, New Haven, CT 06520

²Center for Nanoscale Science and Technology, Rice University, MS 222, 6100 Main Street, Houston, TX 77005

ABSTRACT

Molecular devices utilizing active self-assembled monolayer (SAM) (containing nitroamine (2'-amino-4-ethynylphenyl-4'-ethynylphenyl-5'-nitro-1-benzenethiolate) and nitro (4-ethynylphenyl-4'-ethynylphenyl-2'-nitro-1-benzenethiolate) redox center) as the active component are reported. Current-voltage measurements of the devices exhibited negative differential resistance at room temperature and an on-off peak-to-valley ratio in excess of 1000:1 at low temperature.

The discovery of negative differential resistance (NDR) in semiconductor diodes opened a new chapter in semiconductor device physics [1]. The physical basis of the Esaki diode is interband tunneling between the valence band and the conduction band. NDR can also result from resonant tunneling in semiconductor heterostructures [2]. The presence of NDR at room temperature allows for many practical applications [3, 4, 5]. Here we report the observation of large NDR behavior, and room temperature operation, in an electronic device that utilizes molecules as the active component.

Electronic measurements were performed in a nanostructure consisting of top metal contact (Au) - self-assembled monolayer (SAM) active region (30 to 50 nm in

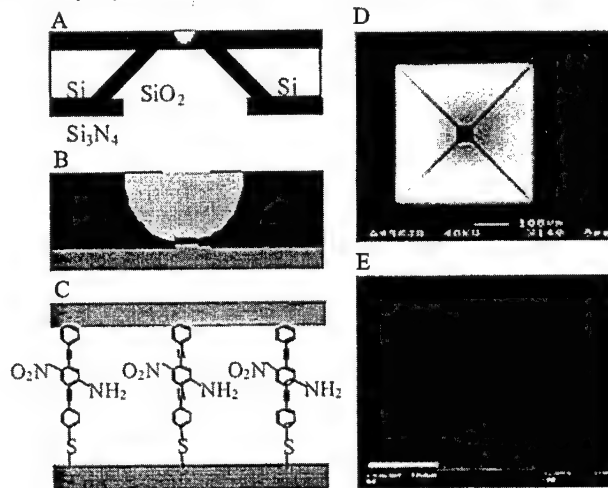


Figure 1. Schematics of device fabrication: (A) cross section of a silicon wafer with a nanopore etched through a suspended silicon nitride membrane; (B) Au-SAM-Au junction in the pore area; (C) blowup of (B) with 1 sandwiched in the junction; (D) scanning electron micrograph (SEM) of pyramid Si structure after unisotropic Sietching (that is, the bottom view of (A)); (E) SEM of an etched nanopore through the silicon nitride membrane.

diameter) - bottom metal contact (Au), similar to that reported previously [6,7]. The active electronic component was made from 2'-amino-4-ethynylphenyl4'-ethynylphenyl-5'-nitro-1-(thioacetyl)benzene (**1a**) that was prepared as outlined in Figure 1.

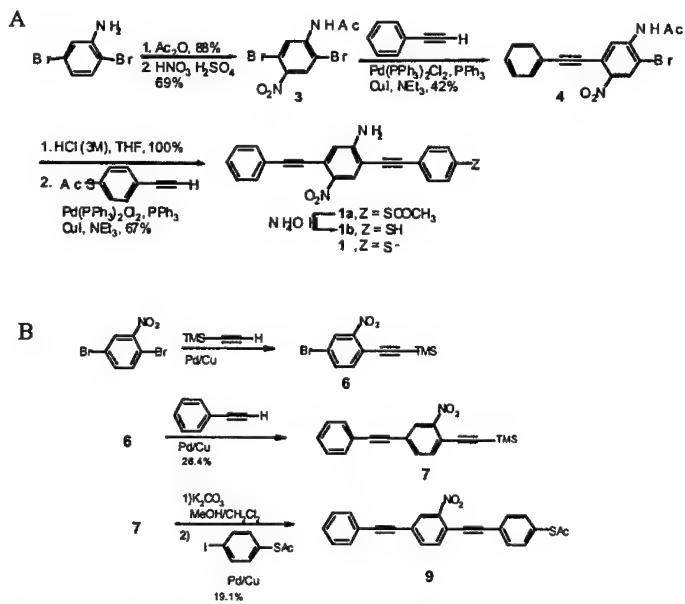


Figure 2. (A) Schematic of the synthesis of the active molecular compound and its precursors (**1a-b** and **1**); (B) schematic of the synthesis of the active molecular compound **2**.

Acylation and nitration of 2,5-dibromoaniline afforded **3** [8] which underwent Pd/Cu-catalyzed coupling [9] with phenylacetylene preferentially at the more electrophilic C-Br site to yield **4**. Acetate hydrolysis and coupling with 4-ethynyl(thioacetyl)benzene [10] afforded the desired compound **1a**. As we established previously, thioacetyl groups can be selectively hydrolyzed with ammonium hydroxide in tetrahydrofuran (THF) during the self-assembly step to afford the free thiol, 2'-amino-4-ethynylphenyl4'-ethynylphenyl-5'-nitro-1-benzenethiol (**1b**) in this case. The assembly likely forms the thiolate (**1**: 4-ethynylphenyl4'-ethynylphenyl-5'-nitro-1-benzenethiolate) upon exposure to Au [11]. The other redox center containing molecular compound we used in this study is 2'-amino-4-ethynylphenyl4'-ethynylphenyl-5'-nitro-1-benzenethiolate (**2**). Its synthesis is shown in Figure 2B. 2,5-Dibromonitrobenzene was coupled to trimethylsilylacetylene (TMS)

under Sonogashira coupling conditions using bis(triphenylphosphine)palladium(II) chloride, copper(I) iodide, and diisopropylethylamine in THF. Product 7 was isolated and the TMS protected alkyne was deprotected to the terminal alkyne by stirring with potassium carbonate and methanol in methylene chloride for 2 hrs at room temperature. This product was taken on to the final Sonogashira coupling with 4-thioacetyl-iodobenzene to afford the molecule 9.

Typical I(V) characteristics of a Au-(1)-Au device are shown in Figure 3. Positive bias corresponds to hole injection from the chemisorbed thiol-Au contact and electron injection from the evaporated contact. At 60 K, the peak current density for this device was $> 53 \text{ A/cm}^2$, the NDR is $< 380 \mu\Omega\text{-cm}^2$, and the peak-to-valley ratio (PVR) is 1030:1. Unlike previous devices that also used molecules to form the active region [12],

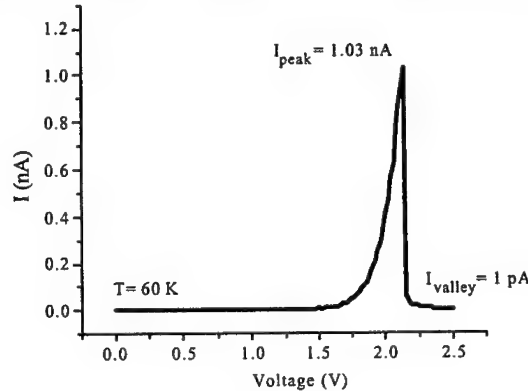


Figure 3. I(V) characteristics of a Au-(2'-amino-4-ethynylphenyl-4'-ethynylphenyl-5-nitro-1-benzenethiolate)-Au device at 60 K. The peak current density is $\sim 50 \text{ A/cm}^2$, the NDR is $\sim 400 \mu\Omega\text{-cm}^2$, and the PVR is 1030:1.

this device exhibits a robust and large NDR. The I(V) curve is fully reversible upon change in bias sweep direction; for a given device, small fluctuations ($\sim 1\%$ in voltage peak position and $\sim 6\%$ in peak current) were observed with consecutive positive and negative sweeps but could be attributed to temperature fluctuations of $\sim 2\text{K}$ (within the experimental thermal stability). The performance exceeds that observed in typical solid state quantum well resonant tunneling heterostructures [13-16]. In addition to the obvious size advantages for scaling, the intrinsic device characteristics (that is, the valley current shutoff) may be superior to that of solid state devices. The intrinsic PVR of the molecule may be considerably greater than that reported here, because the valley currents observed (on the order of picoamperes) are comparable to typical leakage currents in the silicon nitride.

A candidate mechanism for NDR is a two-step reduction process that modifies charge transport through the molecule (as shown in Figure 4). As the voltage is increased, the molecule initially undergoes a one-electron reduction, thereby supplying a charge carrier for electron flow through the system (although the nitro moiety is the most

electron-withdrawing group in the molecule, the charge is likely dispersed throughout the entire molecule). A further increase in voltage causes a second-electron reduction with

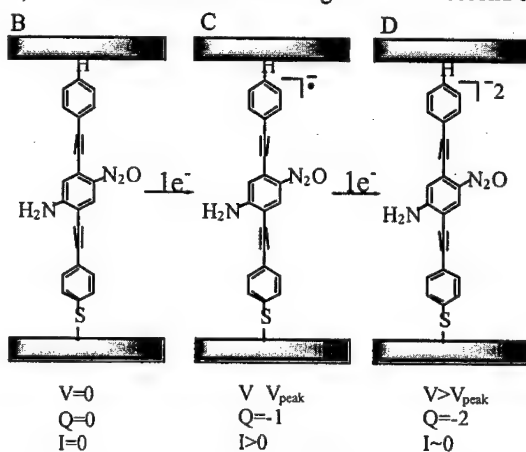


Figure 4: Potential mechanism for the NDR effect. As voltage is applied, the molecules in the SAM (A) undergo a one-electron reduction to form the radical anion (B) that provides a conductive state. Further increase of the voltage causes another one-electron reduction to form the dianion, insulating state (C). Q is the charge.

subsequent blocking of the current. The width of the $I(V)$ peak (~ 0.7 V) correlates well with the difference between the one-electron and two-electron peak reduction potentials ($E_{p2} - E_{p1} = \Delta E_p = 0.63$ V and 0.68 V for **1** with $Z = \text{SCH}_3$ and $Z = \text{H}$, respectively)[17]. The NDR behavior is absent in both the control molecule (no amine or nitro moieties) [12], indicating that the nitroamine redox center is responsible for the NDR behavior of the devices. Theory to explain the temperature dependencies and future experimental work such as optical response and other time dependencies should elucidate the transport mechanisms that would further permit engineering of device performance for larger PVR at room temperature. The NDR observation cannot be explained by the Coulomb blockade of interstitial metal particles because two-terminal localized state transport gives rise to current steps [18] and not switching behavior.

Similar NDR behavior was also observed in devices with nitro only moiety (**2**).

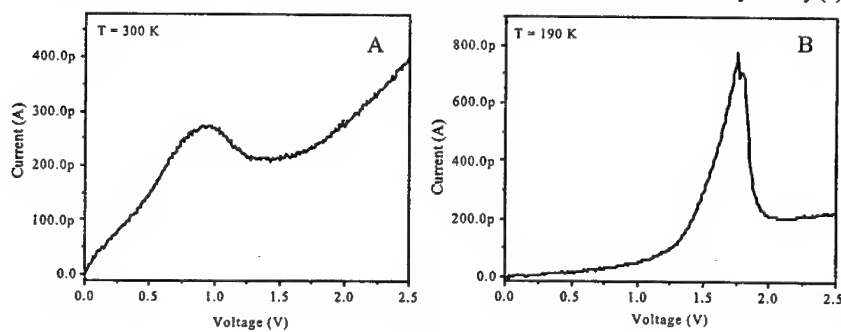


Figure 5. I(V) characteristics of a Au-(4-ethynylphenyl-4'-ethynylphenyl-5'-nitro-1-benzenethiolate)-Au device (A): at 300 K; (B): at 190 K.

The PVR is smaller than that of **1**, but NDR behavior persisted from low temperature to room temperature. I(V) characteristics of a Au-(2)-Au device at 300 K is shown in Figure 5A. The device has a peak current density $> 16 \text{ A/cm}^2$, $\text{NDR} < 144 \text{ m}\Omega \cdot \text{cm}^2$ and a PVR $\sim 1.5:1$. At 190 K (shown in Figure 5B), the NDR peak is much sharper, although its PVR is not as big as that of **1**. The degradation in PVR (decreasing in peak current) could possibly be due to increased scattering with increasing temperature. The reduction potential difference for this molecule is also roughly equal to the width of the I(V) peak. Further understanding of the underlying mechanism and experimentation with various redox centers should allow us to engineer molecular compounds in the future to improve PVR at room temperature and above.

ACKNOWLEDGEMENTS

The authors would like to thank Robert G. Wheeler for stimulating discussions. This work was supported by DARPA through ONR under grant N00014-99-1-0406.

REFERENCES

1. L. Esaki, Phys. Rev. **109**, 603 (1958).
2. L. L. Chang, L. Esaki, R. Tsu, Appl. Phys. Lett. **24**, 593 (1974).
3. T. C. L. G. Sollner *et al.*, Appl. Phys. Lett. **43**, 588 (1983).
4. M. Tsuchiya, H. Sakaki, J. Yoshino, Jpn. J. Appl. Phys. **24**, L466 (1985).
5. S. M. Sze (Eds), *High-Speed Semiconductor Devices*, (Wiley, New York, 1990).
6. C. Zhou *et al.*, Appl. Phys. Lett. **71**, 611 (1997).
7. J. Chen, M. A. Reed, A. M. Rawlett, J. M. Tour, Science **286**, 1550 (1999).
8. M. Moroni *et al.*, Macromolecules **1997**, *30*, 1964.
9. K. Sonogashira, Y. Tohda, and N. Hagihara, Tetrahedron Lett. **4467** (1975).
10. D. L. Pearson and J. M. Tour, J. Org. Chem. **62**, 1376 (1997).
11. J. M. Tour *et al.*, J. Am. Chem. Soc. **117**, 9529 (1995).
12. C. Zhou, thesis, Yale University (1999).
13. J. H. Smet, T. P. E. Broekaert, and C. G. Fonstad, J. Appl. Phys. **71**, 2475 (1992).
14. J. R. Söderström, D. H. Chow, and T. C. McGill, J. Appl. Phys. **66**, 5106 (1989).
15. J. Day *et al.*, J. Appl. Phys. **73**, 1542 (1993).
16. H. H. Tsai *et al.*, IEEE Elec. Dev. Lett. **15**, 357 (1993).
17. The case where Z = SH was avoided due to anomalies that could be caused through electrochemical disulfide formation and cleavage events.
18. M. R. Deshpande *et al.*, Phys. Rev. Lett. **76**, 1328 (1996).

Transport Calculations in Molecular Devices from First Principles

M. DI VENTRA¹, N.D. LANG² AND S.T. PANTELIDES¹

¹DEPARTMENT OF PHYSICS AND ASTRONOMY, VANDERBILT UNIVERSITY, NASHVILLE, TN 37235

²IBM RESEARCH DIVISION, THOMAS J. WATSON RESEARCH CENTER, YORKTOWN HEIGHTS, NY 10598

ABSTRACT

For molecular electronics, Boltzmann's equation is no longer valid for simulating device characteristics. We present the first fully *ab initio* simulation of a molecular device that has already been studied experimentally, namely a benzene-1,4-dithiolate molecule between gold electrodes. The theoretical I-V curve has the same overall shape as the experimental curve – reflecting the electronic structure of the molecule in the presence of the electric field – but the absolute value of the current is very sensitive to contact chemistry and geometry. In particular the presence of a single gold atom between the molecule and the electrode surface reduces the conductance by more than an order of magnitude. Replacement of the single gold atom by an aluminum atom, whose *p* orbitals couple more effectively to the molecule's π orbitals, increases the conductance by about an order of magnitude. We have also studied the polarization effects induced by a third terminal (gate) on the I-V characteristics of the above device. In particular, we have found that current gain due to the gate bias can be achieved at reasonable gate fields. Finally the effect of current-induced forces on the device will be discussed.

INTRODUCTION

Devices made from single molecules are currently considered as a possible alternative to achieve the ultimate miniaturization below 10 nm, where Si-based microelectronics is believed to fail, in the next 10-15 years. Prototypes have already been fabricated. Reed *et al.* [1] reported I-V characteristics of single benzene-1,4-dithiolate molecules. Alivisatos and coworkers [2] reported similar I-V characteristics of semiconductor and metal nanoclusters between gold electrodes. Dekker and coworkers [3] reported transistor-like behavior in carbon nanotubes. Similar devices have been demonstrated by Avouris and coworkers using single- and multi-walled carbon nanotubes. [4]

Theoretical modeling played a key role in the invention of the transistor and in the subsequent development of integrated circuits. Device modeling continues to provide indispensable input to circuit modeling for designing logic and memory chips and microprocessors. It is based on a “semiclassical approximation” that treats electrons and holes as classical particles except that their kinetic energies are determined by the semiconductor energy bands, most commonly in the effective-mass approximation. In this scheme, transport is governed by Boltzmann's equation. Most industrial modeling is done in the drift-diffusion approximation, to a lesser extent in the higher-order hydrodynamic approximation, and, at times, by solving the Boltzmann's equation directly by Monte Carlo techniques. [5] For nanodevices, however, when quantum phenomena are dominant, the semiclassical Boltzmann's equation does not apply. Quantum mechanical simulations are needed. So far, only semiempirical approaches have been employed to investigate transport

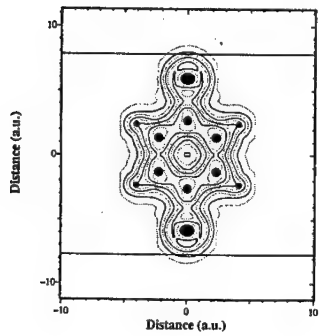


Figure 1: Contour plot of the electron density of the molecule described in the text. The dots represent the positions of the atoms. The lines represent the position of the model metal surfaces.

in molecular systems, providing useful insights into the fundamental mechanisms. [6, 7, 8, 9]

In this paper we describe first-principles calculations of the I-V characteristics of the benzene-1,4-dithiolate molecule [10] for which experimental data are available. [1] We find that when the molecule is placed between two electrodes made of an ideal metal (homogeneous electron gas or jellium model [11]), the shape of the I-V characteristic is determined by the electronic structure of the molecule in contact with the electrodes and in the presence of the external electric field. The shape is essentially the same as that of the experimental curve. The absolute magnitude of the current, however, is more than two orders of magnitude larger than the experimental value. We investigated the origins of this discrepancy and found that insertion of a single gold atom at each metal-molecule contact, as suggested by the experimental setup, leaves the shape of the I-V characteristic globally unchanged, but reduces the absolute value of the current by more than an order of magnitude, reflecting reduced coupling between the s states of the gold and the orbitals of the molecule. Replacement of the single gold atoms by aluminum atoms, which have p orbitals in the relevant energy region, raises the value of the current by about one order of magnitude. Other factors that can affect the absolute value of the current are discussed later in the paper.

We have also studied the polarization effect on the transport properties of the benzene-1,4-dithiolate molecule. We have found that a polarization field oriented perpendicular to the transport direction would provide current amplification. In particular we have shown that a) the molecule operates as a resonant tunneling transistor, and b) no charging effect is present in the molecule since only a fraction of the electron charge accumulates in the molecular region. This extra charge does not spend enough time in the device to prevent

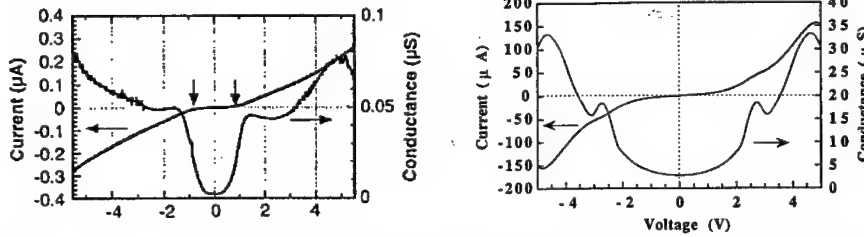


Figure 2: Left panel: Experimental I-V characteristic of a benzene-1,4-dithiolate molecule measured by Reed *et al.* [1]. Right panel: Conductance of the molecule of Fig. 1 as a function of the external bias applied to the metallic contacts.

additional charge from entering the active region of the device.

Finally we have investigated the effect of current-induced forces on the molecule. We found that the molecule twists around the axis perpendicular to its plane when the bias increases. Furthermore, the molecule undergoes a “breathing oscillation” at the first resonant tunneling condition. These effects, however, do not substantially alter the conductance through the molecule.

These results show that such calculations can provide valuable quantitative information to help design molecular devices.

THEORETICAL METHOD

We assume that all relevant scattering processes occur in a region of space defined by the presence of the nanostructure, e.g., the region of space that includes a molecule or a nanocluster. Far away from this region the electrons are provided by a reservoir that for practical purposes will be described by certain boundary conditions. The electrons are then assumed to be traveling in the bare electrodes without further scattering until they reach the relevant scattering region of space. The physical situation we are thus trying to represent corresponds to a two-probe experimental condition.

In order to easily enumerate the scattering states of impinging electrons we choose to represent the bare electrodes by a uniform-background model (jellium with a background density specified by a certain radius r_s). [11] In order to have current flowing into the structure the right and left Fermi levels are kept at a finite potential difference. Assuming that equilibrium has been reached (steady-state condition), deep within the right and left electrodes charge neutrality must be satisfied. The latter implies that the total effective potential (sum of the electrostatic and exchange-correlation potentials) is constant deep within each electrode. The current calculation then proceeds in the following way: First, within density functional theory, the single-particle wavefunctions and self-consistent electron densities are determined for the bare metallic electrodes in the presence of the bias voltage. Next, a Lippmann-Schwinger equation is solved to obtain a single-particle wave function for the total system, consisting of the two electrodes plus the structure of interest between them. Exchange and correlation are included in the density-functional formalism within the local-density approximation. [12] The electron wave functions are computed by solving the Lippmann-Schwinger equation iteratively to self-consistency in steady state. [13] The current is computed from the wave functions of the electrode-molecule system. The differential conductance is then calculated as the derivative of the current with respect to

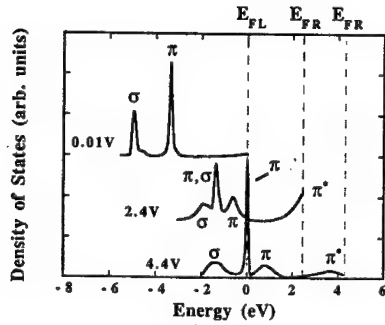


Figure 3: Difference between the density of states of the two semi-infinite electrodes with and without the benzene-1,4-dithiolate molecule in between, for three different voltages. The left Fermi level (E_{FL}) has been chosen as the zero of energy. The labels E_{FR} correspond to the energy position of the right Fermi levels. The three curves correspond to the bias voltages indicated.

the external bias. Finally current-induced forces are calculated via a Hellmann-Feynman-like theorem that applies to steady-state current conditions. [14]

DISCUSSION

TWO-TERMINAL DEVICE

We begin with the study of the I-V characteristic of a single benzene-1,4-dithiol molecule between two ideal metallic contacts. [10] It is well known that when the benzene-1,4-dithiol molecule is adsorbed on gold surfaces, the H of the thiol terminations desorbs and the sulfur atoms at each end bond strongly to the Au (111) surfaces. [15] The remaining molecule (benzene-1,4-dithiolate) is then simply the one represented in Fig. 1 where we show the contour plot of the electronic density in the benzene ring plane. The molecule has π bonding and π^* antibonding orbitals formed by the carbon and sulfur p orbitals perpendicular to the ring plane and σ bonds due to the in-plane s and p orbitals of the atoms. The electron density of the jellium electrodes is taken equal to the value for metallic gold ($r_s \approx 3$).

The calculated I-V characteristic is shown in the left panel of Fig. 2. The experimental curve is also shown for comparison in Fig. 2. It is clear that the shapes of the two curves are similar, but the absolute magnitude of the current and conductance are quite different. We will first discuss the origins of the shape and then address the question of absolute values.

We focus on three distinct regions in the calculated conductance curve: the initial rise (from zero bias to about 1V), the first peak at 2.4V and the second peak at 4.4V. In Fig. 3 we show the calculated density of states of the molecule for three different voltages, namely 0.01, 2.4, and 4.4V (the density of states shown is the difference between that of the molecule-electrodes system and that of the electrodes without the molecule). The zero of energy is the left Fermi level so that the right Fermi level is equal to the external bias (in Fig. 3 the labels E_{FR} correspond to the 2.4 and 4.4V values of the bias).

The initial slow rise of the conductance, which is also present in the experimental data,

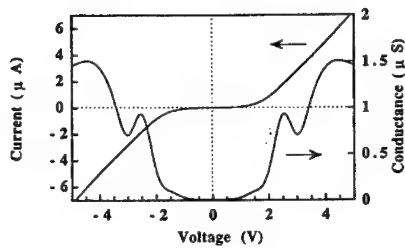


Figure 4: Conductance of the molecule of Fig. 1 with one Au atom between the model metal surface and the sulfur for each contact as a function of the external bias applied to the metallic contacts.

represents basically ohmic behavior. Fig. 3 (top curve) shows that the molecule has a small but relatively smooth density of states through which current can flow. The σ and π bonding states lie several eV below the Fermi energy so that a considerable bias is needed to produce nonlinear behavior.

After the initial increase of the current with increasing bias, a first conductance peak and subsequent valley are observed. This is also observed experimentally, though at somewhat lower voltages and with a smaller peak-to-valley ratio. The peak and the valley are due to *resonant tunneling* through π^* *antibonding* states, which are the first to appear in the window of energy between the right and left Fermi levels (see Fig. 3, middle curve). Note also that the bonding σ and π states are altered significantly by the bias simply because the different atoms of the benzene ring are at different potentials.

Increasing the bias further, a second peak is found due to resonant tunneling with π *bonding* states. From Fig. 3 it is evident that the π^* *antibonding* states are still present in the energy region between the right and left Fermi levels but with a lower peak ratio with respect to the π *bonding* states. The discrepancy between the theoretical and experimental peak positions is consistent with known limitations of the local-density approximation. [16]

The different scattering processes that occur for different biases can be studied in more detail by looking at the local density of states along the direction of current flow. The local density of states integrated between the left and right Fermi levels for small bias, is plotted in Fig. 5A. As in the case of the total density of states, we plot here the difference between the local density of states of the molecule-electrodes system and that of the electrodes without the molecule. It is evident that the sulfur-to-metal contact has a very low density of states, in effect constituting a barrier through which electrons must tunnel. After tunneling through this barrier, the electrons encounter a region of relatively smooth, higher density of states corresponding to the states of the molecule. For biases in the neighborhood of 2.5V (Fig. 5B), the electrons find a much larger density of states originating from the π^* *antibonding* states of the molecule (resonant tunneling condition). The antibonding region is between the middle carbons of the molecule. Finally, with a further increase of the bias, to the range of 5V, resonant tunneling occurs through bonding states of the molecule (see Fig. 5C).

At the first resonance condition at about 2.5V, electrons experience a higher number of

scattering events than at other biases because the depletion of states between the central carbon atoms (Fig. 5B) plays the role of an extra barrier for electrons. This effect is reflected in the time a single electron spends scattering through the device. An estimate of this time is given by (in units for which $\hbar = 1$)

$$\tau = \frac{d\delta}{dE} = \pi \Delta D(E), \quad (1)$$

where δ is the phase shift induced by the molecule scattering potential, and $\Delta D(E)$ is the difference of the density of states between the whole molecule-electrodes system and the bare electrodes. [17] The maximum delay occurs at the bias corresponding to the first resonance condition. At this bias, the electrons spend enough time in the molecule to couple to the vibrational modes. The lowest vibrational mode period of the molecule corresponds to the C-H stretching mode and is about 11fs which is comparable with the time delay at the first resonance. Inclusion of the vibrational coupling would smear out the peak and generate a lower peak-to-valley ratio in the I-V characteristic, bringing closer the agreement between theory and experiment.

We now turn to the absolute value of the current which differs by more than two orders of magnitude from the experimental value. We attribute part of this discrepancy to the contact geometry and chemistry. The experiment by Reed *et al.* [1] suggests that the contacts are atomically terminated, which means that the sulfur atoms are attached to *single* Au atoms. We investigated the effect of such a possibility on the I-V characteristic by introducing a single gold atom between the sulfur and the model metal surface at each contact. The shape of the I-V characteristic (Fig. 4) remains essentially the same, but the absolute value of the conductance *decreases* by more than an order of magnitude. This reduction is partly due to the constriction resistance generated by the *geometry* of the contact and partly to the *chemistry* of the contact between the gold and the sulfur atom. The Au atoms contribute *s* states at the Fermi level while the sulfur atoms that attach to them contribute *p* states. Only the *p* states that are perpendicular to the electrode surfaces can couple, by symmetry, to the *s* states of the gold atoms, forming σ bonds. The *p* states of the sulfur atoms that are parallel to the metal surfaces do not couple to the gold *s* states, thus breaking the π scattering channel that connects the electrode to the main benzene ring. The gain in resistance is thus mainly due to the type of contacts. This conclusion is confirmed by a calculation where the single gold atoms at the contacts are replaced by aluminum atoms. For a bias of 0.01V the resistance changes from 96 M Ω to 2.9 M Ω . The Al atoms can now contribute with *p* orbitals at the Fermi level that are parallel to the electrode surface and form π states with the *p* orbitals of the sulfur atoms similarly oriented. Finally, we performed a test calculation by positioning the S atom in front of the center of a triangular pad of three gold atoms on each electrode surface. This simulates a S atom on top of a Au(111) surface. The calculated resistance is nearly the same as the one for the sulfur attached to the model metal. The reason for this is that the *s* states of each Au atom in the pad form one state of *s* symmetry and two states of *p* symmetry parallel to the surface of the electrodes that can couple to the corresponding sulfur *p* state.

THREE-TERMINAL DEVICE

We investigate now the effects of a polarization field in the direction perpendicular to the current flow. To do this, a third terminal is introduced in the form of a capacitor field generated by two circular charged disks at a certain distance from each other placed

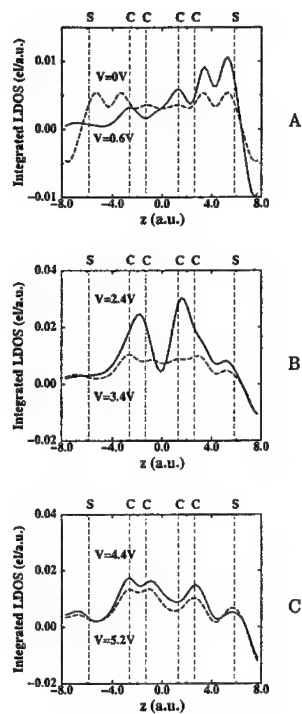


Figure 5: Local density of states (integrated in a plane parallel to the metal surfaces) difference between that of the molecule-electrodes system and that of the electrodes without the molecule, integrated between left and right Fermi levels. Voltage region A corresponds to the linear response regime. Region B corresponds to the first resonant tunneling and region C to the second resonant tunneling bias conditions.

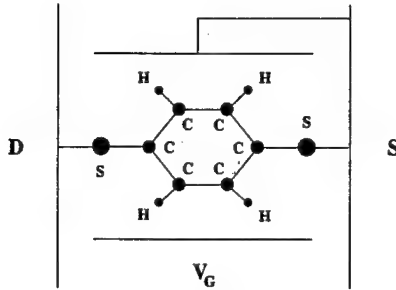


Figure 6: Scheme of the three-terminal geometry used in the present study. The molecule is sandwiched between source and drain electrodes along the direction of electronic transport. The gate electrodes are placed perpendicular to the molecule plane. One of the gate electrodes is kept at the same energy as the source Fermi level while the other electrode is at a higher potential V_G .

perpendicular to the transport direction. The disks are kept at a certain potential difference with one of the two disks at the same potential energy as the source Fermi level (see Fig. 6). The axis of the cylindrical capacitor is on the plane of the benzene ring. Since in practical realizations of this device the gate could be of different form and size we discuss the results in terms of applied gate field along the axis of the capacitor. The calculated I-V characteristic as a function of the gate bias is shown in Fig. 7. The source-drain voltage difference has been fixed at 10 mV. After a region of nearly constant current, the current increases with the gate field, reaches a maximum value at $1.1 \text{ V}/\text{\AA}$, then decreases till about $1.5 \text{ V}/\text{\AA}$, to increase further afterwards linearly. The different features of the I-V curve can be understood by looking at the density of states for different gate voltages. The initial slow rise of the conductance represents basically ohmic behavior. It is also observed experimentally for the two-terminal geometry. [1, 10] Fig. 8 (top curve) shows that the molecule has a small but relatively smooth density of states through which current can flow. The σ and π bonding states lie several eV below the Fermi levels while the π^* antibonding states are nearly 1 eV above the Fermi levels.

After the initial increase of the current with increasing gate bias, a first conductance peak and subsequent valley are observed. The peak and the valley are due to *resonant tunneling* through π^* *antibonding* states. The antibonding states thus shift in energy and eventually enter into resonance with the states between the right and left Fermi levels, separated by 10 meV (middle curve of Fig. 8). The gap between the π and π^* states decreases about 1 eV at resonance. Increasing the bias further (bottom curve of Fig. 8), the resonant-tunneling condition is lost and a valley in the I-V characteristic is observed. Finally, as the gate bias is increased further the current starts to increase with the gate bias. The peak-to-valley ratio of the present system is however 1.4 which is probably so small that it would be washed out by the vibrational coupling with the modes of the molecule. This has already been argued in the two-terminal geometry case [10]: the peak-to-valley ratios observed experimentally in the present system for the two-terminal geometry are considerably smaller than theoretically predicted (see discussion above). [1, 10]

The value of the gate field at which resonant tunneling occurs ($\approx 1 \text{ V}/\text{\AA}$) seems slightly

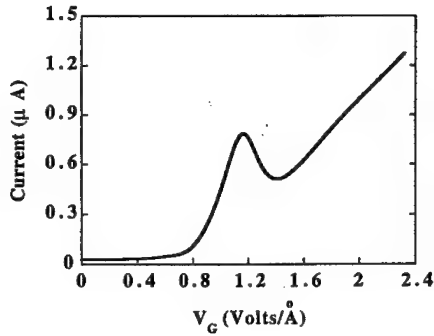


Figure 7: Conductance of the molecule of Fig. 1 as a function of the external gate field. The source-drain bias is 0.01V.

high for a molecule of nominal length of 8 Å. Two observations are however in order: i) we have previously shown [10] that the theoretical peak of transmission due to π^* antibonding states occurs at *higher* external bias than the experimental one. ii) In a practical realization of the device the capacitance field would certainly leak into the source and drain electrodes, providing a pocket of electrons with higher kinetic energy to tunnel, thus reducing the gate bias value at which the resonance occurs. Both above remarks give us confidence that resonant tunneling and amplification can occur at lower gate field.

The resistance at zero gate bias is about 360 kΩ. At 1.1 V/Å its value changes to 12.7 kΩ. The amplification is more than one order of magnitude. The peak value is close to the single-channel resistance of 12.9 kΩ (spin included). At resonance the lowest π^* antibonding state cuts exactly the narrow window of states defined by the right and left Fermi level providing a single channel for electrons to tunnel. We stress that this value could not be obtained without a self-consistent approach: the transmission coefficient of the channel is not necessarily unity, [6] and strongly depends on the chemistry and geometry of the contacts. Finally, no charging effect is present in the I-V characteristics. The electrons do not spend enough time in the device to charge it. At small gate fields (where Coulomb blockade could be effectively observed) the delay time is about 2fs. In this time only a charge of 0.04 |e| is present in the molecular region between the source and drain electrodes comprised between the right and left Fermi levels. The transport in the channel thus occurs by elastic tunneling and no Coulomb blockade is present.

CURRENT-INDUCED FORCES

The effect of forces on the two-terminal molecular device have been investigated in the case of the molecule connected to two bare electrode metals. The current flow has essentially two effects on the atomic structure: i) the molecule twists around the axis perpendicular to its plane, ii) the molecule expands at the bias for which the first resonant tunneling condition occurs then contracts at about 2.8V corresponding to the valley of Fig. 2. The first effect increases with increasing bias even though the global current is not substantially altered. The second effect is due to the deplation of charge between the central C atoms (see Fig. 5B) at the first resonance peak due to resonant tunneling

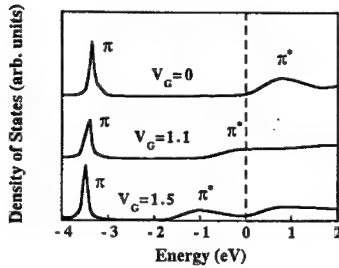


Figure 8: Difference between the density of states of the two semi-infinite electrodes with and without the benzene-1,4-dithiolate molecule in between, for three different gate voltages. The left Fermi level has been chosen as the zero of energy.

with antibonding states. The charge is again recovered in the central C bonds when the resonant tunneling condition is lost and the molecule contracts back to nearly its original bond-length distances. This “breathing” effect is not observed at the second peak bias, because resonant tunneling in that case is mainly due to bonding π orbitals. Further details on current-induced forces will be given elsewhere.

CONCLUSION

The above calculations show that the absolute magnitude of the current is an extremely sensitive function of the contact geometry and chemistry. For the case at hand, the discrepancy with experiment is still about an order of magnitude. There are of course additional effects that can alter the value of the current, such as temperature (hot electrons and vibrational coupling) or local disorder in the Au metal near the contacts that can produce electron localization. [18] The latter effect may arise from the breaking of the gold wire when contacts to the molecule are made. [1] We further note that the experimental measurements have an uncertainty of at least a factor two. [1] Additional theoretical and experimental work is clearly needed to clarify these issues further. Finally, our results shed new light on the transport properties of molecular devices and show that such calculations would be useful in designing devices and engineering contacts for future nanotechnology.

Acknowledgment: This work was supported in part by the DARPA/ONR Grant N00014-99-1-0351, the National Science Foundation Grant DMR-98-03768, and by the William A. and Nancy F. McMinn Endowment at Vanderbilt University.

REFERENCES

1. M.A. Reed, C. Zhou, C.J. Muller, T.P. Burgin, J.M. Tour, *Science* **278**, 252 (1997).
2. D.L. Klein, P.L. McEuen, J.E. Bowen Katari, R. Roth, and A.P. Alivisatos, *Appl. Phys. Lett.* **68**, 2574 (1996).
3. J.W.G. Wildoer, L.C. Venema, A.G. Rinzler, R.E. Smalley, C. Dekker, *Nature* **391**, 59 (1998); S.J. Tans, A.R.M. Verschueren, C. Dekker, *Nature* **393**, 49 (1998); S.J. Tans,

M.H. Devoret, H.J. Dai, A. Thess, R.E. Smalley, L.J. Geerligs, C. Dekker, *Nature* **386**, 474 (1997).

4. R. Martel, T. Schmidt, H.R. Shea, T. Hertel, Ph. Avouris, *Appl. Phys. Lett.* **73**, 2447 (1998).
5. M.V. Fischetti, *Phys. Rev. Lett.* **53**, 1755 (1984); M.V. Fischetti and E. Laux, *Phys. Rev. B* **38**, 9721 (1988).
6. P. Delaney and M. Di Ventra, *Appl. Phys. Lett.* (in press); P. Delaney, M. Di Ventra, and S.T. Pantelides, *Appl. Phys. Lett.* (in press).
7. W.B. Davis, W.A. Svec, M.A. Ratner, and M.R. Wasielewski, *Nature* **396**, 60 (1998).
8. M.P. Samanta, W. Tian, S. Datta, J.I. Henderson, and C.P. Kubiak, *Phys. Rev. B* **53**, R7626 (1996); S. Datta, D.B. Janes, R.P. Andres, C.P. Kubiak, and R.G. Reifenberger, *Semicond. Sci. Technol.* **13**, 1347 (1998).
9. J.K. Gimzewski and C. Joachim, *Science* **283**, 1683 (1999).
10. M. Di Ventra, S.T. Pantelides, and N.D. Lang, *Phys. Rev. Lett.* (in press).
11. See, e.g., N.D. Lang, in *Solid State Physics*, edited by F. Seitz, D. Turnbull, and H. Ehrenreich (Academic, NY, 1973), Vol. 28, p. 225.
12. W. Kohn and L. J. Sham, *Phys. Rev.* **140**, A1133 (1965); D. M. Ceperley and B. J. Alder, *Phys. Rev. Lett.* **45**, 566 (1980).
13. N.D. Lang, *Phys. Rev. B* **52**, 5335 (1995); *ibid.* **49**, 2067 (1994); N.D. Lang and Ph. Avouris, *Phys. Rev. Lett.*, **81**, 3515 (1998).
14. M. Di Ventra and S.T. Pantelides, *Phys. Rev. B* (submitted).
15. P.E. Laibinis, G.M. Whitesides, D.L. Allara, Y.T. Tao, A.N. Parikh, and R.G. Nuzzo, *J. Am. Chem. Soc.* **113**, 7152 (1991).
16. See, e.g., J.P. Perdew, K. Burke, and M. Ernzerhof, *Phys. Rev. Lett.* **77**, 3865 (1996).
17. M. Sassoli de Bianchi and M. Di Ventra, *J. Math. Phys.* **36**, 1753 (1995).
18. P.W. Anderson, D.J. Thouless, E. Abrahams, and D.S. Fisher, *Phys. Rev. B* **22**, 3519 (1980).

ELECTRONIC STRUCTURE OF ORGANIC/METAL INTERFACES STUDIED BY UPS AND KELVIN PROBE

Kazuhiko Seki^{1,2}, Hiroshi Oji², Eisuke Ito³, Daisuke Yoshimura²,
Naoki Hayashi², Yukio Ouchi², and Hisao Ishii²

¹Research Center for Materials Science and Dept of Chemistry, Nagoya, JAPAN;

²Department of Chemistry, Graduate School of Science, Nagoya University, Furo-cho, Chikusa-ku, Nagoya 464-8602, JAPAN.

³Venture Business Laboratory, Nagoya University, Furo-cho, Chikusa-ku, 464-8603, Japan

ABSTRACT

The interfaces of organic materials with other solids play important roles in the function of various organic devices such as organic light-emitting diodes (OLEDs), spectral sensitization in photography, organic solar cells, and electrophotography. Also they should be important in future molecular devices, both in the central part of the device and at the connection with outside circuits. However, serious experimental examination of such interfaces has started only recently. In this talk we focus our attention on the organic/metal interfaces, and summarize our understanding about (1) the energy level alignment right at the interface, and (2) possible band bending within an organic layer, mainly using the techniques of UV photoemission spectroscopy (UPS) and Kelvin probe method. As for (1), the formation of electric dipole layer was observed in most organic/metal interfaces, and its origin is discussed. As for (2), recent examination of the existence/absence of band bending in ultrahigh vacuum will be reported. It is also pointed out that there can be much effects of (i) atmosphere at sample preparation and measurements, and (2) chemistry and interdiffusion at the interface.

INTRODUCTION

Recently there has been much interest in the electronic devices using electronically functional organic materials. Organic photoconductors are already used in the real application of electrophotography, and active studies are currently carried out worldwide in the field of organic electroluminescent devices (OLEDs). Such investigations are also aimed at devices at molecular level, as extensively discussed in this session.

In many of these devices, the function originates in the interface formed by the organic material with other solids, such as metal electrode or another organic material. Thus the elucidation of the interfacial electronic structure is very important for understanding and improving the function. However, serious experimental examination of the electronic structures has started just recently.

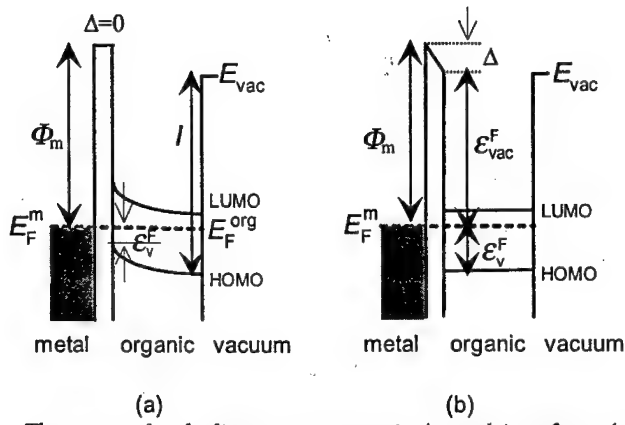


Figure 1. The energy level alignment at organic / metal interface. (a) Mott-Schottky model. (b) observed energy diagram by UPS.

The interfacial electronic structure has been often estimated by lining up the separately observed electronic structures of an organic material and an electrode metal, with the assumption of a common vacuum level at the interface, according to Mott-Schottky (MS) model [1] as shown in Fig.1(a). In this model, the vacuum level of an organic semiconductor coincides to that of a metal electrode at their interface, while the energy positions of electronic levels of the organic semiconductor changes with the distance from the interface to achieve the Fermi level alignment between the organic semiconductor and the electrode metal. This spatial change of the energy levels is called band bending. By using this model, for example, the barrier height for hole injection (ϵ_v^F) has been often estimated as the difference between the work function of the electrode (Φ_m) and threshold ionization potential (I) of the organic material in solid phase.

Recently, we have performed experimental examination of the assumption of a common vacuum level by using ultraviolet photoemission spectroscopy (UPS) for various type of organic materials such as dye molecules [2-6,9], organic EL materials [6-9], strong donors and acceptors [6,9], and organic insulator[10-12]. Our results have clearly indicated that the vacuum level alignment in MS model is not valid for the interfaces between metal and various organic materials. At these interfaces, the vacuum levels of an organic material and a metal do not align at the interface, as shown in Fig.1(b), indicating the formation of an electric dipole layer at the interface. Here we define the potential difference between outermost metal surface and 1st organic layer as Δ , which corresponds to the error of the MS model. The investigation of the general tendency of the direction and magnitude of Δ is useful not only for a practical estimation of barrier height but also for the control of the device performance.

Besides energy level alignment right at organic/metal interface, band bending expected from MS model should be also examined for organic/metal interfaces. The gradient of electrostatic potential at space charge layer near organic/metal interface plays an important role in charge separation process in organic photovoltaic cells. Fermi level

alignment in MS model, which is driving force to band bending, is actually valid for conducting materials such as metals and inorganic-semiconductors. However, the validity is not well understood in the case of organic materials, which are basically wide gap insulators.

In this talk, we present our recent effort for clarifying the interfacial electronic structures at organic/metal systems. The concepts of “common vacuum level” and “band bending” were examined by UV photoemission and Kelvin probe method for organic thin films on metal electrodes. We propose the possible origins of the formation of the interfacial dipole and the general trends of the potential shift against the work function of the electrode metal. The results of band bending and Fermi level alignment at TPD/metal interface in ultrahigh vacuum are also presented. Although the measurements were carried out for thin films of macroscopic size, we hope that the results by well established methods will serve as a guide for more microscopic methods, and give useful insight into more microscopic interfaces, e.g. between an SPM tip and a molecule attached to it.

RESULTS and DISCUSSION

(I) UPS study for the examination of *common vacuum level* at organic/metal interfaces

(i) An example of UPS study for energy level alignment at organic/metal interface

Figure 2(a) shows UPS spectra of TPD film on Au substrate as a function of film thickness from 0.05 to 10 nm. The bottom spectrum is for the clean Au substrate. The abscissa is the electron binding energy relative to the Fermi level of Au substrate. The detailed assignment was described elsewhere including the experimental details[9]. The cut-off at the lower binding energy side (left-side) indicated by a dotted line corresponds to the vacuum level of the film and its position clearly depends on the film thickness. Figure 2(b) shows the thickness dependence of the energy of the vacuum level (ϵ_{vac}^F) of the TPD film derived from the cut-off, together with the onset energy of TPD (ϵ_v^F) determined from the high energy onset (right-side) of the spectra. Initial deposition of TPD induced abrupt decrease of ϵ_{vac}^F in the thickness range up to around 0.5nm. The vacuum level was shifted slightly downwards by the further deposition up to 2nm thickness, and then became almost constant in the larger thickness region. This variation of the vacuum level energy clearly indicates that the assumption of a common vacuum level is not valid for this interface. This shift of the vacuum level of -0.5 eV implies the formation of an electric double layer at the interface. The initial steep decrease of ϵ_{vac}^F suggests that the potential drop across the interface is confined to the interfacial region.

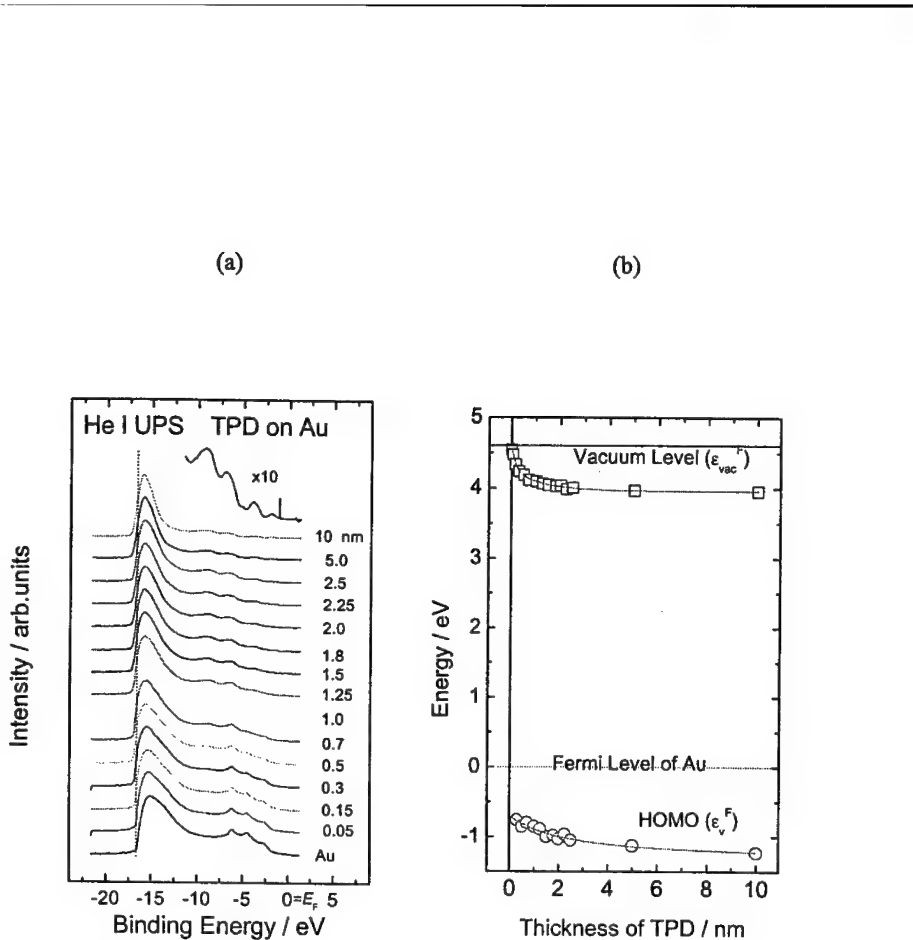


Figure 2. (a) UPS spectra of TPD on Au substrate as a function of the thickness of TPD. (b) The plot of the energy position of the vacuum level and highest occupied molecular orbital (HOMO) of TPD.

(ii) Trend of the observed vacuum level shift

By performing similar experiments, we have so far investigated the energy level alignment at various organic/metal interfaces. The observed vacuum level shifts Δ are plotted as functions of the work function of metal electrode (Φ_m) in Figure 3. The data points for three porphyrins (ZnTPP, H₂TPP, H₂T(4-Py)P), organic EL materials (Alq₃, TPD, and DP-NTCI), strong donor and acceptor (TTN, TCNQ), and organic insulator (long chain alkane, TTC) are plotted. Substrate metals are denoted around each data point. (As to the full name and the chemical structures, please see ref[9]).

As seen in the plot, there is no exact analytical relation between Δ and Φ_m which can explain the total behavior of all data points. However, phenomenologically we can find the trends of Δ . We can point out two tendencies. First, the polarity of Δ is negative except for strong acceptor / metal interface such as DP-NTCI/Al and TCNQ/Au interfaces. This trend suggests that the MS model tends to underestimate (overestimate) the barrier height for hole (electron) injection at organic /metal interfaces. It should be noted that the error often reaches 1.0 eV which is comparable to the band gap of typical organic semiconductor. Thus, the traditional MS model often predicts wrong interfacial properties such as carrier injecting nature. Second, the magnitude of Δ seems to be

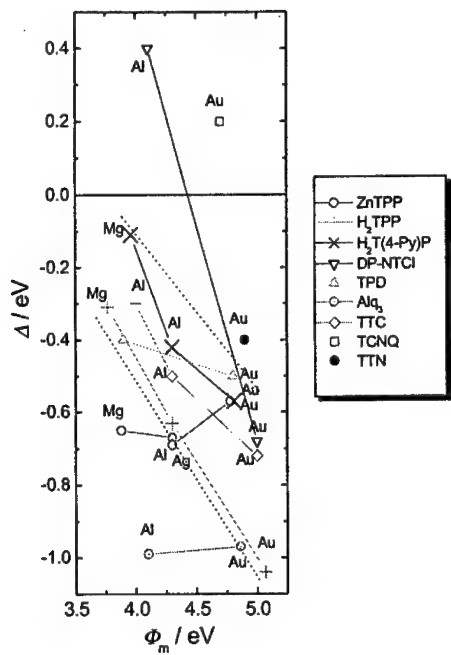


Figure 3. Plots of the observed vacuum level shift Δ against the work function of metal substrate Φ_m

Table 1. Interface parameters S at various organic / metal interfaces

ORGANIC MATERIALS	SUBSTRATE METAL	INTERFACE PARAMETER, S	REF.
ZnTPP	Mg, Al, Ag, Au	1.0	2, 4-6
Alq ₃	Mg, Ag, Au	0.9	13
	Mg, Al, Au	~1	14
TTC (n-C ₄₄ H ₉₀)	Pb, Ag, Au	0.6	10
	Cu(100), Au(111)	0.5	11
CBP	Mg, Ag, Au	0.6	13
α-NPD	Mg, Au	0.49	13
H ₂ TPP	Mg, Al, Au	0.5	4-6
H ₂ T(4-Py)P	Mg, Al, Au	0.4	4-6
DP-NTCI	Al, Au	~0.5	7
C ₆₀	Mg, Bi, Cr, Ag, Au	~0	15
PTCDA	Mg, In, Sn, Au	0	13

monotonic function of Φ_m ; that is, most data points seem to be almost linear function of Φ_m .

Similar linearity has been well known at inorganic semiconductor/metal interfaces: the barrier height ϵ_v^F is proportional to Φ_m and the absolute value of the slope of the linear function is defined as *interface parameter S*[1]. Because ϵ_v^F is equal to $I\cdot\Phi_m - \Delta$, the slope in Fig.3 corresponds to $S-1$. In table 1, the interface parameters obtained from UPS measurements were summarized together with that reported by other groups. The value of S varies from zero to unity depending on the materials.

(iii) Possible origins of the interface dipole

The clarification of the origin of the vacuum level shift is indispensable for understanding the energy level alignment at the interfaces. Though we have no definite model to explain the whole behavior of Δ at the present stage, the observed trends enable us to suggest possible origins of Δ . Here we can point out several factors to be considered as follows.

(a) Charge transfer

As shown in Fig.2, strong acceptors such as TCNQ and DP-NTCI showed positive shift of the vacuum level. This implies that the interface dipole with the organic side negatively charged is formed. This can be explained that electron is transferred from metal to acceptor molecules. Such charge transfer behavior has been reported at some interfaces such as C_{60} /metal[16], and Alq_3/Ca [17], where the appearance of extra peak in UPS due to the occupation of lowest unoccupied molecular orbital (LUMO) of the molecules by electron transfer has been experimentally observed.

(b) Formation of chemical bond

Chemical bond formation at the interface can also lead the formation of interface dipole. In the case of adsorption of small molecules such as CO, ethylene, and benzene to metal surfaces, parts of their molecular orbitals mix with the wave function of metal surface, leading chemical bond at the interface[18]. Such interaction which is accompanied with charge redistribution at the interface can contribute to the formation of interface dipole with the work function change of the surface. At the interface between metal and organic semiconductor with π system, such type of interaction can be expected. The behavior of Alq_3 and $ZnTPP$ interface may be due to this kind of chemical effect.

(c) Interface state

Another origin is the possible existence of interface state. As mentioned in the previous section, for inorganic/metal interface, Schottky barrier height is known to be proportional to the metal work function Φ_m with a slope parameter, S , is dependent on the compound. Such behavior has been explained by surface or interface states: the population of such mid-gap states will change when the relative position of the Fermi level of metal electrode to the gap is changed by the variation of Φ_m . Such change of the population can induce the change of the interfacial dipole.

(d) Vacuum level shift at physisorption system: image effect or push back effect

TTC ($n-C_{44}H_{90}$) is an organic insulator with a wide HOMO-LUMO gap of about 9 eV. Because of such a wide gap, at TTC/metal interfaces, the frontier orbitals of TTC are well separated from the Fermi level of the metal substrate. Thus, either charge transfer or

chemical bond formation can not be expected at this interface. In spite of weak interaction at the interface, the vacuum level shift of -0.7eV was observed at TTC/Au interface[10]. This fact implies that we have to consider another origin of interface dipole which is operative even in the case of physisorption. At this present, we have two models for this effect.

First is the image-effect. Since molecular semiconductors form molecular solids with van der Waals interaction, it is suggestive to refer the rare gas/metal system. Xe atoms are absorbed physically on various metal. In spite of such a weakly interacting system, the absorption of Xe atoms leads finite change of the work function of the surface. That is, chemically inert Xe atoms induce the electric double layer at the surface. This work function change is ascribed to the interaction of the valence electrons of Xe with its image in the metal [19, 20]. Such decrease of the work function can be explained that an electron closer to the substrate is attracted more strongly by its image than an electron far away from the substrate.

There is an alternative explanation about the case of Xe adsorption that the change of the work function is not due to the image effect, but due to the rearrangement of the electron cloud at the metal surface. The tailing part of the electronic cloud into vacuum is pushed back by repulsion with the electron cloud in the adsorbate molecules, resulting in an effectively positive charging of the vacuum side by adsorption compared with the bare surface.

Both the two models lead the formation of interface dipole with organic side positively charged. It should be also applicable to other organic/metal interfaces, and explains the general trend of negative vacuum level shift.

(II) Examination of band bending and Fermi level alignment at TPD/metal interfaces

In Fig.4, the vacuum level energy of TPD film on various metal substrates (Au, Cu, Ag, Mg, Ca) were plotted as a function of Φ_m of the substrates and the thickness of the TPD film. The measurement was performed with Kelvin probe method (KPM) instead of UPS. In the case of UPS, it is often difficult to distinguish the spectral shift by band bending from artificial shift due to sample charging and/or photovoltaic effect during the measurement. KPM is more suitable for the measurement for thicker film because it is free from charge-up and photovoltaic effect.

At all the interfaces in Fig.4, an abrupt shift of the vacuum level was observed within 1nm thickness, while further deposition of TPD up to 100nm led to no change of the location of the vacuum level. According to MS model, the energy levels of semiconductor show gradual shift with the increase of the thickness, and finally Fermi level alignment between the semiconductor and the metal is achieved, where the energy position of the levels of the semiconductor relative to the Fermi level of the metal becomes irrespective of the work function of the substrate metal. The observed flat behavior of the vacuum level indicates that band bending does not occur or is very small within 100nm thickness in ultrahigh vacuum (UHV) condition. These results are probably due to the low concentration of the impurity in TPD film in UHV.

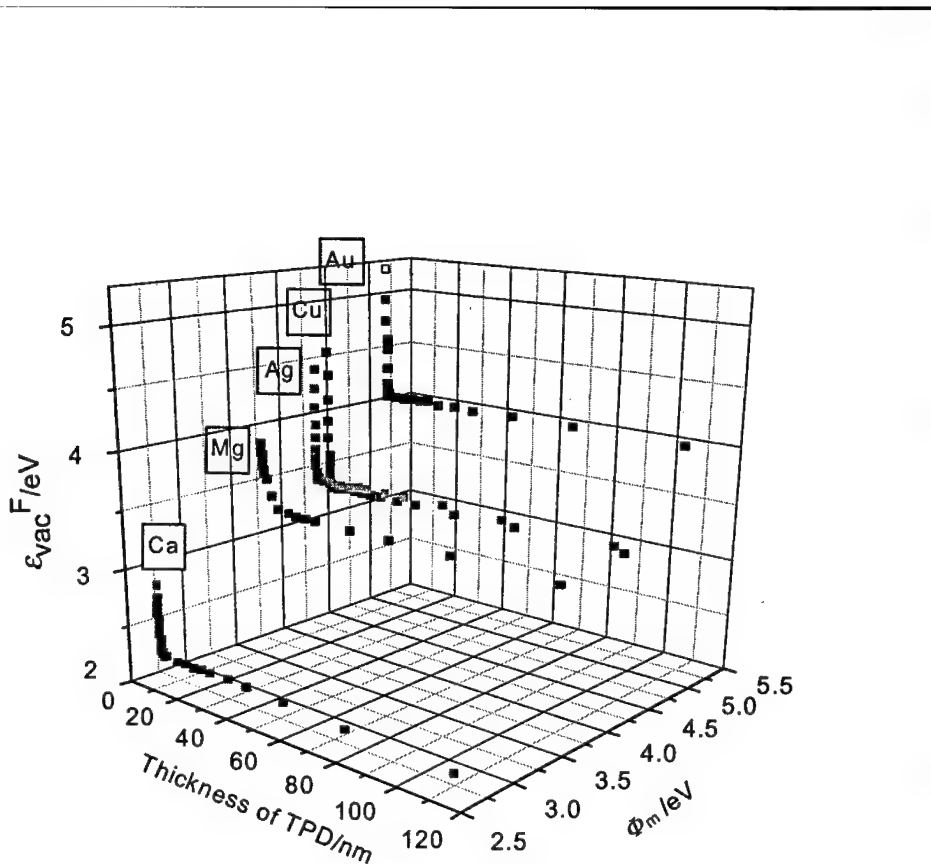


Figure 4. The energy of the vacuum level of TPD film on various metal substrates (Au, Cu, Ag, Mg, Ca) as a function of Φ_m and thickness of TPD. Energy reference is the Fermi level of the substrate metal.

Recently, Pfeiffer et al.[21], proposed the Fermi level alignment between zinc phthalocyanine (ZnPC) and metal electrode (Au and Ag) in high vacuum condition. Since they used only two substrates, the Fermi level alignment was not clearly proved. Experimental criteria of Fermi level alignment is that the energy position of thick organic film against the Fermi level of the substrate is constant irrespective of the work function of the metal substrate. Thus, constant energy of the vacuum level of the organic film should be confirmed for more than two metals.

In the case of atmospheric condition, Moons et al.[22] reported the change of the vacuum level position with increasing film thickness like band bending. Iwamoto et al.[23] observed constant surface potential of LB films on various metal substrate in atmosphere, suggesting Fermi level alignment.

The discrepancy among these works is dependent on the difference of the atmosphere, sample, and its purity for the experiments. The study in UHV condition is one of the practical and important ways for total understanding of band bending and Fermi level alignment.

(III) Effect of atmosphere and deposition sequence

As mentioned above, atmosphere can affect band bending behavior. The increase of the concentration of dopant such as oxygen in atmosphere may lead band bending and Fermi level alignment. The effect of atmosphere should be taken into account to discuss the real device. For example, the oxidation of electrode surface by oxygen in atmosphere can induce the change of the work function of the electrode and modify the interfacial electronic structure. Actually, the change of the energy level alignment was observed at porphyrin/metal interfaces. Figure 5 shows UPS spectra of zinc-tetraphenylporphyrin(ZnTPP) film on Au, Ag, Al, and Mg substrates before and after exposure to oxygen of 4Torr for 5 min [2,5]. The solid and dotted vertical lines indicate the onset of HOMO peaks measured before and after exposure to oxygen, respectively. As denoted by an arrow, the energy position was changed by oxygen exposure and the amount and the direction of the shift is strongly dependent on metals. This result indicates that the control of atmosphere is crucial for the fundamental studies of interfaces and the performance of real devices.

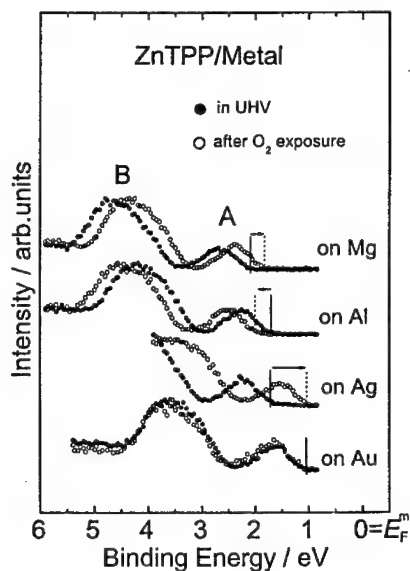


Figure 5 .UPS spectra in the uppermost valence region for ZnTPP films evaporated on various metals (Mg, Al, Ag, Au) in ultrahigh vacuum (filled circles) and after exposure to oxygen (open circles).

In this paper, we have reported the results for the interfaces where an organic thin film was formed on a metal substrate (organic on metal system). This system is suited for the investigation of energy level alignment. On the other hand, the reverse interface where a metal electrode is fabricated on an organic film (metal on organic system) is also important in real devices. In the latter case, chemical reaction and metal diffusion can

readily occur at many interfaces, and actually such phenomena were reported for several interfaces like Alq₃/Mg[24], sexiphenyl / metal [25] systems.

CONCLUSION

The energy level alignment at organic/metal interfaces was examined by using UPS and Kelvin probe method. We found that the vacuum level alignment is not achieved at the interfaces. There exists a potential change across the interfaces, which cannot be neglected at most organic interfaces. The general trends and possible origins of the vacuum level shift were discussed. Such discussion is useful to estimate and control the barrier height at real device interfaces. The concepts of band bending and Fermi level alignment in MS-model were also examined. At TPD/metal interfaces fabricated in UHV, no band bending feature was observed within 100nm thickness region. In order to understand the possible band bending, the experimental data for clean organic film and that with well defined dopant should be accumulated. It is also pointed out that there can be much effects of (1) atmosphere at sample preparation and measurements, and (2) chemistry and interdiffusion at the interface.

In this paper, we discussed the energy level alignment between an organic film and a metal electrode. The formation of interfacial dipole is basically due to the microscopic interaction between a metal surface and first organic layer contacted directly to the metal surface. Thus, we believe that the understanding for macroscopic organic interface will serve as a guide for more microscopic methods, and give useful insight into more microscopic interfaces, e.g. between an SPM tip and a molecule attached to it.

ACKNOWLEDGEMENT

This work was supported in part by Grant-in Aids for Scientific Research from the Ministry of Education, Science, Sports, and Culture of Japan (Nos. 10146101, 10440205, and 07CE2004), and by the Venture Business Laboratory Program "Advanced Nanoprocess Technology" of Nagoya University.

REFERENCES

- [1] R. Mönch, *Surf. Sci.*, 299/300 (1994) 928 and references therein.
- [2] S. Narioka, H. Ishii, D. Yoshimura, M. Sei, Y. Ouchi, K. Seki, S. Hasegawa, T. Miyazaki, Y. Harima, and K. Yamashita, *Appl. Phys. Lett.*, 67 (1995) 1899.
- [3] K. Seki, T. Tani, and H. Ishii, *Thin Solid Films*, 273 (1996) 20.
- [4] D. Yoshimura, H. Ishii, S. Narioka, M. Sei, T. Miyazaki, Y. Ouchi, S. Hasegawa, Y. Harima, K. Yamashita, and K. Seki, *Synth. Met.*, 86 (1997) 2399.
- [5] H. Ishii, S. Hasegawa, D. Yoshimura, K. Sugiyama, S. Narioka, M. Sei, Y. Ouchi, K. Seki, Y. Harima, and K. Yamashita, *Mol. Cryst. Liq. Cryst.*, 296 (1997) 427.
- [6] H. Ishii and K. Seki, *IEEE Trans. Electron Dev.*, 44 (1997) 1295.

[7] K. Sugiyama, D. Yoshimura, E. Ito, T. Miyazaki, Y. Hamatani, I. Kawamoto, H. Ishii, Y. Ouchi, and K. Seki, *Synth. Met.*, 86 (1997) 2425.

[8] H. Ishii, D. Yoshimura, K. Sugiyama, S. Narioka, Y. Hamatani, I. Kawamoto, T. Miyazaki, Y. Ouchi, and K. Seki, *Synth. Met.*, 85 (1997) 1389.

[9] H. Ishii, K. Sugiyama, D. Yoshimura, E. Ito, Y. Ouchi, and K. Seki, *IEEE J. Sel. Top. Quant. Electron.*, 4 (1998) 24.

[10] E. Ito, H. Oji, H. Ishii, K. Oichi, Y. Ouchi, and K. Seki, *Chem. Phys. Lett.*, 287 (1998) 137.

[11] H. Ishii, E. Morikawa, S. J. Tang, D. Yoshimura, E. Ito, K. Okudaira, T. Miyamae, S. Hasegawa, P. T. Sprunger, N. Ueno, K. Seki and V. Saile, *J. Electron Spectrosc. Relat. Phenom.*, 101-103 (1999) 559.

[12] H. Ishii, K. Sugiyama, E. Ito, and K. Seki, *Advanced Materials*, 11 (1999) 605.

[13] I. G. Hill, A. Rajagopal, A. Kahn, and Y. Hu, *Appl. Phys. Lett.*, 73 (1998) 662.

[14] unpublished data

[15] T. R. Ohno, Y. Chen, S. E. Harvey, G. H. Kroll, J. H. Weaver, R. E. Haufler and R. E. Smalley, *Phys. Rev.*, B44 (1991) 13747.

[16] E. Magnano, S. Vandre, C. Cepek, A. Goldoni, A. D. Laine, G. M. Curro, A. Santaniello, M. Sancrotti, *Surf. Sci.*, 377-379 (1997) 1066.

[17] V.-E. Choong, M. G. Mason, C. W. Tang, and Y. Gao, *Appl. Phys. Lett.*, 72 (1998) 2689.

[18] H.J.Freund and H.Kuhlenbeck, in *Application of synchrotron radiation* (ed. W. Eberhardt), Springer-Verlag Berlin Heidelberg (1995) 9 and references therein.

[19] A. Zangwill, *Physics at surfaces*, Cambridge University Press, Cambridge, pp.185, 1988, and references therein.

[20] K. Wandelt and J. E. Hulse, *J. Chem. Phys.*, 80 (1984) 1340.

[21] M. Pfeiffer, K. Leo and N. Karl, *J. Appl. Phys.*, 80 (1996) 6880.

[22] E. Moons, A. Goossens, T. Savenije, *J. Phys. Chem., B* 101 (1997) 8492.

[23] M. Iwamoto, A. Fukuda, and E. Itoh, *J. Appl. Phys.*, 75 (1994) 1607.

[24] R. Rajagopal and A. Kahn, *Appl. Phys. Lett.*, 84 (1998) 355.

[25] H. Oji, E. Ito, M. Furuta, K. Kajikawa, H. Ishii, Y. Ouchi, and K. Seki, *J. Electron Spectrosc. Relat. Phenom.*, 101-103 (1999) 517.

Molecular Scale Electronics

A. M. Rawlett, E. T. Mickelson, W. A. Reinerth, L. Jones II, M. Kozaki, T. P. Burgin, and J. M. Tour*

Department of Chemistry and Center for Nanoscale Science and Technology, MS 222, Rice University, Houston, TX 77005, USA

E-mail: tour@rice.edu

J. Chen, C.-W. Zhou, C. J. Muller, M. R. Deshpande, and M. A. Reed*

Department of Electrical Engineering, Yale University, New Haven, CT 06520, USA

E-mail: mark.reed@yale.edu

L. A. Bumm, M. T. Cygan, T. D. Dunbar, P. S. Weiss*, and D. L. Allara*

Department of Chemistry, Pennsylvania State University, University Park, PA 16802, USA

E-mail: stm@psu.edu (Weiss), dla3@psu.edu (Allara)

ABSTRACT

This paper reports on some of the recent advances in the development and testing of molecular-scale electronic devices, devices that may ultimately be the basis of a molecular-based computer. These advances include: the synthesis of molecules which will perform specific electronic functions, self-assembled monolayer formation of rigid-rod conjugated oligomers, novel methodologies for the design and testing of molecular electronic devices, and the observance of negative differential resistance (NDR) through a molecule.

INTRODUCTION

It is increasingly likely that the computers of tomorrow will consist of devices that are ultra dense, ultra fast, and molecular-sized [1-8]. As we rapidly approach the point at which solid state electronic devices reach the limit of their miniaturization [9], molecular-based systems may afford the most attractive route towards allowing us to continue to scale down the size of computers. Miniaturization, however, is not the only benefit which might be realized by the adoption of molecular-based circuitry. Computational speed and lower fabrication costs may also be considerations for turning to a molecular-based computer system.

The computational speed of existing computer devices is often dependent upon the time it takes for an electron to travel between devices. By using molecular scale electronic interconnects, transmit times could be dramatically minimized by virtue of the shorter distances realized between devices [9]. Fabrication costs of current solid-state devices are relatively high. By switching to an alternative technology like molecular-based circuitry, we may be able to eliminate many of the factors that drive up the cost of current methods and also achieve a higher defect tolerance as a result of the much higher device density of the molecular system [10]. This later feature would further act to drive costs down.

We have strived to demonstrate that molecular electronic devices can be constructed, and that once constructed, that they can be used to fabricate molecular-based computer

circuitry. Our strategy for demonstrating these ideas has involved devising synthetically precise routes to conjugated rigid rod molecules, probing their electrical properties, and devising a method of self-assembly for these molecules which will allow for the fabrication of molecular electronic devices.

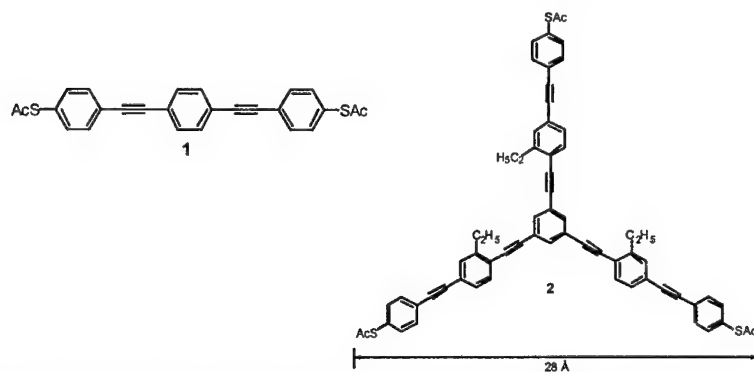
While it is well known that bulk conjugated materials can be made semiconducting or even conducting when doped [11], only recently have we discovered how thiol-ended rigid rod conjugated molecules orient themselves on gold surfaces in self-assembled monolayers (SAMs), and how we could record electronic conduction through these undoped conjugated molecules [10]. Furthermore, we have made significant advances in the synthesizing molecules to serve as molecular electronic devices. We have also demonstrated the attachment of protected thiol moieties to one or both ends of the molecular wires to serve as molecular-scale alligator clips that provide electrical contact to gold probes [12]. Using this technology, we have demonstrated negative differential resistance (NDR) behavior in a SAM of thiol-ended rigid rod conjugated molecules [13]. This result demonstrates that these molecules can be used as nanoscale electronic devices and brings the molecular computer concept much closer to being a reality.

RESULTS AND DISCUSSION

Synthesis of Molecules Which Can Serve as Molecular Scale Devices

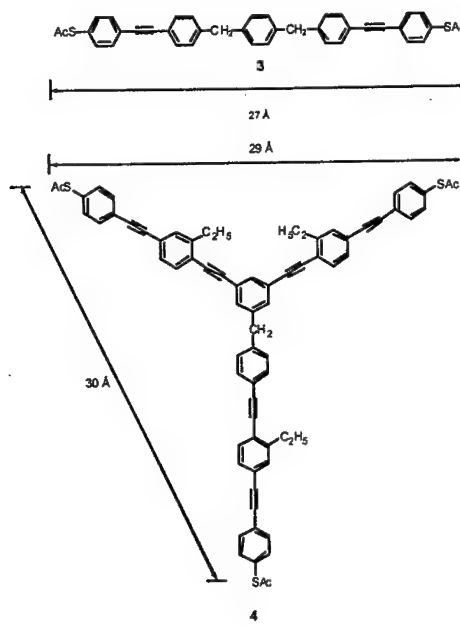
As mentioned above, discrete, highly conjugated oligo(phenylene ethynylene)s as molecular scale wires have been demonstrated to conduct an electric current. Furthermore, STM studies demonstrate that alkyl units pose significantly larger electronic transport barriers than the δ -conjugated moieties in single molecule systems [14]. With this knowledge in hand, we then began designing molecules which would, at least in theory, serve as molecular electronic devices. Molecules **1** and **2** are two examples of the kinds of δ -conjugated molecules we have synthesized. Furthermore, functional groups can be added to the rings to drastically alter their solubility and electronic properties.

We can introduce methylene and ethylene barriers into the conductive wires or devices to impart a conduction barrier as shown in molecules **3** and **4**. Such barriers may



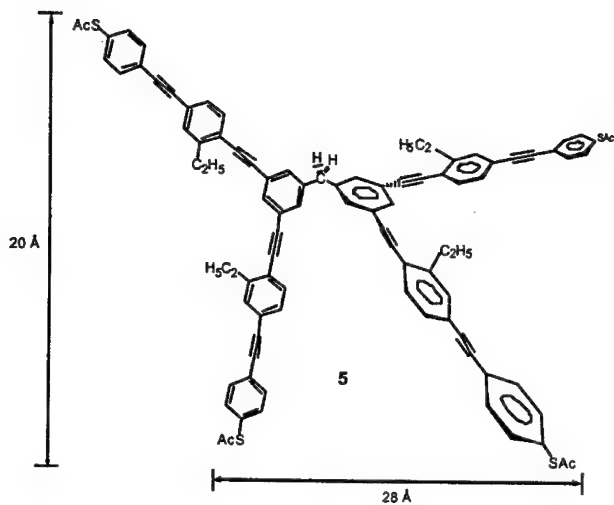
allow for the development of molecular devices which might serve as field effect transistors or resonant tunneling diodes. While three-terminal systems may possess

switch-like properties, four-terminal systems (like molecule **5**) might serve as logic gates [15].



Self-Assembled Monolayer Formation of Rigid-Rod Conjugated Oligomers

As a prelude to the utilization of molecular scale wires in molecular scale electronic devices, it is necessary to understand the molecular ordering on metal surfaces. These sulfur-terminated conjugated oligomers form SAMs on gold surfaces by attachment of the thiol end groups which serve as molecular scale alligator clips [12], this is illustrated in Figure 1. The SAMs were analyzed using ellipsometry, X-ray photoelectron spectroscopy (XPS), and infrared external reflectance spectroscopy. The thiol moieties usually dominate adsorption on the gold sites; interactions with the conjugated δ -systems are weaker. Rigid rod α,ω -dithiols form assemblies in which one thiol group binds to the surface while the second thiol moiety projects upward at the exposed surface of the SAM. *In situ* deprotection of the thiol moieties by deacetylation of the thioacetyl groups using NH₄OH permits formation of SAMs without having to isolate the oxidatively unstable free thiols. Moreover, direct adsorption, without exogenous base, of the thioacetyl-terminated oligomers can be accomplished to generate gold surface-bound thiolates. However, in the non-base-promoted adsorptions, higher concentrations of the thioacetyl groups, relative to that of thiol groups, are required to achieve monolayer coverage in



a given interval [16]. A thiol-terminated phenylene ethynylene system was shown to have a tilt angle of the long molecular axis of $<20^\circ$ from the normal to the substrate surface. These aromatic α,ω -dithiol-derived monolayers provide the basis for studies leading to the design of molecular wires capable of bridging proximal gold surfaces.

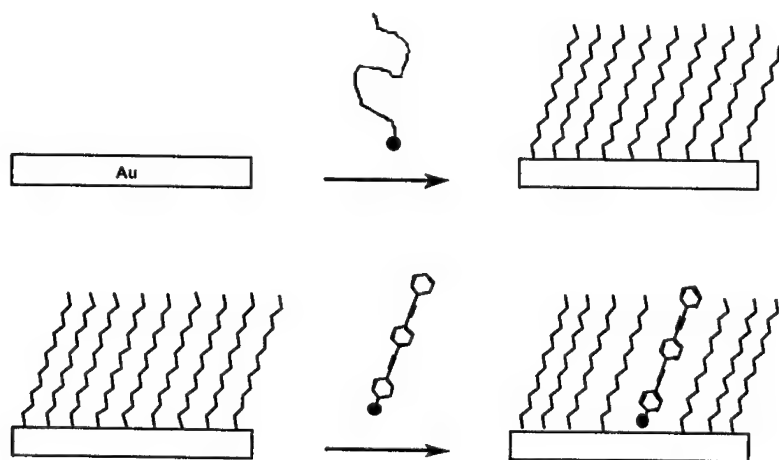


Figure 1. Schematic showing the self-assembly of a mixed monolayer of alkanethiolates and fully conjugated oligomers at an electrode via co-assembly and via sequential alkanethiolate host assembly followed by oligomer insertion. Note that the co-adsorption gives rise to domains of conjugated oligomers within the alkanethiolate host.

Conductance of a Molecular Junction

Charge transport in and the measurement of the conductance of single organic molecules is an intriguing, experimentally challenging, and long sought goal. These measurements have been performed on benzene-1,4-dithiolate connected between stable proximal metallic gold contacts using a mechanically controllable break junction (MCB) [17], as shown in Figure 2. The metal-molecule-metal configuration presents the molecular embodiment of a system analogous to a quantum dot, with the potential barriers replaced by the contact barrier of the gold-thiolate end groups. The results show a highly reproducible apparent Coulomb gap at about 0.7 V at room temperature. This study provides a direct, quantitative measurement of the molecular conductance of a junction containing a single molecule, a fundamental step in the emerging field of molecular scale electronics.

Large On-Off Ratios and Negative Differential Resistance in a Molecular Electronic Device

Electronic measurements were performed on molecules containing a nitroamine redox center (2'-amino-4-ethynylphenyl-4'-ethynylphenyl-5'-nitro-1-benzenethiol). This was carried out in a nanostructure that has a metal top contact, a SAM active region, and a metal bottom contact. The top gold contact was placed on top of the SAM via a metal evaporation process. The nanostructure used in the testing, along with the molecule being tested, is shown in Figure 3. This nanostructure is similar to that reported previously [18]. Typical I(V) characteristics for this molecule at 60 K are shown in Figure 4. Unlike previous devices that also utilized molecules to form the active region [19], this device exhibits a robust and large NDR of $< -380 \mu\text{A}\cdot\text{cm}^2$ and an on-off peak to valley ratio (PVR) in excess of 1000:1.

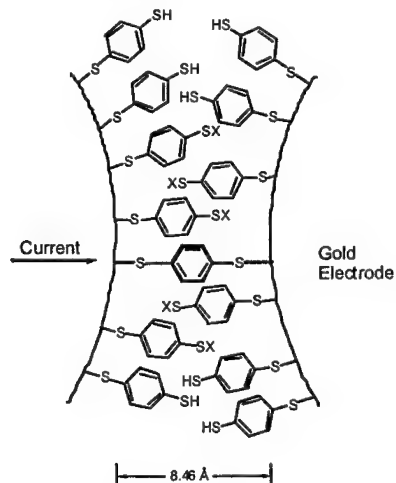


Figure 2. The desired placement of benzene-1,4-dithiolate between gold electrodes in a MCB. ($X=H, Au$).

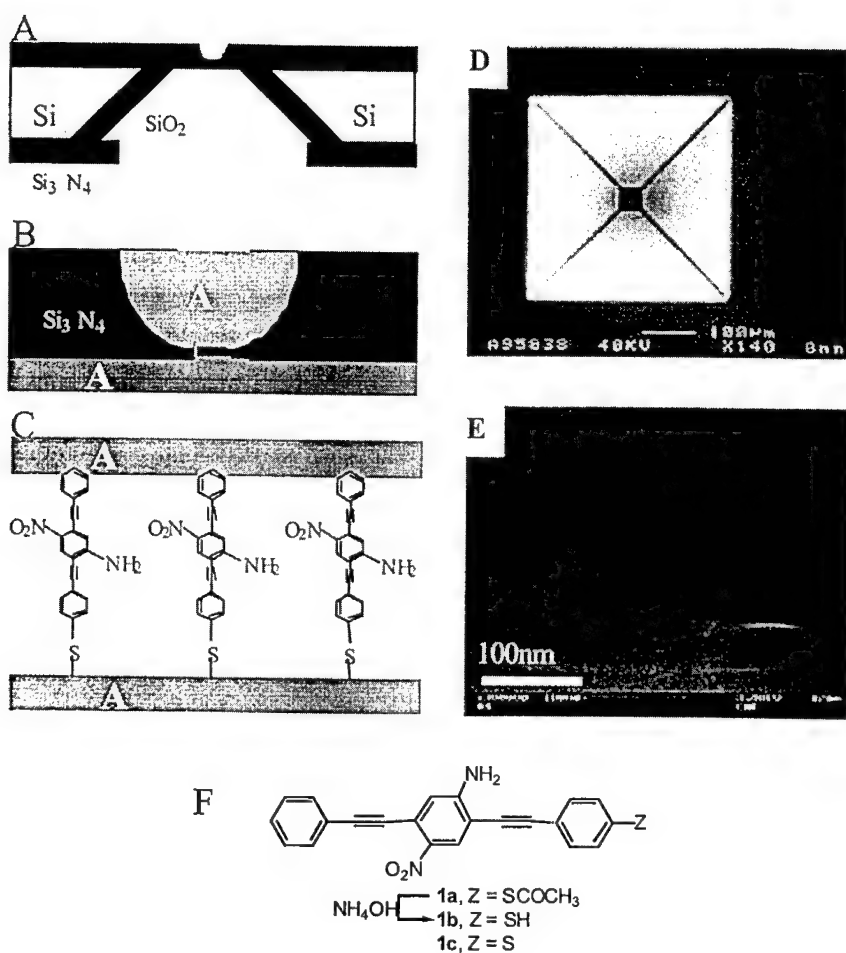


Figure 3. Schematics of device fabrication: (A) cross section of a silicon wafer with a nanopore etched through a suspended silicon nitride membrane; (B) Au-SAM-Au junction in the pore area; (C) blowup of (B) with 1c sandwiched in the junction; (D) scanning electron micrograph (SEM) of pyramid Si structure after unisotropic Si etching (that is, the bottom view of (A)); (E) SEM of an etched nanopore through the silicon nitride membrane; (F) the active molecular compound 1c, and its precursors, the free thiol 1b and the thiol-protected system 1a.

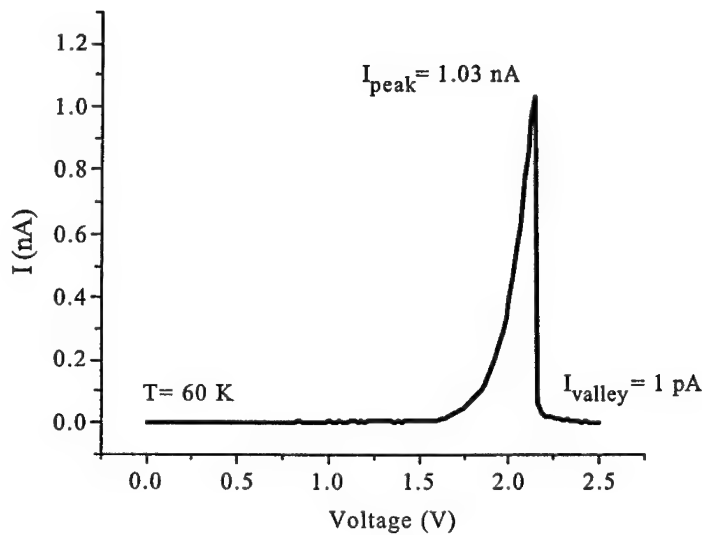


Figure 4. $I(V,T)$ characteristics of a Au-(2'-amino-4-ethynylphenyl-4'-ethynylphenyl-5'-nitro-1-benzenethiolate)-Au device.

SUMMARY

In summary, we have made significant progress towards fabricating a molecular computer. This progress has come in the synthesis of molecules suitable for inclusion in molecular-scale electronic devices, our ability to self-assemble these molecules into larger devices, and the testing of these molecular electronic devices. In our testing of these molecular electronic devices, we have demonstrated their promising role in the electronics of tomorrow. Ultimately, this technology will likely find its way into computational devices (where the need for nanoscale electronics will be the greatest) and the molecular computer will be born.

ACKNOWLEDGEMENT

Financial Support from the Defense Advanced Research Projects Agency (DARPA) via the Office of Naval Research (ONR) N00014-99-1-0406, and the Army Research Office (ARO) DAAD19-99-1-0085 is gratefully acknowledged.

REFERENCES

1. A. Aviram, Ed. *Molecular Electronics: Science and Technology*, Conference Proceedings No. 262 (American Institute of Physics, New York, 1992).
2. V. Mujica, M. Kemp, A. Roitberg, and M. Ratner, *J. Phys. Chem.* **104**, 7296 (1996).

3. A. Farazdel, M. Dupuis, E. Clementi, and A. Aviram, *J. Am. Chem. Soc.* **112**, 4206 (1990).
4. H. Dai, E.W. Wong, and C.M. Lieber, *Science* **272**, 523 (1996).
5. M.D. Ward, *Chem. Ind.*, 568 (1996).
6. S.T. Purcell, N. Garcia, V.T. Binh, L. Jones II, and J.M. Tour, *J. Am. Chem. Soc.* **116**, 11985 (1994).
7. J.I. Pascual, J. Mendez, J. Gomez-Herrero, A.M. Baro, N. Garcia, U. Landman, W.D. Luedtke, E.N. Bogachek, and H.-P. Cheng, *Science* **267**, 1793 (1995).
8. C. Joachim, and J.F. Vinuesa, *Europhys. Lett.* **33**, 1100 (1996).
9. M.C. Petty, M.R. Bryce, and D. Bloor, Eds. *Introduction to Molecular Electronics* (Oxford University Press, New York, 1995).
10. A. Aviram and M. Ratner, Eds. *Molecular Electronics: Science and Technology*, Vol. 852 (Ann. N.Y. Acad. Sci., 1998).
11. T.A. Skotheim, Ed. *Handbook of Conducting Polymers* (Marcel Dekker, New York, 1986).
12. J.M. Tour, L. Jones II, D.L. Pearson, J.S. Lamba, T.P. Burgin, G.W. Whitsides, D.L. Allara, A.N. Parikj, and S. Atre, *J. Am. Chem. Soc.* **117**, 9529 (1995).
13. J. Chen, M.A. Reed, A.M. Rawlett, and J.M. Tour, *Science* **286**, 1550 (1999).
14. L.A. Bumm, J.J. Arnold, M.T. Cygan, T.D. Dunbar, T.P. Burgin, L. Jones II, D.L. Allara, J.M. Tour, and P.S. Weiss, *Science* **271**, 1705 (1996).
15. J.M. Tour, M. Kozaki, and J.M. Seminario, *J. Am. Chem. Soc.* **120**, 8486 (1998).
16. M.T. Cygan, T.D. Dunbar, J.J. Arnold, L.A. Bumm, N.F. Shedlock, T.P. Burgin, L. Jones II, D.L. Allara, J.M. Tour, and P.S. Weiss, *J. Am. Chem. Soc.* **120**, 2721 (1999).
17. M.A. Reed, C. Zhou, C.J. Muller, T.P. Burgin, and J.M. Tour, *Science* **278**, 252 (1997).
18. C. Zhou, M.R. Deshpande, M.A. Reed, L. Jones II, and J.M. Tour, *Appl. Phys. Lett.* **71**, 611 (1997).
19. M.A. Reed, *Proc. IEEE* **87**, 652 (1999).

End-Grafted Semiconducting Polymer—Candidate for Molecular Wire

Kazuaki Furukawa, Keisuke Ebata and Michiya Fujiki
NTT Basic Research Laboratories,
3-1 Morinosato Wakamiya, Atsugi, Kanagawa 243-0198 Japan.

ABSTRACT

We report on polysilane, a synthetically accessible σ -conjugated silicon-catenated polymer with such semiconducting properties as photoconductivity, high hole drift mobility, and electroluminescence, as a candidate for molecular wire. We apply the “end-graft” technique, which we developed for fixing individual polymer chains on a substrate surface, to a semiflexible polysilane. The end-grafted semiflexible polysilane extended more than 500 nm across the Si(111) surface, and was clearly observed by means of atomic force microscopy (AFM).

INTRODUCTION

Molecular wire, a nanoscale lead, is attracting considerable attention not only as a key technology for realizing future molecular electronic devices but also for basic research designed to reveal intrinsic optoelectronic properties at the single molecule level. The prerequisites for macromolecules for molecular wire use are (1) conductivity, (2) rigidity, and (3) connectivity. In this field, the carbon nanotube is probably the most promising material at present because it has a long and rigid structure as well as high conductivity. By contrast, the advantages of synthetic polymers are the diversity of materials and the potential for connectivity precisely controlled by means of a designed chemical reaction. Here we introduce “polysilane” as a synthetic polymer that possesses the above three characteristics.

Polysilane is a polymer whose backbone consists solely of silicon atoms (figure 1). As with many other silicon-backbone materials, including crystalline silicon, polysilane has a variety of semiconducting properties arising from the delocalization of σ -electrons (σ -conjugation) [1]. For instance, it has been reported that polysilane exhibits photoconductivity [2,3], excellent hole drift mobility [4,5] and electroluminescence [6,7]. Because these semiconducting properties are always measured by using solid thin polysilane films, the observed data are dominant to the most difficult processes in the film, like the intermolecular hopping process for charge transport. The direct electronic measurement of individual polysilane single chains is thus of great interest as it will allow us to see the intrinsic properties of polysilane as well as reveal its potential for utilization as molecular wire.

This paper describes how we plan to use this polysilane as a molecular wire. The current results were obtained based on two recent pieces of original research that we undertook: the synthesis of rigid polysilane [8] and the development of the end-graft technique [9,10]. We report on the synthesis and AFM characterization of end-grafted semiflexible polysilanes.

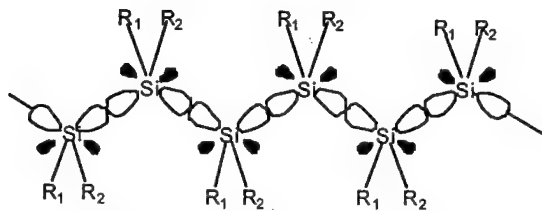


Figure 1. Molecular structure of polysilane. R_1, R_2 : organic substituents.

EXPERIMENT

A hydrogen-terminated flat Si(111) surface, that we prepared by etching an Si(111) wafer with NH_4F aqueous solution [11], was used throughout this work. This flat surface is indispensable not only for AFM observations of single molecules but also for the end-graft reaction using surface Si-H bonds.

The semiflexible polysilanes (figure 2) substituted with a branched alkyl group of (*S*)-2-methylbutyl group and a normal alkyl group (1: *n*-hexyl, 2: *n*-decyl and 3: *n*-octadecyl) were synthesized according to previously described methods [8]. Their number-average molecular weight was 1.8×10^6 , 6.3×10^6 , and 2.6×10^6 respectively (polystyrene standard). Therefore the average polymer length can be evaluated to be 1800, 4700 and 1300 nm. A dilute hexane solution of these polysilanes (ca. 5×10^{-9} mol/L) was coated on Si(111) surface for the AFM measurements.

End-grafted polysilane was synthesized by a one-to-one chemical reaction between a reactive anchor on the Si(111) surface and an end-lithiated polysilane 2 (figure 3). A hydrogen-terminated Si(111) flat surface was immersed in a (1-*r*):*r* mixture of 11-bromo-1-undecene and 1-dodecene under photoirradiation ($\lambda > 400$ nm, 16h) to form a reactive alkylbromide anchor on the Si(111) surface. The substrates were dipped into a dried and oxygen-free tetrahydrofuran solution of end-lithiated polysilanes which we prepared by the scission reaction of the Si-Si bond of polysilane 2 using lithium 4,4'-di-*tert*-butylbiphenylide. The substrates were then repeatedly washed with good polysilane solvents such as tetrahydrofuran or isoctane to remove any polysilane remaining on the surface. The end-grafted polysilane, however, was not dissolved during the washing process because it had formed a chemical bond with the surface. The molecular weight distributions of end-grafted polysilane can be evaluated from those of corresponding polysilanes obtained by quenching the lithiated polysilanes used for the end-graft reaction. The number-average molecular weight was 8.0×10^5 for end-grafted polysilane 2.

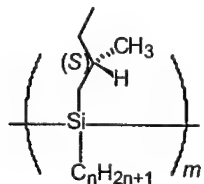


Figure 2. Chemical formulas of polysilanes used in this study. 1: $n = 6$; 2: $n = 10$; 3: $n = 18$

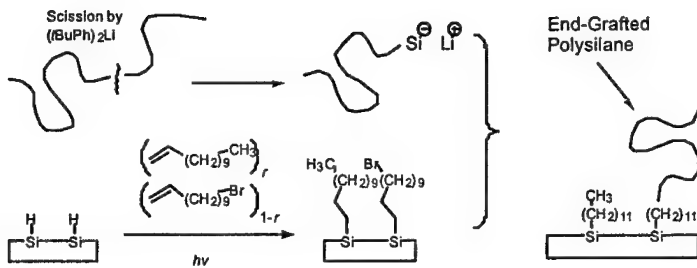


Figure 3. Schematic illustration of the synthesis of end-grafted polysilane on Si(111).

RESULTS

Semiflexible polysilane—How rigid is it?

Polysilane is unique in that the backbone rigidity is extensively controlled by the steric effects of the organic substituents. If we employ a branched alkyl group and a long normal alkyl group as substituents for each silicon atom, we can synthesize soluble semiflexible polysilanes with very high molecular weights. The persistence length, one of the scales for the rigidity of a polymer, of polysilane **1** was about 90 nm in tetrahydrofuran solution at room temperature [12]. This is longer than the value of 60 nm determined for DNA, a representative semiflexible polymer [13]. We can also evaluate the rigidity of polysilanes **2** and **3** by means of their molar absorption coefficients (ϵ) [8]. This is because the logarithmic ϵ of polysilanes is proportional to the viscosity index (α), another scale for evaluating chain rigidity. The α values of polysilanes **1**, **2**, and **3** are between 1.25 and 1.35, which is in a range of semiflexible polymers.

Figure 4 shows the tapping mode AFM topography of polysilane **3** coated on a flat Si(111) surface. Each single polysilane molecule is observed as a “macromolecular rope” with over 1000 nm long and about 1 nm high lying on the surface. The height is in good agreement with the previous observation of a single polysilane chain [14]. A similar image has been observed using polysilane **1**.

Single molecule observation is relatively easy with rigid macromolecules. Synthetic polymers, which are flexible chains in most cases, easily become entangled during the unavoidable condensation of the solution which occurs in the coating process for sample preparation. Rigid macromolecules, which include carbon nanotubes and DNA, can be placed on the substrate surface in isolation because they escape entanglement. However, we are still looking for the area of the substrate where single polysilane molecules exist in isolation as shown in figure 4. We must develop a method for picking up one or several chains in a controllable manner in order to utilize the polymer chains as a molecular wire.

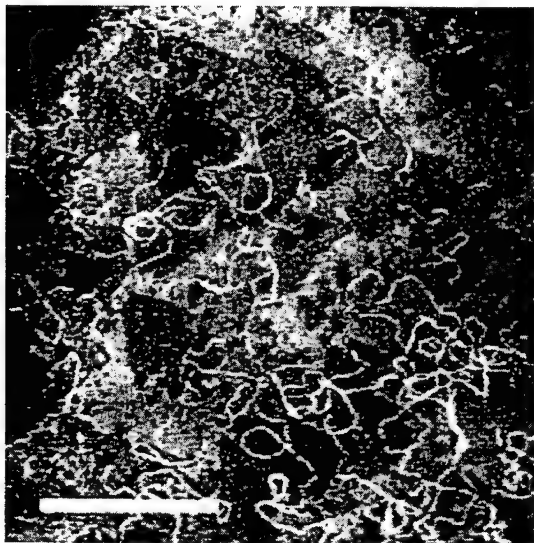


Figure 4. Tapping mode AFM topography of polysilane 3 casted on an Si(111) surface. The equilateral triangles show step patterns on the Si(111) surface. Scale bar: 500 nm.

End-graft technique—Handling of a single polymer in a controllable manner

We developed a unique “end-graft” technique designed to fix individual polysilane molecules homogeneously and extensively with a controllable density on a substrate surface. This method overcomes the above difficulty and provides substrates studded with single polysilane chains in isolation. We have reported AFM observations of the flexible polysilane poly(*n*-propyltrimethylsilane) end-grafted with a controllable density [10]. We applied the same technique to the semiflexible polysilane **2** in this study.

Figure 5 shows the tapping mode AFM topography of polysilane **2** end-grafted onto a flat Si(111) surface. The end-grafted polysilane molecules are observed again as molecular ropes. This is in marked contrast to the end-grafted flexible polysilanes which were observed as dots [10]. The end-lithiated polysilane **2** was prepared by a scission reaction with the initial polysilane high polymer, and so the resulting end-grafted polysilanes **2** were rather shorter than those observed in figure 4. However, they were still more than 500 nm in length. This means they are long enough to bridge a pair of electrodes fabricated by modern microlithographic technology, typically with a gap of less than 100 nm.

The end-grafted polysilanes **2** were well isolated from each other on the substrate

surface as shown in figure 5. We should emphasize that end-grafted polysilane chains were observed over almost the whole of the substrate area with the same density. The obtained sample is exceedingly convenient for use in the further investigation of the physical properties of the single polysilane molecule; for instance, by means of scanning probe microscopy. This is because techniques designed for detecting surface structures and physical properties simultaneously, such as scanning tunneling microscopy and scanning near-field optical microscopy, use a probe with a delicate tip which is often damaged while an area is being searched, as shown in figure 4.

There are good prospects with regard to developing molecular wiring based on the end-graft technique. The advantage of this technique is that we can end-graft a variety of polymers onto a variety of surfaces by designing reactive anchors and end-functionalized polymers. In fact, we have already acquired routes to end-grafted polysilanes on both SiO_2 [10] and SiH surfaces. This implies that we can selectively synthesize end-grafted polysilanes on either the SiO_2 surface or the SiH surface of an SiO_2/SiH patterned surface. In addition to silicon material application, we expect to employ the end-graft technique with semiconducting polymers, for instance, by using the chemical reaction between an Au surface and a terminal SH group to build reactive anchors.

Currently, it is only possible to fix one of two termini of the polysilane on the substrate surface. Although we believe this is a significant advance, the control of the other terminus is insufficient for molecular wiring. We should also design a chemical reaction to control the remaining terminus.



Figure 5. Tapping mode AFM topography of polysilane 2 end-grafted on Si(111) surface. Scale bar: 500 nm.

CONCLUSIONS

We applied an end-grafted technique to semiflexible polysilane. The AFM observations clearly characterized the isolated single polysilane molecules on the surface, with lengths extending to more than 500 nm. Polysilane is also known to be as a σ -conjugated semiconducting polymer and so is a material with the potential for molecular wire use.

ACKNOWLEDGEMENT

The authors thank Dr. Masao Morita for his encouragement throughout this work.

REFERENCES

1. N. Matsumoto, *Jpn. J. Appl. Phys.*, **37**, 5425 (1998).
2. M. Fujino, *Chem. Phys. Lett.* **136**, 451 (1987).
3. R. G. Kepler, J. M. Zeigler, L. A. Harrah and S. R. Kurtz, *Phys. Rev.*, **B35**, 2818 (1987).
4. M. Stolka, H. J. Yuh, K. McGrane and D. M. Pai, *Chem. Phys. Lett.*, **136**, 451 (1987).
5. M. A. Abkowitz, F. E. Knier, H. J. Yuh, R. J. Weagley and M. Stolka, *Solid State Commun.*, **62**, 547 (1987).
6. C.-H. Yuan, S. Hoshino, S. Toyoda, H. Suzuki, M. Fujiki and N. Matsumoto, *Appl. Phys. Lett.*, **71**, 3326 (1997).
7. H. Suzuki, S. Hoshino, C.-H. Yuan, M. Fujiki, S. Toyoda and N. Matsumoto, *IEEE J. Select. Topics Quantum Electron.*, **4**, 129 (1998).
8. M. Fujiki, *J. Am. Chem. Soc.*, **118**, 7424 (1996).
9. K. Ebata, K. Furukawa and N. Matsumoto, *J. Am. Chem. Soc.*, **120**, 7367 (1998).
10. K. Furukawa, K. Ebata and N. Matsumoto, *Appl. Phys. Lett.*, **75**, 781 (1999).
11. G. S. Higashi, Y. J. Chabal, G. W. Trucks and Krishnan Raghavachari, *Appl. Phys. Lett.*, **56**, 656 (1990).
12. Y. Jinbo, I. Terakawa, S. Sato, A. Teramoto and M. Fujiki, *Polym. Prepr. Jpn.*, **46**, 3755 (1997).
13. P. J. Hagerman, *Ann. Rev. Biophys. Biophys. Chem.*, **17**, 265 (1988).
14. K. Ebihara, S. Koshihara, M. Yoshimoto, T. Maeda, T. Ohnishi, H. Koinuma and M. Fujiki, *Jpn. J. Appl. Phys.*, **36**, L1211 (1997).

FABRICATION AND TRANSPORT PROPERTIES OF Te-DOPED Bi NANOWIRE ARRAYS

Y. M. Lin¹, X. Sun², S. B. Cronin², Z. Zhang², J. Y. Ying³, and M. S. Dresselhaus³

¹Department of Electrical Engineering and Computer Science, ²Department of Physics, and ³Department of Chemical Engineering, Massachusetts Institute of Technology, Cambridge, MA 02139

ABSTRACT

Te-doped Bi nanowires with a 40 nm wire diameter have been successfully synthesized in anodic alumina templates by the pressure injection technique. Due to the unique semimetal-semiconductor transition that occurs in Bi nanowires, these systems exhibit a rather different temperature dependence in transport properties from their bulk counterparts. An improved theoretical model of this unique 1D nanowire system is developed based on the band structure of bulk bismuth. The temperature dependence of resistance for Bi nanowire arrays have been studied experimentally for various Te dopant concentrations and the results are compared with theoretical predictions.

INTRODUCTION

Nanowires have attracted a great deal of research interest because they allow for the study of transport properties of one-dimensional (1D) quantum systems, and offer promising low-dimensional thermoelectric applications [1,2]. Since their electronic states are strongly perturbed by quantum confinement effects normal to the wire axis, 1D nanowire systems exhibit very different transport properties relative to their bulk counterparts [3,4].

Bi is a semimetal in which the T -point valence band overlaps slightly with the L -point conduction band. Due to quantum confinement effects in the nanowires, Bi undergoes a semimetal-semiconductor transition as the wire diameter decreases [4]. Theoretical modeling predicts that the semimetal-semiconductor transition occurs at a wire diameter of 50 nm for wires oriented along the (012) direction, which is a common growth direction for the nanowires.

In most applications, it is desired to be able to control the Fermi level so that the transport phenomena are dominated by a single type of carriers, i.e. electrons or holes. The study of n -type Bi nanowires is especially desirable because of the very small electron effective mass ($\approx 0.001 m_0$ [5]) and the very high anisotropy of the electron Fermi surface of Bi. The group VI element, Te, acts as an electron donor in Bi; thus Te addition increases the electron density. However, because of the band overlap in Bi, a large dopant concentration must be introduced to eliminate the effect of hole carriers; the resulting increased ionized impurity scattering can have an adverse effect on the carrier mobility.

In semiconducting Bi nanowires, because of the energy separation between the valence band and the conduction band, the carrier densities can be altered significantly without reducing the mobility very much. Therefore, the Te-doped Bi nanowire system is expected to provide a promising 1D system with highly mobile carriers by increasing the concentration of high mobility electrons and eliminating the heavier holes, especially for T below liquid nitrogen temperature, 77 K.

FABRICATION AND CHARACTERIZATION

The fabrication technique of the Te-doped Bi nanowire arrays is similar to that used in synthesizing pure Bi nanowires [6], except that pure Bi metal is replaced by the Te-doped Bi alloy in the pressure injection process. The host material for the doped Bi nanowires is a porous anodic alumina template which has self-assembled hexagonally-packed cylindrical channels. The wide bandgap of the anodic alumina provides excellent confinement of the electronic wavefunctions within the nanowires.

The porous anodic alumina was prepared by a two-step anodization method [7] to control the pore size distribution and the regularity of the pore packing order. The Al substrate with a thickness of 0.25 mm was polished mechanically and electrochemically before the anodization process. It was first anodized in 4 wt% $H_2C_2O_4$ at 45 V for 90 minutes at 19°C, and then dipped in an etch solution of H_3PO_4 and CrO_3 to dissolve the anodic alumina layer before the second anodization. The resulting Al substrate was re-anodized for 250 minutes under conditions identical to the first anodization. The SEM image of the top surface of the anodic alumina template is shown in Figure 1(a). The as-prepared anodic alumina has an average pore diameter of 40 nm with a channel length of 70 μm . It was found that the pore size and the template thickness were very reproducible for samples prepared by this two-step anodization method.

The Te-doped Bi alloy was prepared by mixing the desired amounts of high-purity Bi (99.9999%) and Te (99.999%) in a quartz tube, which was then evacuated and sealed. The mixture was melted, and maintained at 600°C for 24 hours. The as-prepared Bi-Te alloy was then placed in the high-pressure reactor along with the porous alumina template. In the pressure injection process, Cu atoms were introduced into the metal melt to facilitate the Bi alloy filling by reducing the surface tension of Bi with respect to the template [8]. After the pressure injection process, the Al substrate and barrier layer underlying the nanowire arrays were etched away by 0.2 M $HgCl_2$ and 5 wt% H_3PO_4 , respectively, so that the nanowires were exposed on both sides of the template and electrical contacts could be made. The nanowire array was annealed in vacuum for 8 hours to release the pressure within the composite system before the transport measurements [8]. Figure 1(b) shows the SEM image of the bottom surface of the anodic

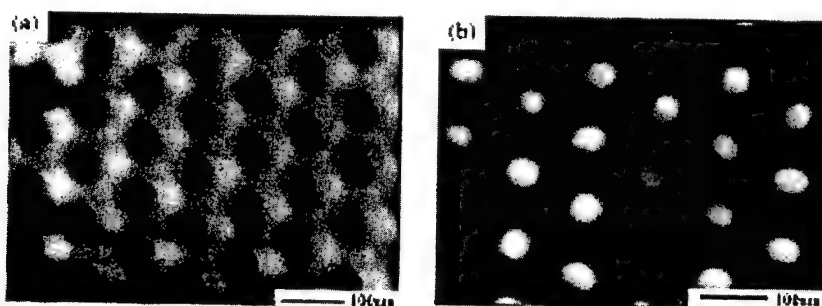


Figure 1. SEM images of (a) the top surface of the anodic alumina template after two-step anodization; and (b) the bottom surface of the anodic alumina template after pressure injection of molten Te-doped Bi. The average pore diameters of both templates are 40 nm.

alumina template after removal of the barrier layer. The bright spots indicate the channels that are filled with metal, and the dark spots represent unfilled channels. Figure 1(b) shows that most of the channels were successfully filled all the way to the bottom side of the template. X-ray diffraction pattern of the nanowire composite indicates that the crystal structure of Bi is preserved in the 40 nm nanowires, and that more than 80% of the wires are oriented along the (012) direction, or the (0,0.839,0.545) direction in Cartesian coordinates. In previous studies, it was found that pure Bi nanowires of larger wire diameters (65~105 nm) synthesized by a similar fabrication technique exhibited a preferential (202) crystal growth orientation [6,8], while the 28 nm nanowires had the same preferred orientation of (012) as our 40 nm wires. This suggests that the preferred growth direction for Bi nanowires fabricated by pressure injection may depend on the wire diameters.

THEORETICAL MODEL OF Te-DOPED Bi NANOWIRES

Bismuth has a rhombohedral crystal structure with three principal crystal axes: binary, bisectrix and trigonal, which we denote as the x , y and z axes, respectively. Bi is a semimetal in bulk form, and has three degenerate electron pockets at the L -point of the Brillouin zone and one hole pocket at the T -point, with a band overlap of 38 meV at 77 K [9]. The dispersion relation for the T -point holes can be described by a parabolic band, while the L -point electrons are strongly coupled to the L -point holes, and the dispersion relation is described by the non-parabolic Lax model [10]. If we take the edge of the conduction band at the L -point as zero, the dispersion relation of the two coupled L bands can be written as,

$$\epsilon(\vec{k}) = -\frac{\epsilon_g}{2} \pm \frac{1}{2} \sqrt{\epsilon_g^2 + 2\epsilon_g \vec{k} \cdot \vec{\alpha} \cdot \vec{k}} \quad (1)$$

where $\epsilon_g = 13.8$ meV is the direct L -point band gap at 77 K, and $\vec{\alpha}$ is the inverse effective mass tensor at the conduction band extrema. Since the carrier pockets of Bi are highly anisotropic, the electronic energy states and transport properties are strongly dependent on the crystal orientation of the nanowires. Due to the confinement of the electron wavefunctions in the plane normal to the wire axis, the energy associated with the electron motion in the cross-sectional plane will be quantized for each carrier pocket and the dispersion relation for each quantized subband will behave like a 1D system in the unconfined direction. Recently, calculations based on the square wire assumption have been performed for nanowires oriented along the three principal axes [1]. We provide here a solution to the dispersion relation for nanowires of circular cross-section, taken into consideration the anisotropic carrier pockets and the non-parabolicity of the band structure for an arbitrary crystal direction. Details of the calculations are presented elsewhere, and only results are summarized here. Figure 2(a) shows the calculated band edge energy of the first subband at 77 K for the three L -point electron pockets and the T -point hole pocket as a function of wire diameter for nanowires oriented along the (012) direction. We note that the three electron pockets split into two groups: the pocket with its major axis along a bisectrix axis has a higher subband energy compared to the other two degenerate electron pockets. For wires with a diameter < 50 nm, the energy of the lowest electron subband exceeds that of the highest hole subband, indicating that these nanowires are semiconducting.

Since the band parameters of Bi are strongly temperature dependent for $T > 80$ K [5,11,12], the critical wire diameter for the semimetal-semiconductor transition will also

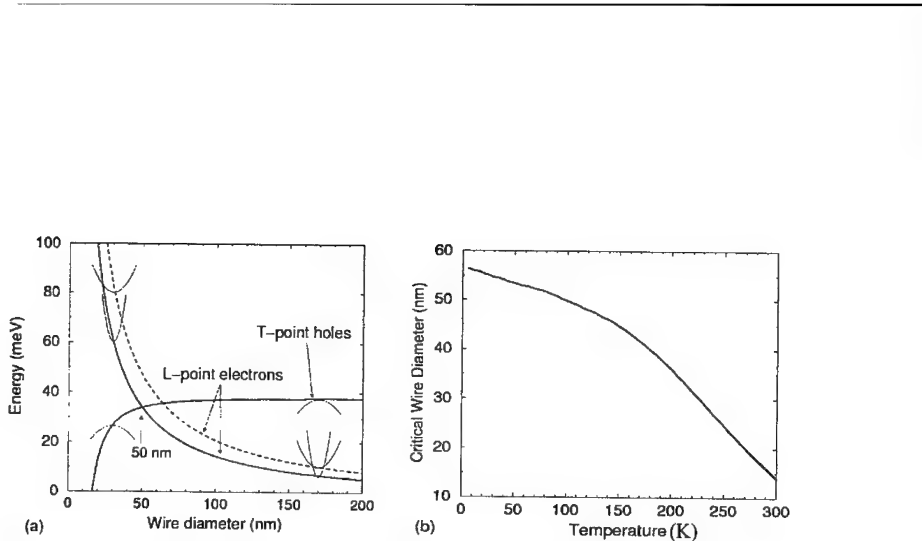


Figure 2. (a) Calculated results for the band edge energy of the first subband for the three L-point electron pockets and the T-point hole pocket as a function of wire diameter for nanowires oriented along the (012) direction at 77 K. (b) The critical nanowire diameter d_c for the semimetal-semiconductor transition calculated as a function of temperature for Bi nanowires oriented along the (012) direction.

be temperature dependent, which must be taken into account when studying the temperature dependence for transport properties of Bi nanowires. Because the direct bandgap at the L point, the band overlap and the electron effective mass all increase with temperature, smaller nanowires are required for the semimetal-semiconductor transition at higher temperatures (see Figure 2(b)). For Te-doped Bi nanowires, we assume for simplicity that each Te atom donates one electron to the conduction band and that the ionization energy is negligible for all T of interest.

Two-Point Resistance Measurements

Since the nanowires are embedded within the anodic alumina template and only two ends of the wires are exposed, we cannot perform a conventional four-point measurement to obtain an absolute conductivity value for a single nanowire without breaking or dissolving the alumina template. Therefore, a pseudo-four-point method was adopted to measure the resistance of the nanowire composite. In this setup, silver paint was applied onto both sides of the template to make good ohmic contacts, to which two gold wires were attached on each side. One pair of the gold wires was connected to a current source and the voltage drop was measured across the other pair of gold wires. Since the number of Bi nanowires connected by the silver paint is unknown, we cannot obtain an absolute resistivity value. However, the T dependence of the resistivity can be studied by normalizing the resistance $R(T)$ to the resistance at a fixed common temperature (e.g. $R(270\text{ K})$); in this way, the T dependence of the resistivity for different samples can be compared.

Figure 3(a) shows the T dependence of the resistivity of Bi nanowire samples with different Te doping concentrations. The average diameters of the three samples are all $\sim 40\text{ nm}$. The concentrations quoted in Figure 3(a) were based on the ratio of the Bi and Te atoms that were introduced into the quartz tube. The resistance values for the samples ranged from a few hundred ohms to several thousand ohms. The T dependence of the resistivity was very different for samples with different Te concentrations. For all three samples, the resistance increased as the temperature decreased. However, pure Bi nanowires showed the strongest temperature dependence, with $R(4\text{ K})$ being ~ 2.3 times

the resistance at 300 K. In contrast, for the sample with the highest dopant concentration (0.15 at% Te), the resistance was almost constant between 2 K and 100 K. The very different temperature dependence of resistance can be qualitatively explained in terms of the difference in donor concentration (N_d) within the Bi nanowires.

According to the theoretical calculations shown above, the 40 nm Bi nanowires will undergo a semimetal-semiconductor transition at $T \leq 170$ K. Thus, for $T \leq 170$ K, the intrinsic carrier density will drop significantly with decreasing T , just like a semiconductor. Figure 3(b) shows the calculated carrier density of a 40 nm nanowire as a function of T for different donor carrier concentrations. At low temperatures where the intrinsic carriers are overwhelmed by the carriers from the dopants, the total carrier density is essentially constant and is governed by the dopant concentration. As the temperature rises, the number of intrinsic carriers will increase exponentially, and will eventually exceed the number of dopant carriers above a certain threshold temperature, so that the carrier concentration will again be dominated by the intrinsic carriers in this high-temperature regime. At high temperatures (≥ 200 K), the phonon scattering is usually the dominant scattering mechanism, which has the same effect on samples with different doping levels. Therefore, the resistance for different samples will exhibit a similar T dependence, since they all have roughly the same temperature dependence for carrier concentrations and mobilities at temperatures higher than 200 K (see Fig. 3(b)). On the other hand, in the low-temperature regime, ionized impurity scattering plays a more important role in the mobility of the Te-doped Bi nanowires, compared to that of the intrinsic Bi nanowires. However, since the mobility usually has a much weaker temperature dependence than the carrier concentration, the overall (normalized) resistance will be smaller for the Te-doped Bi nanowires at low temperatures. Thus, Te-doped nanowires are expected to have a temperature dependence for resistance similar to the intrinsic nanowires at high T , and to behave like an extrinsic semiconductor at low T .

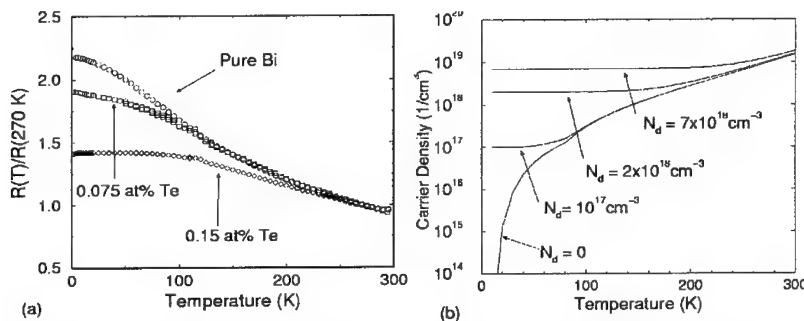


Figure 3. (a) Temperature dependence of resistance for 40 nm pure or Te-doped Bi nanowire arrays. The resistances of the nanowire samples at a given temperature are normalized to their resistance at 270 K. (b) The calculated carrier density of 40 nm Bi nanowires of various dopant carrier concentrations (N_d) as a function of temperature.

CONCLUSIONS

Te-doped Bi nanowires synthesized by the pressure injection technique have been examined experimentally and theoretically. The Bi crystal structure is preserved in the 1D nanowire system; the 40 nm Te-doped Bi nanowires possess a preferential growth orientation perpendicular to the (012) crystal plane. The critical wire diameter d_c for the semimetal-semiconductor transition in Bi nanowires is predicted to be 50 nm at 77 K; d_c is expected to decrease with increasing T . Two-point resistance measurements show that undoped Bi nanowires exhibit a stronger T dependence than Te-doped Bi nanowires; the T dependence further weakens as the dopant concentration increases. The different temperature dependences for resistance of samples with different dopant carrier concentrations are found to be consistent with the theoretical predictions.

ACKNOWLEDGMENTS

The authors thank Prof. G. Chen of UCLA and Dr. J. Heremans of Delphi Corporation for stimulating discussions. The support from MURI subcontract 0205-G-7A114-01, NSF grants CTS-9257223 and DMR-98-04734, and US Navy contract N00167-92-K005 are also gratefully acknowledged.

REferences

1. X. Sun, Z. Zhang, and M. S. Dresselhaus, *Appl. Phys. Lett.* **74**, 4005 (1999).
2. L. D. Hicks and M. S. Dresselhaus, *Phys. Rev. B* **47**, 16631 (1993).
3. Z. Zhang, X. Sun, M. S. Dresselhaus, J. Y. Ying, and J. Heremans, *Appl. Phys. Lett.* **73**, 1589 (1998).
4. Z. Zhang, X. Sun, M. S. Dresselhaus, J. Y. Ying, and J. Heremans, *Phys. Rev. B*, in press.
5. J. Heremans and O. P. Hansen, *J. Phys. C: Solid State Phys.* **12**, 3483 (1979).
6. Z. Zhang, J. Y. Ying, and M. S. Dresselhaus, *J. Mater. Res.* **13**, 1745 (1998).
7. H. Masuda and M. Satoh, *Science* **268**, 1466 (1995). H. Masuda and M. Satoh, *Jpn. Appl. Phys.* **35**, 126 (1996).
8. Z. Zhang, D. Gekhtman, M. S. Dresselhaus, and J. Y. Ying, *Chem. Mater.* **11**, 1659 (1999).
9. R. T. Isaacson and G. A. Williams, *Phys. Rev.* **185**, 682 (1969).
10. B. Lax and J. G. Mavroides, in *Advances in Solid State Physics*, Vol. 11, (Academic Press, New York, 1960).
11. C. F. Gallo, B. S. Chandrasekhar, and P. H. Sutter, *J. Appl. Phys.* **34**, 144 (1963).
12. M. P. Vecchi and M. S. Dresselhaus, *Phys. Rev. B* **10**, 771 (1974).

Transport Measurements of Individual Bi Nanowires

Stephen B. Cronin^b, Yu Ming Lin^a, Takaaki Koga^d, Jackie Y. Ying^c, and Mildred S. Dresselhaus^{a,b}

^aDepartment of Electrical Engineering and Computer Science,

^bDepartment of Physics, and ^cDepartment of Chemical Engineering,
Massachusetts Institute of Technology, Cambridge, MA 02139

^dDivision of Engineering and Applied Sciences, Harvard University,
Cambridge, MA 02139

ABSTRACT

Transport properties are reported for Bi nanowires, prepared by the filling of an alumina template with molten Bi. The temperature dependence of the resistance is presented for such arrays of Bi nanowires with diameters in the 40 to 200nm range. The data are understood qualitatively on the basis of a model for a quantum-confined system. Finally, a 4-point measurement is performed on an individual Bi nanowire prepared by using an electron beam lithography technique. Techniques for handling the practical issues of non-ohmic contacts and wire burn-out are given. The physical significance of the final results of the measurements are discussed in light of various scattering mechanisms in the nanowire.

INTRODUCTION

Constant demand for higher computer performance has forced the circuits in CPUs to be made smaller and smaller. As this trend continues new methods for fabricating and predicting the properties of nanoscale conductors will become essential for further increases in performance for future generation CPUs. The confinement of electrons to very small wires can have profound effects on the transport properties of the material, causing it to deviate greatly from its bulk properties. As will be shown in this paper, for small enough wire size, Bi transforms from a semimetal to a semiconductor. We would like to understand the changes in materials properties as the size of the wires are made very small. The Bi nanowires discussed in this work are prepared by non-lithographic means, and can be made as small as 7nm in diameter. While there is no way to arrange these wires, as of yet, to form logic circuits, the Bi nanowire system in many ways is ideal for the study of phenomena occurring in very small conductors.

The unique electronic properties of bismuth make it an exceptional material for the study of low dimensional phenomena. Because of Bi's very low effective mass ($\sim 0.001m_0$), the electronic bound state energies in small diameter Bi wires are much larger for Bi than in any other material system (e.g. gold $m \sim m_0$), making the effects of quantum confinement more easily observable. Also, the large electron mean free path ($\sim 1\mu\text{m}$) makes Bi nanowires a viable system for studying ballistic transport.

In this work, Bi nanowire samples are prepared by filling an anodic alumina (Al_2O_3) template with Bi. The anodic alumina templates are prepared by an electrochemical method, discussed in detail elsewhere in this volume [1]. These templates contain a

close-packed array of empty channels, which extend continuously from one side of the template to the other. The channel diameter can be made between 7 and 200nm by varying the electrochemical growth parameters. The template is then filled with either molten Bi [1,2,3] or with Bi from the vapor phase [4]. From X-ray diffraction measurements, it was found that the deposited Bi crystallizes with a preferred orientation with respect to the wire axis. Doping of the Bi with Te has also been studied, and is discussed elsewhere [1]. For measurements on individual nanowires, the nanowires are removed by dissolving the template in acid to leave a solution of free standing nanowires.

In addition to the large body of work describing the fabrication of Bi nanowires, extensive theoretical work has been done on this system in predicting its electronic properties [5]. One of the most interesting phenomena that occurs in low dimensional systems is the quantum confinement shifting of the energy of the band edges. This effect increases as both the wire diameter decreases, as shown in Fig. 1, and also as the temperature decreases [1].

The calculation of band shifts in this work assumes a circular wire cross-section, corresponding to the experimental situation, whereas previous calculations had assumed a square wire cross-section [5]. Here we choose the trigonal crystalline orientation for simplicity to demonstrate the concept, since the three L-point electron pockets are degenerate for this orientation. In bulk form, Bi is a semimetal, with a band overlap of 38meV. As the wire diameter gets smaller than a critical diameter d_c , the conduction band no longer overlaps the valence band and the material becomes a semiconductor with a band gap. As one might expect, the properties of the material change dramatically below this d_c . Since the Bi nanowire samples prepared in this work are not oriented along the trigonal axis, the semimetal to semiconductor transition occurs at a slightly different value of d_c than shown in Fig. 1.

2-POINT RESISTANCE MEASURMENTS OF Bi NANOWIRE ARRAYS

Measurements of arrays of Bi nanowires in the anodic alumina templates can be made by attaching leads to either side of the sample with silver paint or low temperature solder. Since we don't know how many wires are contributing to the conduction or the precise conduction length, it is not possible at present to deduce the resistivity of the sample from these measurements. However these samples can provide the temperature dependence of the resistivity. Shown in Fig. 1 is the resistance normalized to room temperature for samples of various wire diameters in comparison to bulk Bi. We find the temperature dependence of the resistance of the nanowires to be different from that of bulk Bi. The bulk Bi sample shows semimetallic behavior where the resistance increases with temperature. For larger diameter wires (~200nm), a peak in the resistance is observed below 100K. We understand this behavior on the basis of the decrease in the band overlap, as depicted in Fig. 1, and also the increase in scattering at the wire boundary and grain boundaries. At low temperatures the dominant scattering mechanism is scattering at grain boundaries and wire boundaries. As the temperature increases, the number of phonons increases, causing the resistance to increase, just as in bulk Bi. Above about 100K, however, the carrier density increases rapidly due to the increasing band overlap with temperature and also increased thermal excitation of carriers, causing the resistance to drop. For samples with small wire diameters, the resistance above 100K

decreases monotonically with temperature as in a semiconductor. From the dependence of $R(T)$ on wire diameter we see evidence for the band energy shifting predicted theoretically. These results are in agreement with other work in the literature [4].

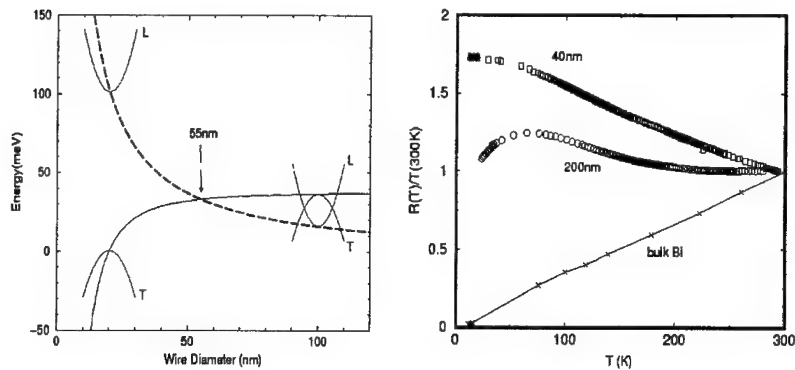


Figure 1. Left: The band energies in Bi nanowires plotted as function of wire diameter for wires with the trigonal orientation along the axis of the wire at 77K. Right: 2-point resistance of Bi nanowire arrays normalized to room temperature plotted versus temperature. Samples of 40nm and 200nm wire diameter are shown in comparison to bulk Bi. Bulk data taken from [4].

4-POINT RESISTIVITY MEASUREMENTS OF INDIVIDUAL Bi NANOWIRES

Although the 2-point measurement has the great advantage of requiring no special equipment and no long and expensive lithographic procedures, its geometry is inherently limiting in that the number of wires contributing to the conduction is unknown. In order to determine the absolute resistivity, the nanowires must be removed from the alumina template and electrodes must be attached to one nanowire at a time. The resistivity can then be determined from a resistance measurement by knowing precisely the cross-sectional area and length of conduction. Although the temperature dependence of the 2-point resistance measurement gives a qualitative picture about whether the sample is metallic or semiconducting, 2-point resistance measurements on Bi nanowire arrays still give only qualitative data about the electronic structure and the transport properties. The resistivity contains more quantitative information about the carrier density and the scattering times of the sample, which we would like to compare to our model and test the assumptions on which it is based. Further motivation for measuring the resistivity is that, as mentioned above, much of the current interest in Bi nanowires is fueled by their potential application as a low temperature thermoelectric material [6,7]. In order to evaluate the potential thermoelectric efficiency of these wires, the absolute resistivity must be known.

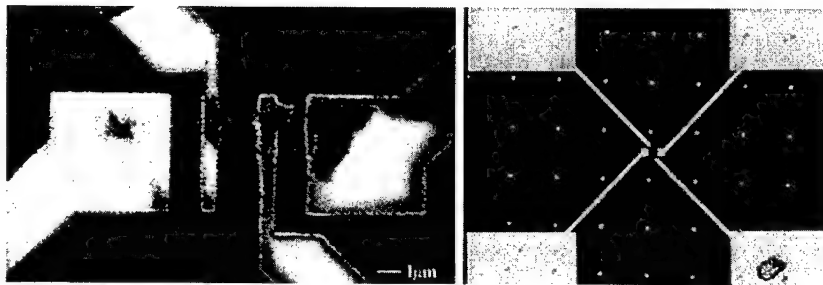


Figure 2. Left: SEM image of a 70 nm Bi nanowire with four electrodes burnt out by electrostatic discharge. Right: Optical image of a larger area of the lithography pattern. The nanowire lies at the center of the 'X' pattern.

In this work, electrodes were patterned on top of the nanowires using an electron beam lithography technique. The electrodes consist of 1000Å of gold with a 50Å adhesion layer of chromium. The processing of these electrodes follows a standard 'lift off' method. Details of this technique are described elsewhere [8].

The small size of the nanowires and the low melting point of Bi (~271°C) make the Bi nanowires especially prone to being burnt out by static discharge. If care is not taken to prevent unwanted currents from passing through the wire, the sample will be ruined, as shown in Fig. 2. The figure shows an SEM image of a 70nm Bi nanowire underneath four gold electrodes that was burnt out by electrostatic discharge. In order to prevent this from happening, the sample must be kept shorted at all times, until right before the measurement is taken. More details about static protection are given below.

The right image in Fig. 2 shows a large area of the pattern that is written using an electron lithography technique. The entire pattern consists of four large bonding pads (300μm x 300μm) and four leads that extend inward forming an 'X' shape connecting the large bonding pads to the four electrodes shown in the SEM image. Along the perimeter of the pattern, not shown, the bonding pads are shorted to each other by thin conducting strips. These strips prevent static discharge through the wire resulting in the damage shown in the SEM image. After the meters are connected and the sample is shorted externally, these strips are cut with a diamond scribe, and static discharge is avoided.

In characterizing the I-V response of the contacts, I-V was measured across the inner two electrodes of the sample as a 2-point measurement. It was found that the contacts were highly non-ohmic, resembling a diode, as shown in Fig. 3. The diode-like I-V response is attributed to the junction of the two dissimilar metals, chromium and bismuth in this case, separated by an insulating oxide layer, in this case probably Bi oxide. Indeed it was found that the voltages of the standard 4-point method were so noisy that no meaningful data could be attained. In order to reduce the noise to get reasonable data, a second current source was used to run a small constant bias current across the voltage leads. This small constant bias current shifts the I-V response of the contacts away from the origin into a more linear (more ohmic) regime. This results in a shift of the I-V curve by a constant voltage, while preserving the slope, and hence the measured resistance. The addition of this second current source resulted in a dramatic improvement in the quality of the data. The I-V data taken using this scheme is shown in

Fig. 3 for the 70nm wire shown in the inset of this figure. As expected, the resulting measured resistance was independent of the magnitude of the bias current.

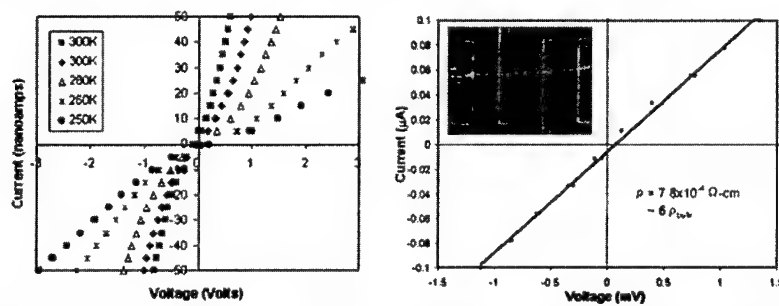


Figure 3. Left: 2-point I-V plot across inner electrodes at various temperatures. Right: 4-point I-V plot for 70nm Bi nanowire with a bias current of 6nA. The inset shows an SEM image of the wire with four gold electrodes.

The resulting resistivity of a 70nm diameter Bi nanowire at 300K was determined to be approximately 6 times greater than that of bulk Bi. From theoretical modeling, the band shifts due to quantum confinement are expected to affect the carrier density at room temperature negligibly, so that the increase in resistivity must be attributed to increased scattering at the wire boundaries and grain boundaries within the wire. TEM (transmission electron microscopy) has shown that the nanowires prepared in this work contain grain boundaries on the order of the size of the wire diameter. The presence of these grain boundaries, not present in bulk Bi, is expected to increase the resistivity of the sample.

We would ultimately like to extend these resistivity measurements to low temperatures and over a variety of wire diameters. However, as shown in Fig. 3 the problem of making ohmic contacts becomes more serious as the temperature is lowered even to 0°C. In the future we will focus on eliminating the oxide layer which is believed to be responsible for the non-ohmic behavior.

CONCLUSIONS

Two-point measurements of the resistance have been performed on arrays of Bi nanowires as a function of temperature and wire diameter. The data are understood on the basis of our physical expectations of the system. The quantum confinement of carriers in the nanowires and the expected changes in the dominant scattering mechanisms explain qualitatively the dependence of the sample resistance on temperature and wire diameter.

A method for affixing four electrodes on top of an individual nanowire was developed and carried out. Results of these 4-point resistivity measurements agree qualitatively with our basic understanding of the bismuth nanowire system. We plan to extend these measurements over a range of temperatures and wire diameters, and examine the validity of our transport model for bismuth nanowires quantitatively.

ACKNOWLEDGMENTS

The authors would like to thank Dr. J. Heremans at Delphi Automotive Systems for help with sample preparation and valuable discussions, also X. Sun, Z. Zhang, M. Mondol, Prof. H. Smith, Dr. G. Petrich, A. Erchak at MIT and D. Bozovic at Harvard University for advice and guidance. The authors gratefully acknowledge support from MURI subcontract 0205-G-7A114-01, NSF grants CTS-9257223 and DMR-98-04734, and US Navy contract N00167-98-K-0024.

REFERENCES

1. Y.M. Lin, X. Sun, S. B. Cronin, Z. Zhang, J. Y. Ying, and M. S. Dresselhaus, *Fabrication and Charactorization of Te-Doped Bi Nanowire Arrays*, in MRS Symposium Proceedings, Boston, (1999).
2. Z. Zhang, J. Y. Ying, and M. S. Dresselhaus, *J. Mater. Res.*, **13**, 1745 (1998).
3. Z. Zhang, X. Sun, M. S. Dresselhaus, J. Y. Ying, and J. Heremans, *Electronic transport properties of single crystal bismuth nanowire arrays*, *Phys. Rev. B*, **60**, accepted 10/27/99.
4. J. Heremans, C. M. Thrush, Z. Zhang, X. Sun, M. S. Dresselhaus, J. Y. Ying, and D. T. Morelli, *Phys. Rev. B* **58**, R10091 (1998).
5. X. Sun, Z. Zhang, and M. S. Dresselhaus, *Appl. Phys. Lett.*, **74**, 4005 (1999).
6. M. S. Dresselhaus, Y.-M. Lin, G. Dresselhaus, X. Sun, Z. Zhang, S.B. Cronin, T. Koga and J. Y. Ying, in *The 18th International Conference on Thermoelectrics: ICT Symposium Proceedings, Baltimore*, (1999).
7. M. S. Dresselhaus, Z. Zhang, X. Sun, J. Y. Ying, J. Heremans, G. Dresselhaus, and G. Chen, in *Thermoelectric Materials--The Next Generation Materials for Small-Scale Refrigeration and Power Generation Applications: MRS Symposium Proceedings, Boston*, edited by T. M. Tritt and H. B. Lyon and G. Mahan and M. G. Kanatzidis (*Mater. Res. Soc. Proc.* **545**, Pittsburgh, PA, 1999) pp. 215 (1999).
8. S. Cronin, Y.-M. Lin, T. Koga, X. Sun, J. Y. Ying, and M. S. Dresselhaus, in *The 18th International Conference on Thermoelectrics: ICT Symposium Proceedings, Baltimore*, (1999).

Plasmonics: Electromagnetic energy transfer and switching in nanoparticle chain-arrays below the diffraction limit

Mark L. Brongersma, John W. Hartman, and Harry H. Atwater

Thomas J. Watson Laboratory of Applied Physics,
California Institute of Technology,
Pasadena CA 91125

ABSTRACT

A model is given for the transport of electromagnetic energy through structures that consist of chains of closely spaced metal nanoparticles. This transport relies on the near-field electrodynamic interaction between metal particles that sets up coupled plasmon modes. The model predicts that the propagation is coherent and the group velocities can exceed typical saturation velocities of electrons in semiconductors ($\approx 10^7$ m/s). Furthermore, it is shown that in these structures propagation of energy around sharp corners (bending radius \ll the wavelength of visible light) is possible at high efficiency. This efficiency is a strong function of the frequency and polarization direction of the plasmon mode. The operation of a plasmon switch is modeled, in which plasmon waves can be switched or modulated. Finally, suggestions are given for the choice of metal particle and host material.

INTRODUCTION

Integrated optics faces the fundamental limitation that, for the guiding, modulation, and amplification of light, structures are needed that have dimensions comparable to the wavelength of light [1,2]. Recently, it was theoretically shown that this problem might be circumvented by transporting electromagnetic (EM) energy in optical waveguides with a metallic core [2], or along linear chains of closely spaced metal nanoparticles [3]. Although these structures exhibit severe transmission losses due to radiation and heating, about 3dB/500 nm, they could add new functionality to existing optoelectronic integrated circuits (OEICs).

At the surface-plasmon frequency, light strongly interacts with metal particles and gives rise to collective electron motion, or plasmons [4]. For metals these frequencies are typically in the visible and near infra-red [4]. In particles of nanometer size (\ll wavelength of the exciting light, λ) plasmon excitations produce an oscillating dipole field. The EM energy transport along chains of metal nanoparticles relies on the near-field electrodynamic interaction between metal particles that sets up coupled dipole or plasmon modes [5]. This type of coupling is analogous to the process of resonant energy transfer (RET), which is observed in systems that contain closely spaced optically excited atoms, molecules, or semiconductor nanocrystals [6-8].

This letter, for the first time to our knowledge, describes the transport of EM energy through corners, T's, and switches that consist of chains of metal nanoparticles. In combination with other structures they form the basic building blocks for fully interconnected systems of complex architecture. These "plasmonic devices" potentially are among the smallest possible structures with optical functionality. This letter discusses the dependence of their behavior on the metal particle size, interparticle spacing, the polarization direction of plasmon mode, and the dielectric properties of the host matrix.

DISPERSION RELATION FOR PLASMON MODES

In the first part of this section it is demonstrated that propagation along chains of equally spaced metal particles is coherent and the dispersion relation for the energy migration is determined in the point-dipole limit. Then the propagation of EM energy in other structures, built up of chains of metal particles such as corners, T-junctions, and eventually a switch are modeled.

To determine the dispersion relation for plasmon modes we consider a linear chain of equally spaced metal particles separated by a distance d , as is shown in Figure 1. In the analysis we distinguish between plasmon modes with dipole moments oriented perpendicular to the chain-axis, the transverse (T) plasmon modes, and plasmon modes with dipole moments along the propagation direction, the longitudinal (L) modes. A mode is defined by the magnitude of all the induced dipole moments, $p_{i,m}(t)$, in the polarization direction, i , at all points, m , of the chain.

In general, the electric field from an oscillating dipole, E_p , at a certain point is a function of the distance, R , from this point to the center of the dipole. The electric field vector consists of three terms: $E_p = E_F + E_M + E_R$, where E_F is proportional to R^{-3} , E_M to R^{-2} , and E_R to R^{-1} [8]. The term E_R describes the radiation field and dominates when $R \gg \lambda$. In the quasi-static limit, $R \ll \lambda$, E_F , the Förster field, is dominant. For this reason, the description of the interaction between two closely spaced dipoles ($d \ll \lambda$) only involves the Förster field. An oscillating dipole $p_{i,m}$ at a point m in the chain thus produces an electric field, $E_{i,m}$, at the neighbor locations, $m-1$ and $m+1$, that is given by:

$$E_{i,m}(t) = -\frac{\gamma_i p_{i,m}(t)}{4\pi\epsilon_0 n^2 d^3}, \quad (1)$$

in which γ_i is a polarization dependent constant for which $\gamma_T = 1$ and $\gamma_L = -2$, ϵ_0 is the free space permittivity, and n the refractive index of the host material [8]. The $1/d^3$ dependence of $E_{i,m}$ ensures that only nearest neighbor interactions need to be taken into account [9]. When the dipoles in the chain are assumed to be Hertzian [10], then $p_{i,m} = qx_{i,m}$, where q is the magnitude of the oscillating charge and $x_{i,m}$ its distance from equilibrium in the i -direction at point m in the chain. From the equation of motion for the charges that make up the dipole it follows that:

$$\ddot{p}_{i,m}(t) = -\omega_0 p_{i,m}(t) - \gamma_i \omega_1 [p_{i,m-1}(t) + p_{i,m+1}(t)], \quad (2)$$

where the first term describes the eigen-motion of the dipoles at a circular resonance frequency ω_0 and the third term incorporates the electrodynamic interaction with the nearest neighbor dipoles at $m-1$ and $m+1$. The value of ω_1 is given by $\omega_1 = qe/4\pi m_e \epsilon_0 n^2 d^3$, in which m_e is the electron mass and e the electron charge. For a spherical Ag nanoparticle of 10 nm radius, the magnitude of the oscillating charge is given by $q = \epsilon_0 \rho_{el} V = 3.9 \times 10^{-14}$ C, where ρ_{el} is the electron concentration of Ag ($5.85 \times 10^{22}/\text{cm}^3$ [11]) and V the volume of the particle. For an interparticle spacing $d = 40$ nm and a refractive index of the host material of $n = 1.5$ (SiO_2), we find a value of $\omega_1 = 6.6 \times 10^{14} \text{ s}^{-1}$. For larger values of d and n , the magnitude of ω_1 will be smaller.

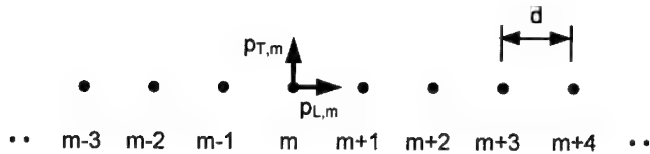


Figure 1. Linear chain of equally spaced metal nanoparticles separated by a distance d . The induced dipole moment at position, m , and polarization, i ($i=T,L$), is given by $p_{i,m}$

$$p_{i,m}(t) = P_i \exp i(\omega t \pm kmd) \quad \text{Propagating wave solutions to equation 2 are of the form}$$

$$, \quad (3)$$

where P_i is the maximum value of the dipole moment in the direction i and k the wave vector of the plasmon wave. The dispersion relation is found by substitution of equation 3 into equation 2:

$$\omega^2 = \omega_0^2 + 2\gamma_i \omega_1^2 \cos(kd) \quad (4)$$

For surface-plasmon resonance in the visible, $\omega_0 \approx 5 \times 10^{15} \text{ s}^{-1}$, and $(\omega_1/\omega_0)^2 \ll 1$. Under these conditions equation 4 can be rewritten as:

$$\omega = \omega_0 + \gamma_i \frac{\omega_1^2}{\omega_0} \cos(kd) \quad (5)$$

The group velocities, $v_{g,i}$, for the two different polarization directions are given by:

$$v_{g,i} = \frac{d\omega}{dk} = -\gamma_i \frac{\omega_1^2}{\omega_0} d \sin(kd) \quad (6)$$

Figure 2 shows the dispersion relations for T and L modes. The bandwidth of the L-branch, $\Delta\omega_L$, is twice as large as that of the twofold degenerate T-branch, $\Delta\omega_T$. At each allowed k value, the L-waves have a $v_{g,L}$ that is twice as large as $v_{g,T}$ and opposite in sign. For both waves the largest v_g is obtained at resonance: $\omega = \omega_0$ and $k = \pm \pi/2d$ ($\lambda = 4d$). For $\omega_1 = 6.6 \times 10^{14} \text{ s}^{-1}$ (see conditions above) and $\omega_0 = 5 \times 10^{15} \text{ s}^{-1}$ we find that the group velocities at resonance are $v_{g,T} = 3.4 \times 10^6 \text{ m/s}$ and $v_{g,L} = 6.8 \times 10^6 \text{ m/s}$. These values are comparable to the saturation velocities of electrons in semiconductors [12]. For these values, the corresponding bandwidths are $\Delta\omega_T = 1.75 \times 10^{14} \text{ s}^{-1}$ (115 meV) and $\Delta\omega_L = 3.5 \times 10^{14} \text{ s}^{-1}$ (330 meV).

CORNERS AND T-JUNCTIONS

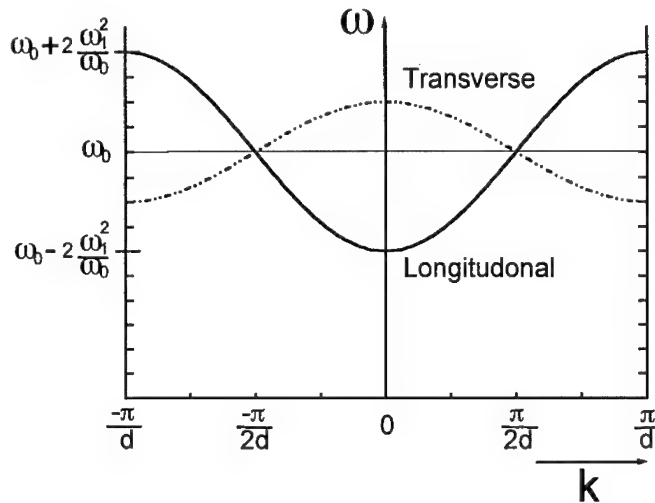


Figure 2. Dispersion relations for plasmon modes that exist in linear chains of polarizable entities as depicted in Figure 1. It shows both the 2-fold degenerate branch of the transverse modes and the longitudinal branch.

The EM energy transport through corners and T-junctions can be calculated by requiring continuity of the dipole waves and conservation of energy flux at the intersection of the chains. In general, part of the incident energy flows through the structure and part is reflected. The transport efficiency depends on 1) the geometry of the structure, 2) the frequency, and 3) polarization directions of the plasmon waves that enter and exit a structure. In this letter only structures that consist of chains and 90° corners are considered. This greatly simplifies the modeling since in that case only three situations need to be distinguished: 1) in a turn an L-wave transforms into a T-wave, 2) in a turn a T-wave transforms into an L-wave, and 3) in a turn a T-wave remains a T-wave. The corresponding efficiencies for the transmission of EM energy are denoted by η_{L-T} , η_{T-L} , and η_{T-T} . At certain values of ω the importance of the frequency and polarization direction is manifested in the dispersion relation showing only L-modes can exist and T-modes are forbidden. This implies that a 90° corner in which L-waves are transformed into T-waves acts as a frequency or polarization filter. In a future paper it will be shown that the transmission efficiency through any structure is maximum at $\omega = \omega_0$ and in the rest of this letter that value of ω is assumed. For example, the power transmission coefficient at ω_0 of 90° corners are $\eta_{L-T} = 8/9$, $\eta_{T-L} = 8/9$ and $\eta_{T-T} = 1$, where 1 corresponds to 100% transport, yielding no reflection. For T-structures we have to distinguish between the situations where the incident plasmon wave is injected into the stem or one of the arms of the T-structure. Injection of plasmon waves into one of the arms is slightly more complicated as part of the wave changes direction and part of it does not. Such a situation will be shown in the discussion of the plasmon switch at the end of this section. For injection into the stem $\eta_{L-T} = 24/25$, $\eta_{T-L} = 16/25$ and $\eta_{T-T} = 8/9$. This shows that power flow around 90° corners with dimensions much smaller than the

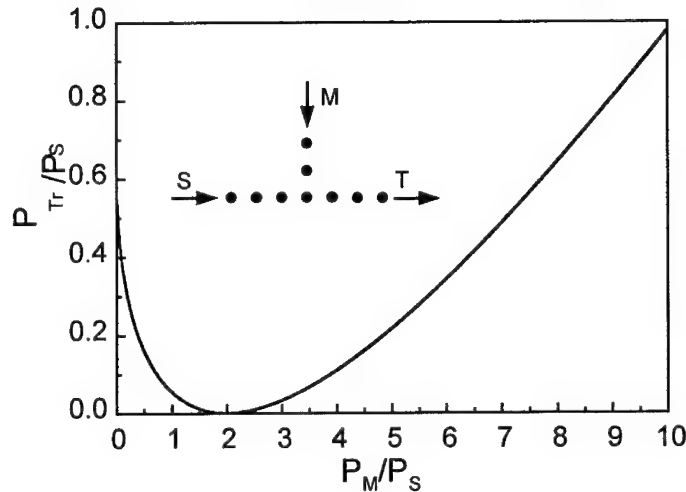


Figure 3. Dependence of the normalized transmitted power, P_{T_s}/P_{S_s} , as a function of the normalized modulation power, P_M/P_S of the switch depicted in the inset. The switch consists of two orthogonal chains of metal nanoparticles. The specific functional dependence is valid for the case that the signal plasmon wave, S, and transmitted plasmon wave, T, are longitudinal and the modulation plasmon wave is transverse and out of phase with S.

wavelength of light is possible at high efficiencies. This is impossible in conventional waveguide technology [1].

PLASMON SWITCH: ACTIVE T-JUNCTION

In the last part of this section a switch is discussed. The simplest switch consists of a T-structure and is pictorially shown in the inset of Figure 3. It shows the incident signal, S, and modulation, M, waves and the outgoing transmitted, T, wave. When the S and M waves have the same polarization and poses opposite phases, they destructively interfere. For a specific ratio of the power in the S-wave, P_S , to the power in the M-wave, P_M , the power in the T-wave, P_T , can be made zero, in other words the switch is in the off state. Figure 3 shows the dependence of the normalized transmitted power, P_{T_s}/P_{S_s} , as a function of the normalized modulation power, P_M/P_S for the case of a longitudinal S-wave and a transverse M-wave. At zero P_M , the value of P_{T_s}/P_{S_s} is determined by the transfer efficiency of the structure for longitudinal S-waves. When P_M/P_S is 2 the switch is in the off state and for higher P_M/P_S the transmitted power is dominated more and more by the power in the M-wave and the dependence of P_{T_s}/P_{S_s} on P_M/P_S becomes linear. The

differential power gain, dP_{Tr}/dP_M , as a function of P_M/P_S is obtained by differentiation of the curve in Figure 3. It is negative below $P_M/P_S = 2$ and positive for larger values.

MATERIALS ISSUES

The transport properties of plasmonic devices are greatly dependent on the size and shape of the metal particles as well as the choice of the metal. Noble metal nanoparticles from Ag, Au, or Cu are preferable to reduce the effect of plasmon waves damping due to resistive heating. For sizes that are large compared to the mean free path of the electrons in the metal, inelastic scattering events of electrons from the metal particle/host matrix interface are minimized (e.g. Ag : $l_{MFP} \approx 50$ nm [4]). The magnitude of v_g can be maximized by using ellipsoidal particles as they can be placed closer together. The choice of host matrix is important in three different ways. First, an increase in n of the host decreases the coupling strength between the particles and thus reduces v_g . Second, by varying n the resonance wavelength can be shifted over several hundred nm from the visible to the near infra-red [13]. Third, a poor choice of host can result in significant damping of the plasmon wave because the plasmons can couple to various degrees of freedom in the host [4].

CONCLUSIONS

We have investigated the behavior of various plasmonic structures and found that we can route and switch EM energy with high efficiency. This work could provide a significant breakthrough, which redefines the conventional requirement in integrated optics that light needs to be guided, amplified, modulated, and switched in structures with dimensions comparable to the wavelength of the guided light.

REFERENCES

1. B.E.A. Saleh and M.C. Teich, *The Fundamentals of Photonics*, (John Wiley & Sons, inc., New York, 1991), p. 238.
2. J. Takahara, S. Yamagishi, H. Taki, A. Marimoto, and T. Kobayashi, Opt. Lett. **22**, 475 (1997).
3. M. Quintin, A. Leitner, J.R. Krenn, and F.R. Aussenegg, Opt. Lett. **23**, 1331 (1998).
4. U. Kreibig and M. Vollmer, *Optical Properties of Metal Clusters*, (Springer-Verlag, Berlin, 1994), p.23.
5. J.R. Krenn, A. Dereux, J.C. Weber, E. Bourillot, Y. Lacroûte, J.P. Goudonnet, G. Schider, W. Gotschy, A. Leitner, F.R. Aussenegg, and C. Girard, Phys. Rev. Lett. **82**, 2590 (1999).
6. Th. Förster, Ann. Physik **2**, 55 (1948).
7. D.L. Dexter, J. Chem. Phys. **21**, 836 (1953)
8. B. W. van der Meer, G. Coker III, S.-Y. S. Chen, *Resonance energy transfer*, (VCH Publishers, 1994), p. 35.
9. The rate of energy transfer between a donor and an acceptor dipole scales with the square of $E_{i,m}$ and thus as $1/d^6$. For this reason, taking into account next-nearest neighbor interactions will not significantly alter these results.

10. Walter Greiner, *Classical Electrodynamics*, (Springer-Verlag, New York 1996), p. 429.
11. C. Kittel, *Introduction to solid state physics*, (John Wiley and Sons, New York 1986), p. 134.
12. S.M. Sze, *Physics of semiconductor devices*, (John Wiley and Sons, New York 1981), p. 44
13. D.D. Nolte, *J. Appl. Phys.* **76**, 3740 (1994).

Nanoscale Patterns of Metal Nanoparticles Chemically-Assembled On Biomolecular Scaffolds: Assembly, Stability and Electron Transport Properties

James E. Hutchison,¹ Leif O. Brown,¹ Jana L. Mooster,¹ Scott M. Reed,¹ Mary E. Schmidt,¹ Laura I. Clarke,² and Martin N. Wybourne²

¹Department of Chemistry, University of Oregon, Eugene, OR 97403-1253 and

²Department of Physics and Astronomy, Dartmouth College, Hanover, NH 03755.

ABSTRACT

A wet chemical approach to preparing one- and two-dimensional arrays of gold nanoparticles assembled onto a polypeptide (poly-L-lysine) scaffold layer is reported. The electrical properties of biopolymer templated and nontemplated gold nanoparticle samples are compared. The electrical response of nontemplated samples is unstable, likely due to nanoparticle mobility. Biopolymer templating provides a simple, chemical method to immobilize the particles and is found to stabilize the electrical response (Coulomb blockade) of the array. A striking feature of the electrical properties is that the electron transport properties are dominated by transport through one-dimensional chains within the sample. Structural studies by AFM and XPS support the transport findings and provide evidence for the formation of one-dimensional assemblies within the arrays.

INTRODUCTION

The novel electronic properties (e.g., Coulomb blockade) of nanometer scale assemblies of metal nanoparticles make them potentially useful in nanoelectronic devices and extremely sensitive chemosensors.[1] To date, no straightforward and reproducible methods are available for the parallel fabrication of low-dimensional nanoparticle assemblies. The method we have been developing for nanofabrication of linear nanoparticle arrays involves the assembly of functionalized metal nanoparticles onto rigid biomolecular scaffolds cast upon an insulating substrate and bridged between narrowly spaced electrodes.

Our previous investigations of nanoparticle thin films provided a clear demonstration of Coulomb blockade at room temperature.[2] In the case of phosphine-stabilized nanoparticles, the Coulomb blockade response is unstable and was thought to be due to the thermal instability of individual nanoparticles. Electron beam patterning of these films lead to enhanced stability of the electrical response, however, Coulomb blockade was only observed at temperatures lower than 195 K suggesting that the patterning method irreversibly alters the nanoparticle core or the ligand shell such that the effective capacitance is lowered. Although thiol-stabilized gold nanoparticles are thermally robust, the Coulomb blockade response still degrades under potential bias.

In the present study, the mechanism of the latter degradation is proposed to involve nanoparticle movement. The use of biopolymer thin films to anchor the nanoparticles is investigated and the electrical properties of the anchored nanoparticle samples are compared to nonpatterned samples. In addition to monitoring the electrical response, assembly of the nanoparticles onto the biopolymer films was directly monitored by x-ray photoelectron spectroscopy and atomic force microscopy.

EXPERIMENTAL

Nanoparticle preparation - Octadecanethiol - stabilized gold nanoparticles (Au(ODT)) were prepared by ligand exchange, as previously reported.[3] TEM images of Au(ODT) yielded a gold core diameter of 1.4 ± 0.5 nm. Mercaptoundecanoic acid - stabilized gold nanoparticles (Au(MUA)) were synthesized by a ligand exchange reaction with Au(TPP) by combining an excess of 11-mercaptoundecanoic acid with Au(TPP) in dichloromethane and stirring for approximately 24 hours under nitrogen. A black precipitate was formed which was washed extensively with dichloromethane. XPS analysis on Au(MUA) indicated complete removal of the triphenylphosphine and chloride ligands and the presence of 11-mercaptoundecanoic acid ligands (Au:S ratio of ca. 2:1). TEM images of Au(MUA) show a gold core diameter of 1.5 ± 0.5 nm.

Electrodes - Prefabricated interdigitated electrodes were purchased from AAI-Abtech of Yardley, PA and had equal finger width and finger spacing dimensions of either ten or fifteen microns. Digit length was 5000 microns. Each electrode had 50 finger pairs that were isolated from large contact pads with long leads. Before use, electrodes were cleaned as suggested by the manufacturer using a UV/Ozone dry process cleaner (Boekel Model 135500). A five-minute exposure was followed by a rinse in nanopure water.

Film deposition/assembly - For non-patterned samples of Au(ODT), a concentrated solution in either dichloromethane was prepared with the addition of heat and drop cast onto an IDA electrode. For patterned samples, a 2.2×10^{-5} mol/l solution of poly-L-lysine (54,000 amu, Sigma as the hydrobromide salt) in 10% water/90% methanol by volume was prepared. A solution of poly-L-lysine was drop cast onto a prefabricated interdigitated array electrode. The coated electrode was submerged in a solution of 1% sodium hydroxide in nanopure water for one to twenty hours. A drop of concentrated solution of Au(MUA) in dimethylsulfoxide was placed on the poly-L-lysine coated electrode. After twenty minutes, the interdigitated area was rinsed with a stream of dimethylsulfoxide (3 - 5 x 5 ml) and then dichloromethane (3-5 x 5 ml). The sample was dried in air or nitrogen.

Electrical measurements and data analysis - Samples were placed on a clean Teflon stage and attached with rigid homemade triaxial connectors. Two terminal measurements were taken in an evacuated environment of approximately 10^{-6} torr. Voltage sourcing and current sensing were accomplished using a Keithley 230 source-measurement unit in remote sensing mode. Voltage changes were limited to one volt or less. Usually, a thirty-second settling time was sufficient to allow the current to reach a steady state. The ultimate resolution of the current measurement was 10 fA. An ohmic leakage current (the current measured for the interdigitated electrode before the sample was deposited) was subtracted from the raw data.

Surface analysis - X-ray photoelectron spectroscopy (XPS) was performed on a Kratos HSi spectrometer. Surface topography was probed in tapping mode with a Digital Instruments Nanoscope IIIa.

RESULTS AND DISCUSSION

The I-V characteristics for drop cast, nontemplated thin films of Au(ODT) and poly-L-lysine-templated Au(MUA) on IDA electrodes are compared in Fig. 1. We first address the characteristics of the nontemplated sample. The response for the Au(ODT) sample is similar to those of phosphine-stabilized nanoparticles, exhibiting initial Coulomb blockade at room temperature followed by degradation of the blockade effect in subsequent scans. The current response above the threshold voltage in Fig. 1A is non-linear - consistent with a 2- or 3-dimensional assembly of nanoparticles.

The most likely causes of the electrical instability seen in Fig. 1A are (a) a capacitance change of the individual nanoparticles or (b) a structural change within the

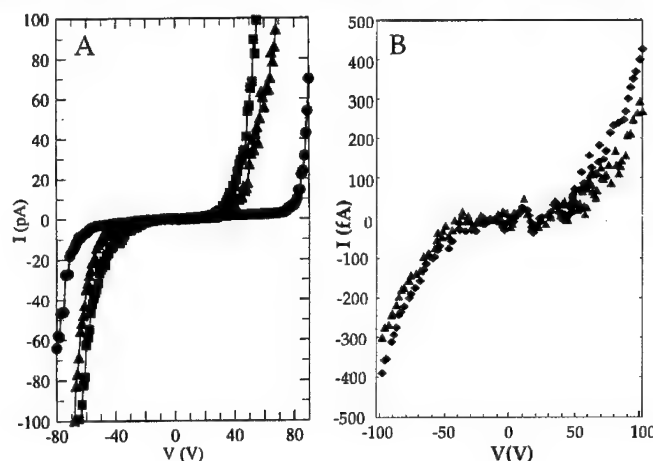


Figure 1. Current-voltage measurements of (A) nontemplated (dropcast) octadecanethiol-stabilized nanoparticles, Au(ODT) and (B) polyL-lysine templated mercaptoundecanoic acid-stabilized nanoparticles, Au(MUA).

film that results in a change in capacitance. We will consider first changes occurring to individual particles. Ligand loss followed by particle aggregation would lead to an increase in particle size, a corresponding increase in capacitance and a loss of Coulomb blockade at room temperature. If ligand loss was the primary cause of degradation of Coulomb blockade, one would expect Au(ODT) to exhibit more stable Coulomb blockade than the phosphine-stabilized nanoparticles because the stability in solution of Au(ODT) is much greater. However, Coulomb blockade in samples of both types of nanoparticles decays rapidly.

Evidence for structural changes within the Au(ODT) films during electrical measurements is found in experiments performed at higher temperatures. In those experiments, currents are 1,000 times larger and rise to a peak followed by a decay to a steady-state current, suggesting an initial reduction/oxidation of material in the vicinity of the electrode contacts followed by a diffusive or migratory transport that is more effective than tunneling. In a related system involving somewhat larger nanoparticles, the melting transition for the alkane chains occurs at 324 K.[4] Thus, at 358 K the chains in Au(ODT) are melted and the nanoparticles exist in a liquid-like matrix wherein

particle movement by diffusion/migration could be facile. In these samples, the melting transition is broad, often extending down to room temperature[5] which could explain particle movement at lower temperatures.

There are a number of possible methods of preventing particle movement, including lowering the temperature and cross-linking the ligand shells. Because the templating methods we are developing are a form of cross-linking, we aimed to investigate whether these methods might prevent particle movement and thus changes in the electrical response. The straightforward deposition method detailed in the Experimental section involves two steps. First, a thin film of poly-L-lysine is cast on the electrode assembly. Following this step, the film is soaked in dilute sodium hydroxide to deprotonate the amino side chains of the poly-L-lysine. The sample was then soaked in a solution containing Au(MUA) and rinsed to remove non-specifically bound nanoparticles. Proton transfer between the acid groups and the amino side chains should result in electrostatic immobilization of the particles.

The I-V characteristics of poly-L-lysine-templated Au(MUA) array are shown in Fig. 1B. In contrast to the nontemplated samples, the Coulomb blockade response shown in Fig. 1B is stable and reproducible. In Fig. 2, the threshold voltage, the voltage where the current discontinuously increases from the baseline, is plotted as a function of the

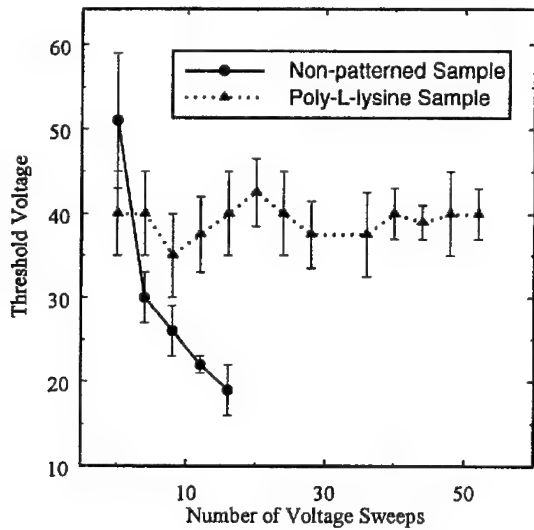


Figure 2. Coulomb blockade threshold voltages for nontemplated Au(ODT) (filled circles) and poly-L-lysine-templated Au(MUA) (filled triangles) nanoparticle thin films as a function of the number of voltage sweeps recorded.

number of consecutive current-voltage scans for both types of samples. Whereas the threshold voltage is seen to decay quickly in the nontemplated sample, the poly-L-lysine-

templated sample is stable, within experimental error, for more than 50 voltage scans. Control experiments involving current-voltage measurements on Au(MUA) samples dropcast onto protonated poly-L-lysine (where electrostatic binding of the nanoparticles does not occur) show that the Coulomb blockade response is only stable when bonding to the biopolymer is possible.

The poly-L-lysine scaffold has a dramatic effect upon the transport in the templated samples and suggests the formation of one-dimensional nanoparticle pathways during the assembly process. Above threshold, the current in the templated samples is nearly linear (Fig. 1B), whereas the nontemplated samples give a strongly non-linear response (Fig. 1A). For disordered one and two-dimensional arrays of normal metal dots where the disorder is introduced by random offset charges placed on each dot, Middleton and Wingreen[6] predict the current above threshold scales as $I \sim (V/V_T - 1)^\zeta$ where ζ is 1 for a one-dimensional system, 5/3 from an analytical calculation for a two-dimensional system and 2.0 ± 0.2 from a numerical calculation for a two-dimensional array. This scaling law has found to apply to one and two-dimensional arrays of metal tunnel junctions and quantum dots. Thus, the linearity of the current response above threshold suggests that the electrical transport is dominated by conduction through one-dimensional pathways.

Each step in the chemical assembly of the templated nanoparticle arrays has been monitored by x-ray photoelectron spectroscopy. In each step, the expected ratios of elements are present, consistent with the described assembly process. After the sodium hydroxide soak, the intensities of the carbon, nitrogen and oxygen signals are significantly lower than before prior to the soak, suggesting that much of the film was removed during this step. AFM studies of the sodium hydroxide-soaked films confirms the removal of poly-L-lysine and reveals the formation of low-dimensional biopolymer aggregates. Images taken after nanoparticle treatment show assembly of the particles onto these aggregates.

CONCLUSIONS

Nontemplated nanoparticle arrays are shown to exhibit unstable Coulomb blockade during measurement of current-voltage characteristics. Current-voltage measurements at elevated temperature suggest particle movement may be responsible for degradation of Coulomb blockade in these samples. The biopolymer templating method described is intended to anchor the nanoparticles in the array, preventing particle motion. Poly-L-lysine-templated arrays show stable Coulomb blockade. No decrease in the threshold voltage occurs during more than 50 voltage sweeps. Finally, the current-voltage characteristics for voltages above the threshold voltage indicate electron transport through one-dimensional particle pathways within the arrays. Such one-dimensional pathways provide opportunities for further physical study and are a step toward nanoelectronic devices based upon Coulomb blockade.

ACKNOWLEDGEMENTS

This research was supported by the National Science Foundation (DMR-9705343; XPS, CHE-9512185; CAREER, CHE-9702726), the Office of Naval Research, the Camille and

Henry Dreyfus Foundation and the University of Oregon. J.E.H. is an Alfred P. Sloan Fellow.

REFERENCES

1. D. V. Averin and K. K. Likharev, in *Mesoscopic Phenomena in Solids*, edited by B. L. Altshuler, P. A. Lee and R. A. Webb (North Holland, Amsterdam, 1991).
2. L. Clarke, M. N. Wybourne, L. O. Brown, J. E. Hutchison, M. Yan, S. X. Cai, and J. F. W. Keana, *Semicond. Sci. Technol.* **13**, A111. (1998)
3. L. O. Brown and J. E. Hutchison, *J. Am. Chem. Soc.*, **119**, 12384 (1997).
4. A. Badia, S. Singh, L. Demers, L. Cuccia, G. R. Brown, and R. B. Lennox, *Chem. Eur. J.*, **2**, 359 (1996).
5. A. Badia, L. Cuccia, L. Demers, F. Morin, and R. B. Lennox, *J. Am. Chem. Soc.*, **119**, 2682 (1997).
6. A. A. Middleton and N. S. Wingreen, *Phys. Rev. Lett.* **71**, 3198 (1993).

SYNTHESIS OF ULTRA-SMALL SI NANO PARTICLE COLLOIDS AND THIN FILMS-HIGH TEMPERATURE SINGLE ELECTRONICS

J. M. Therrien, G. Belomoin, and M. H. Nayfeh
Department of Physics, University of Illinois at Urbana-Champaign,
1110 W. Green St., Urbana, IL, 61801 USA

ABSTRACT

We describe a procedure for dispersing electrochemical etched silicon into a colloid of ultra-small (~ 1 nm) silicon nano particles. The particles are then reconstituted on a Si substrate by gentle evaporation from a volatile colloid, forming thin films. When the colloid or the film is excited with UV radiation at 355 nm, strong blue emission band at 390 nm is observable with the naked eye in room light. Two-terminal I-V spectra of the deposited film, taken using a scanning tunneling microscope (STM), show a single regular conductance resonance at a spacing of 0.25-0.30 eV, consistent with single electron charging. However, under light irradiation, we observe a second regular resonance, for negative tip biasing less than -1 eV, that modulates the charging structure at ~ 1.0 eV period, consistent with the particle's quantum energy level spacing. This paves the way for operation of high-temperature Si-based single electron devices.

INTRODUCTION

In single electronics (single electron technology), device operation is based on the concept of one carrier for one bit of information[1]. That is, it is based on one-by-one manipulation of electrons through a small sub-structure. For observation of effects based on the discreteness of the electrical charge and the discreteness of the quantum energy levels at high temperature, much smaller structures than presently available must be used, such that the quantum energy spacing become larger than room temperature thermal energies. Since the capacitance is inversely proportional to the diameter of the particle, whereas the quantum energy is inversely proportional to the square of the diameter, the potential energy due to the discreteness of the charge is more important for larger sizes. At an intermediate size of 5 nm, the two become comparable. The quantum energy dominates, however, for ultra-small particles.

In this paper we report on a method for dispersing electrochemical etched silicon or porous silicon [2] into individual nano particles. Direct imaging using high resolution transmission electron microscopy shows that the particles are 1 nm in diameter, and material analysis profiles using electron photo spectroscopy show that the particles are composed of silicon with no oxygen present. Upon irradiation with 355 nm UV radiation, emission from the colloid is found to be dominated by an extremely strong deep blue band centered at 390 nm, with a structureless weak orange/red tail (690 - 490

nm), and a weak infrared band centered at 760 nm. Thin films of particles are formed on device quality silicon substrates by gentle evaporation from a volatile particle colloid. The particles are small enough such that the quantum energy spacing is threefold larger than the single electron characteristic charging energy, and such that both are large enough to dominate the thermal fluctuation energy at room temperature or higher by a factor of 10 to 40, allowing comfortable high temperature operation of single electronics.

SAMPLE PREPARATION AND CHARACTERIZATION

We etch a single crystalline silicon wafer in an anodization solution of a mixture of HF acid, H_2O_2 liquid, and methanol[3,4]. The silicon wafers are (100) oriented, 1-10 ohm-cm resistivity, p-type boron-doped silicon wafers. The wafer and a platinum cathode are connected to a constant current source. The silicon wafer is vertically immersed in the etchant and is advanced, at a reduced speed of ~ 1 mm per hour[4], vertically into the solution, at a certain distance from the immersed platinum cathode. While advancing the wafer, the current is maintained at a constant value (15 mA). In lateral anodization, the current has the highest concentration at the meniscus (air-liquid interface), resulting in a higher etching rate hence in ultra-small weakly interconnected nanostructure. Advancing the sample in the liquid slowly and uniformly, results in a large area of the sample that is meniscus-like, hence enriching the ultra small nano substructure. The sample is then immersed in an ultra sound acetone bath [5] for a brief period of time. Under the ultra sound treatment, the very top layer of the luminescent film crumbles into ultra small particles, leaving behind the bottom layer of the film, a deep red luminescent material. The colloid is left to settle. Larger yellowish / orangish luminescent particles precipitate in a few hours, leaving behind a luminescent bluish colloid. The colloid is stable as the sample retains its characteristic emission over weeks, indicating that the particles are small enough to stay in suspension.

We determined the size of the particles by direct imaging using high resolution transmission electron microscopy. A thin graphite grid was coated with the particles by immersion in the colloid. Figure 1a shows that most of the particles are 1 nm in diameter, with only a small percentage in the range 1-3 nm. Material analysis profiles using electron photoluminescence shown in Figure 1b shows that the particles are composed of silicon with no oxygen present. We should note that the dual nature of oxidation and etching provided by the combination of HF and H_2O_2 in the etchant provides continuous refreshing of the luminescent layer over the duration of the treatment. Such a procedure reduces the substructure and eliminates needle- (wire-) like structures. Infrared and Auger electron spectroscopy[4,6] show that the procedure also leaves on the surface a more complete and better quality of hydrogen, free of electronic defects such as di- or tri-hydrides[4], with no oxygen at all[4,6]. Moreover, the results.

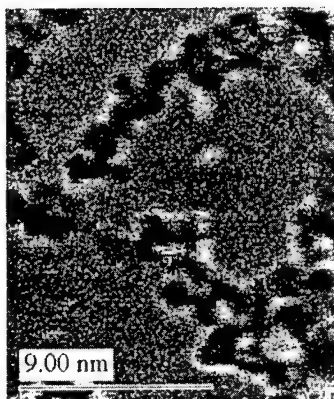


Figure 1 a

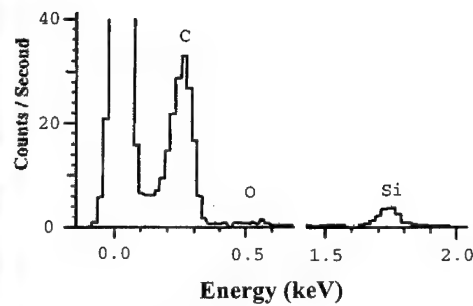


Figure 1 b

show very little residual impurities such as carbon[4] as H_2O_2 is known to be the most powerful and commonly used oxidant to remove nearly every kind of contamination (organic material, metals, alkalines, and metal hydroxides) from silicon surfaces by oxidative dissolution and complex formation. The measured size was also confirmed by two-photon fluorescence correlation spectroscopy (FCS) of particles in the colloid in which we determined the auto correlation function of the luminescence and compared it to a fluorescein dye molecule standard with known density, diffusion coefficient, and size[7].

The luminescence was recorded on a photon counting spectro-fluorometer with a Xe arc lamp light source and 4 nm bandpass excitation and emission monochrometers, with suitable filtering and correction for spectral response. The emission detector has a cut off wavelength at 950 nm. Figure 2 gives the emission spectrum of the dispersed particles and illustrates its development with the excitation wavelength at 330, 350, 365, and 400 nm. Each of the spectra encompasses the visible spectrum but is dominated by a strong blue band with a structureless weak red / orange tail, and a weak infrared band. We also note that when the colloid is excited by the third harmonic of an Nd-Yag laser at 355 nm and 30 ns pulse duration, the blue emission is observable with the naked eye, in room light. For illustration, a photograph of the emission under these conditions is shown in Figure 3. Excitation spectra, which consist of recording the luminescence intensity as a function of excitation energy for a given emission wavelength, essentially measure a product of two factors: the efficiency of exciting electron-hole pairs at a given photon energy; and the probability of those pairs to relax into states from which emission at the chosen wavelength can occur. The excitation spectrum of the dispersed particles while monitoring the emission at 400 nm shows a band extending from 2.5 eV to \sim 4 eV with a maximum near 3.6 eV.

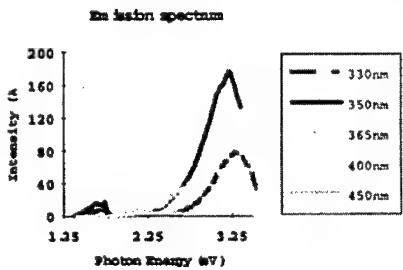


Figure 2

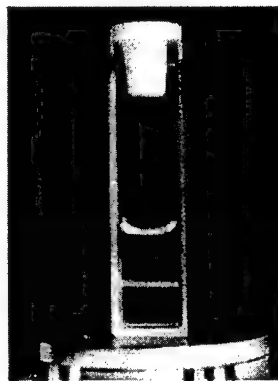


Figure 3

CURRENT-VOLTAGE SPECTRA

Thin films of particles are formed on device quality silicon substrates by gentle evaporation from a volatile particle colloid. The tip of an STM is placed over the silicon particle film. In this two-terminal arrangement, the tip acts as the source electrode, while the substrate acts as the drain electrode. This configuration may be represented by a double barrier model. The particle represents the quantum well, with a narrow vacuum barrier due to a gap between the particle and the tip, and a barrier due to a gap between the particle and the substrate. In the measurement, the tunneling current was set at 1 nA and the biasing voltage at 3V in a constant current mode, giving a tip height of several angstroms. While the voltage of the tip was varied with respect to the (grounded) substrate from -10 to +3 volts in a constant height mode, the tunneling current was recorded as shown in Figure 4a. Figure 4b, the derivative of the I-V curve, clearly shows near regular resonances at a spacing of ~ 0.30 eV for both positive and negative tip biasing. The spectra show that the source-drain current is blocked over a range of ~ 2 Volts, from -1 to +1 Volts. We, therefore, estimate the corresponding capacitance to be $\sim 0.8 \times 10^{-19}$ F. The capacitance of the particles is $C = 2\pi \epsilon d$, where ϵ is the permittivity of silicon. For $d = 1$ nm, and assuming a dielectric constant equal to $\epsilon = 12 \epsilon_0$, we get a capacitance of 6.7×10^{-19} F. The total capacitance C is 7.510^{-19} F. The charging due to a single electron of charge e is therefore $\delta = e^2/C = 0.22$ eV. However, the voltage drop across the source section is the fraction ηV_b where $\eta = C_d/C$. If we associate the 0.8×10^{-19} F with the source branch C_s and the 6.7×10^{-19} F with the capacitance of the drain C_d then $\eta = 0.893$ [8]. Therefore the effective characteristic charging energy is $\delta / \eta = 0.25$ eV, consistent with the measurement.

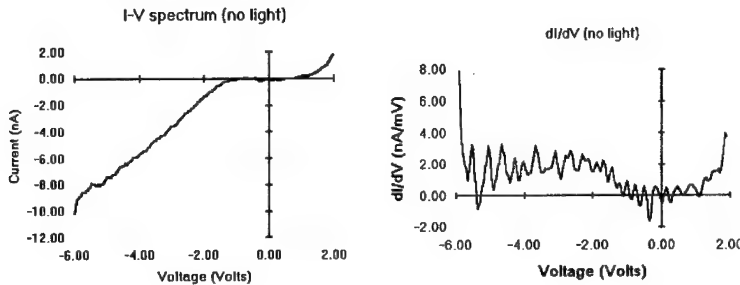


Figure 4

Figure 5, taken with the light from a mercury lamp directed onto the sample, shows quite visibly a regular step structure and a large drop in the magnitude of the tunneling current (by a factor of fifty). The derivative of the I-V curve, shown in Figure 6, shows the progression of the resonance at large negative biasing up to a tip biasing of ~ -2 eV. The light-induced series appears as a modulation of the fine period series, with a period of 1.0 eV. Masked, the fine resonance emerge for biasing above -2 Volts. In addition, upon irradiation, the source blockade widens from ~ 2 to 3.75 Volts. This indicates that the blockade capacitance dropped upon irradiation, by nearly a factor of two, to $\sim 0.4 \times 10^{-19}$ F.

According to a standard theory of confinement, the energy levels of a particle, $E = \hbar^2/8m^*d^2$, gives an energy spacing of $\Delta = 1.03$ eV for $d = 1.1$ nm. Adjusting the energy spacing, we get[8] $\Delta / \eta = 1.07$ eV. Thus we relate the modulation to the opening of tunneling channels as the Fermi energy level of the tip is scanned across the particle's energy levels. The light effect may simply due to hole state generation. Under standard doping levels of $\sim 10^{15} / \text{cm}^3$, as in this sample, particles of 1 nm across contain less than one in a million holes, hence they are no empty levels for the injected electrons. The particles behave as undoped, with the number of electrons in the conduction band extremely small.

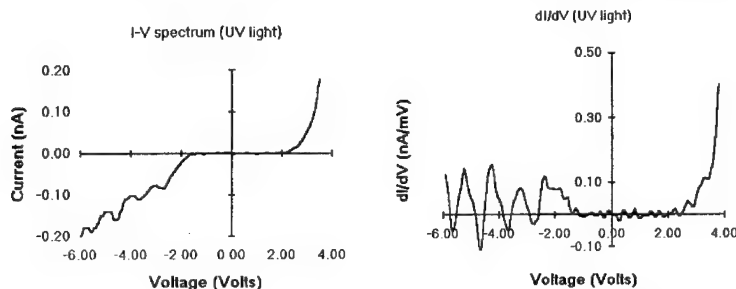


Figure 5

Practical laboratory temperatures are not sufficient to induce holes.

We should note that the charging and modulation resonance reproduce over all sections of the sample. The measurements taken from several spots give the same resonance spacing (to within 10 percent). Thus these I-V spectra confirm the size and uniformity of the particles obtained from TEM and autocorrelation fluctuation spectroscopy, and from differential excitation measurements[9-10].

CONCLUSION

We dispersed silicon into a colloid of ultra-small blue luminescent silicon nano particles ($\sim 1\text{nm}$). The particles are small enough such that the quantum energy spacing is threefold larger than the single electron characteristic charging energy, and such that both dominate the room temperature thermal fluctuation energy by a factor of 10 to 40. We observed, at room temperature, conductance resonance at a spacing of 0.25 to 0.30 eV, consistent with single electron charging. Under light irradiation, we observe conductance resonance modulation, consistent with the particle's quantum energy level spacing. This paves the way for operation of high temperature Si-based single electron devices. Finally, the particles are extremely efficient luminescent material under UV irradiation[11], hence their assembly on device quality silicon crystals provides direct methods for integrating luminescent superlattices into existing microelectronics architecture.

ACKNOWLEDGMENT: We acknowledge the US Department of Energy grant DEFG02-ER45439, and the NIH (RR03155) and the University of Illinois.

REFERENCES

1. Marc Kastner, Physics Today, January, 24 (1993); 1. J. R. Tucker, J. Appl. Phys. **72**, 4399 (1992); D. Ali, and H. Ahmed, Appl. Phys. Lett. **64**, 2119 (1994)
2. L.T. Canham, Appl. Phys. Lett. **57**, 1046 (1990); A. G. Cullis, L. T. Canham, and P. Calcott, J. Appl. Phys. **82**, 909 (1997)
3. D. Andsager, J. Hilliard, J. M. Hetrick, L. H. AbuHassan, M. Plisch, and M. H. Nayfeh, J. Appl. Phys. **74**, 4783 (1993)
4. Z. Yamani, H. Thompson, L. AbuHassan, and M. H. Nayfeh Appl. Phys. Lett. **70**, 3404 (1997); J. Therrien, G. Belomoin, and M. H. Nayfeh, unpublished
5. J. Heinrich, C. Curtis, G. Credo, K. Kavanagh, and M. Sailor, Science **255**, 66 (1992)
6. Z. Yamani, S. Ashhab, A. Nayfeh and M. H. Nayfeh, J. Appl. Phys. **83**, 3929 (1998).
7. O Ackakir, J. Therrien, G. Belomoin, N. Barry, J. Muller, E. Gratton, and M. Nayfeh, (unpublished).
8. D. Averin, A. N. Korotkov, and K. K. Likharev, Phys. Rev. B **44**, 6199 (1991)
9. Z. Yamani , N. Rigakis, and M. H. Nayfeh, Appl. Phys Lett. **72**, 2556 (1998).
10. Z. Yamani, O. Gurdal, A. Alaqil, and M. Nayfeh, J. Appl. Phys. **85**, 8050 (1999)
11. M. Nayfeh, O. Akcakir, J. Therrien, Z. Yamani, N. Barry, W. Yu, and E. Gratton, Appl. Phys. Lett. (In Press: Dec 27, 1999)

UNIMOLECULAR ELECTRICAL RECTIFICATION DOWN TO 105 K, AND SPECTROSCOPY OF HEXADECYLQUINOLINIUM TRICYANOQUINODIMETHANIDE

R. M. METZGER

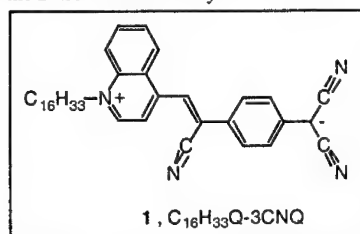
Laboratory for Molecular Electronics, Chemistry Department, University of Alabama, Tuscaloosa, AL 35487-0336, USA, rmetzger@bama.ua.edu

ABSTRACT

A Langmuir-Blodgett monolayer of γ -(n-hexadecyl)quinolinium tricyanoquinodimethanide, $C_{16}H_{33}Q-3CNQ$ (1), sandwiched between Al electrodes, shows asymmetric DC electrical conductivity between 370 K and 105 K. The enhanced forward current is attributable to rectification of electrical current by a single molecule, and is explained by an electronic transition from a high-moment zwitterionic ground state to a low-moment undissociated first excited state.

INTRODUCTION

Aviram and Ratner (AR) proposed in 1974 that a single, asymmetrical, D- σ -A molecule should be a rectifier of electrical current, because the electrical conductivity in one direction through the molecule is much larger than the conductivity in the opposite direction [1]. This would be because the undissociated ground state $D^0-\sigma-A^0$ is close to the first zwitterionic excited state $D^+-\sigma-A^-$, but very far from the oppositely charged zwitterionic excited state $D^--\sigma-A^+$. Indeed, a good one-electron donor end D would be oxidized (relatively) easily into the cation D^+ , and a one-electron acceptor A would be reduced easily to the anion A^- , while the oppositely charged ions D^+ and A^- would lie several eV above the D^+ and A^- states [1]. A saturated covalent bridge σ would separate the D from the A moiety.



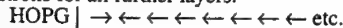
Many D- σ -A molecules that form LB films were synthesized, but, with primitive measurement techniques, rectification was not found [2-4]. Sambles and coworkers developed better techniques, and found asymmetric currents in a sandwich "Pt | LB multilayer of dodecyloxyphenyl carbamate of bromohydroxyethoxytetracyanoquinodimethane | Mg | Ag" [5], but a Schottky barrier could also form in this system [6]. Ashwell introduced a new family of ground-state zwitterionic molecules of the type $D^+-\pi-A^-$, such as picolytricyanoquinodimethane [7], and γ -(n-hexadecyl)quinolinium tricyanoquinodimethanide, $C_{16}H_{33}Q-3CNQ$ (1) [8]. Z-type Langmuir-Blodgett multilayers of 1 have a large second-order nonlinear optical susceptibility $\chi^{(2)}_{zzz} = 180 \text{ pm V}^{-1}$ [9]. Sambles and coworkers, using dissimilar metal electrodes, found that the sandwich "Au wire | Ga/In eutectic | Pt | LB multilayer of 1 | Mg | Ag | Ga/In eutectic | Au wire" is a multilayer rectifier [10,11].

After some preliminary work [12,13] we found electrical rectification through a monolayer of 1 by macroscopic methods in the sandwich "Au wire | Ga/In eutectic | Al pad | monolayer of 1 | Al | Ga/In eutectic | Au wire", and also by nanoscopic methods (STM) [14]; we extended the macroscopic measurements to the range 370 K to 105 K [15], and discussed the junctions with anomalous electrical behavior [16]. We established that 1 is a ground-state zwitterion of the type $D^+-\pi-A^-$, with a large dipole moment (43 ± 8 Debyes) [14], whose first excited state has lower polarity $D^0-\pi-A^0$ (estimated moment 3 to 9 Debyes) [17]; the two states are coupled by a strong intervalence band [14,17]. The molecule can be reduced reversibly once [14], but oxidizes irreversibly [14]; its behavior seems different from that predicted by AR for D- σ -A molecules [1], but the AR proposal was easily modified for a molecule with a $D^+-\pi-A^-$ ground state [14]. Additional theoretical calculations have been carried out [18]. These results have been reviewed in other venues [19-27], but merit a fresh look here.

MOLECULAR AND MONOLAYER PROPERTIES

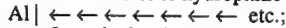
A reliable synthesis of **1** is from N-cetyl-lepidinium tosylate and a 2-fold excess of the lithium salt of TCNQ radical anion, in dry DMSO solution with added pyridine [14]. The NMR spectrum of **1** suggests a dipolar ground state [14]. The dipole moment of **1** in CH_2Cl_2 at infinite dilution is $43 \pm 8 \text{ D}$, which is 90% of the value expected for a positive charge (+1) on the quinolinium nitrogen atom and a negative charge (-1) on the dicyanomethylene central carbon [14]. The blue or green intervalence transition (IVT) in solution is strongly hypsochromic, which indicates a more polar ground state than excited state. From this hypsochromism, an excited-state dipole moment of 3 to 9 D was estimated [17]. The cyclic voltammogram of **1** exhibits a one-electron quasi-reversible reduction ($E_{1/2} = -0.513 \text{ V vs SCE}$), making the molecule into an electron acceptor as weak as benzoquinone [14].

The Π -A isotherm of **1**, measured under a green safelight, shows a collapse point at $50 \text{ \AA}^2 \text{ molecule}^{-1}$ and 34 mN m^{-1} ; this isotherm is moderately temperature-dependent [13,14]. Monolayers and multilayers of **1** were transferred to solid substrates at 15 mm/min at a film pressure of 20 mN/m : **1** first transfers on the downstroke onto hydrophobic HOPG, then on the upstroke for all further layers:



Here the arrow \rightarrow indicates the rough molecular orientation; it points from the hexadecyl tail and the quinolinium ring D^+ (tail of arrow) towards the dicyanomethylene head of A^- (head of arrow). The first monolayer adheres with the hexadecyl tail next to HOPG (X-type orientation), while the other layers have Z-type orientation (tails away from HOPG). The transfer ratios were 50 % for the first layer, and from 50 % to 100 % for the Z-type layers [14].

The film transfer to hydrophilic Al is Z-type for all layers:



the transfer ratio for the first layer is now over 90 % [14].

The IVT band maximum is at 565 nm in LB monolayers [17] or 570 nm in LB multilayers [14]. A grazing-angle Fourier transform infrared spectrum for a monolayer of **1** on Al shows absorbances at 2850 cm^{-1} (symmetric C-H), 2920 cm^{-1} (asymmetric $-\text{CH}_2-$), 2139 cm^{-1} ($-\text{C}\equiv\text{N}$) and 2175 cm^{-1} ($-\text{C}\equiv\text{N}$), indicating that the cyano groups and the methylene groups do not lie in the plane of monolayer [14]. The X-ray photoelectron spectrum of an LB multilayer shows a N 1s spectrum that is the superposition of three peaks, whose chemical shifts are characteristic of N^+ (quinolinium N), of N^0 (cyano N), and of N^- (dicyanomethylene nitrogens), as expected [17]. Simultaneous EPR and CV, at the point where the molecule becomes a stable radical anion, shows a hyperfine structure that can be fit very well to spin densities localized on the 3CNQ part of the molecule, confirming the semiempirical molecular orbital calculations for the LUMO of **1** [17].

Thus **1** is a molecule with a large reduction in dipole moment in the transition from ground to excited state, with an electronically allowed and intense band linking the two states.

MACROSCOPIC CONDUCTIVITY OF LB FILMS

Macroscopic "metal | organic | metal" sandwiches were studied [14-16]. An Edwards 306A evaporator, with a liquid nitrogen-cooled substrate holder and a multiple-source evaporator, was used to form the sandwiches. The I-V curves were measured using both a PAR 270 potentiostat and also a Gateway 2000 microcomputer-controlled AC and DC conductivity measuring system (Hewlett-Packard Models 3245A and 3457A).

The glass or quartz or silicon substrates were covered by an Al layer, $25 \text{ mm} \times 75 \text{ mm} \times 100 \text{ nm}$ thick, then LB monolayer or multilayer films were transferred under a green safelight, then the sample was dried for 2 days in a vacuum desiccator with P_2O_5 . Twelve cylindrical "pads" of Al (4 each of areas 2.8, 4.5, and 6.6 mm^2 , either 100 nm thick or 300 nm thick) were finally deposited per microscope slide, atop the organic layer, with the substrate cooled to 77 K , to form the sandwiches as shown for monolayers (Fig. 1a) and multilayers.

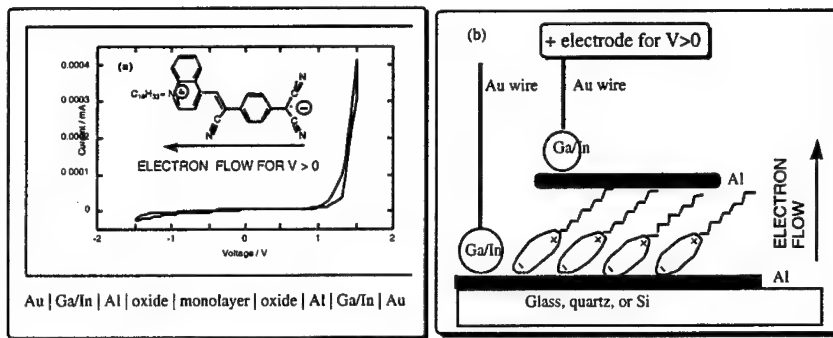


Fig. 1. (a) Current-voltage plot at room temperature for the sandwich "Au wire | Ga/In eutectic | Al substrate (with oxide) | LB monolayer of **1** | Al pad (with oxide) | Ga/In eutectic | Au wire", with arrow indicating the direction of enhanced forward current through the molecule. Rectification ratio $RR = (\text{current at } 1.5 \text{ V})/(\text{current at } -1.5 \text{ V}) = 26$, but RR becomes smaller in later IV cycles [14]. (b) Orientation of the LB monolayer on the glass, quartz, or Si substrate. The electrode (+) for positive bias, and the direction of "easy" electron flow for $V > 0$ are marked. The indicated slant ($48 \pm 5^\circ$) is determined from the ratio of the measured monolayer thickness (23 Å), to the maximum possible calculated molecular length (30 Å) [14].

Contact to the Al electrodes was made with a Ga/In eutectic. The electrodes (Al) are symmetrical, but covered by defect-rich Al_2O_3 layers. When well-dried Y-type (centrosymmetric) multilayers of arachidic acid were studied, no IV asymmetries were found. A very asymmetric I-V curve was found for a 4-monolayer film of **1**; reversing the electrodes reversed the asymmetry [14]. A similarly asymmetric I-V curve occurred when a Mg layer was deposited atop the organic layer below the Al pad [14]. For monolayers, 17 out of 39 pads were short circuits, either because of monolayer defects, or because the Ga/In eutectic created new defects during attachment. The 22 "good" junctions had DC resistances from 1 to 400 MΩ [14], [16]; of these, 4 exhibited rectifying behavior. Fig. 1(a) shows a typical rectification curve. Above a threshold voltage V_t , the monolayer shows larger currents for positive bias than for negative bias. This V_t varies from junction to junction in the range $V_t = 0.8$ to 1.3 V [14]. As the measurement cycle is repeated, RR drops steadily, and disappears after 4 to 6 cycles. Under the intense electric fields ($1.5 \text{ V}/23 \text{ \AA} = 0.65 \text{ GV m}^{-1}$), the physisorbed dipolar molecules probably re-orient [14]. The results on both monolayers and multilayers [14] show that the electrons preferentially flow by IVT from 3CNQ (A^-) to quinolinium (D^+). The enhanced current at 1.5 V in Fig. 1 corresponds to only 0.33 electrons molecule $^{-1}$ s $^{-1}$ [14].

Work in the temperature range 370 K - 105 K showed that the rectification ratio was not a function of temperature. Fig. 2 shows the current asymmetry at 105 K [15].

One goal was to extend such measurements to 4.2 K. However, the design of Fig. 1(b) was very susceptible to vibrations, differences in thermal expansivities, and the frequent detachment of the contacts at low temperatures. When the Ga/In eutectic wetted the Al pad above the LB monolayer, the pad would detach mechanically from the monolayer; if no wetting occurred, there was a 100 kΩ series resistance between the Au wires, presumably at the Ga / oxide / Al interfaces [15]. A new design (Fig. 3) moved the point where the Au wires were connected away from directly above the monolayer [28]. This was obtained by evaporating a 200 nm thick layer of Al onto a glass microscope slide, then carefully polishing the surface chemically in dilute aqueous NaOH, until, on one side of the substrate, the glass surface was exposed [28]. The resulting aluminum surface should have a slope going up from the substrate, and no sharp discontinuities. The IV curve measured at room temperature with this new arrangement and Ag paste contacts, is

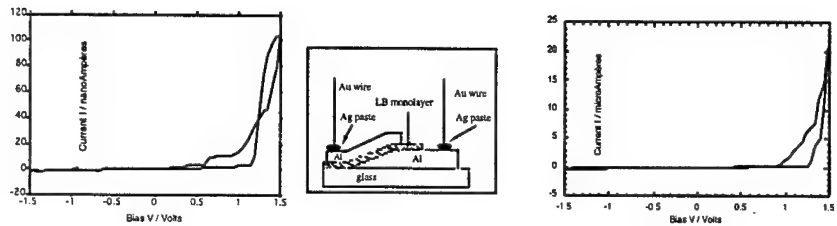


Fig. 2. Current-voltage plot at 105 K for the sandwich "Au wire | Ga/In eutectic | Al substrate+oxide | LB monolayer of 1 | Al pad (with oxide) | Ga/In eutectic | Au wire" [15].

Fig. 3. Improved sloped Al substrate for placing the top electrode contact to the left, rather than above the bottom Al [28].

Fig. 4. Current-voltage plot at room temperature using the improved structure shown in Fig. 3; RR=53 [28].

shown in Fig. 4: much larger currents were recorded [28]. Now the RR is 53, and the enhanced current through the monolayer at 1.5 V has increased to 35 electrons molecule⁻¹ s⁻¹ [28].

NANOSCOPIC STRUCTURE AND CONDUCTIVITY OF LB FILMS

In a low-current STM (Digital Instruments Nanoscope III) an LB monolayer of **1** showed a molecular image with low resolution and a repeat distance of 6 Å × 12 Å (Fig. 5) [14].

Multilayers of **1** on HOPG were studied using a Pt/Ir nanotip at room temperature in air by STM and STS [13]. Asymmetries were seen in the I-V plot in a 15-layer film (Fig. 6) [13], in agreement with the I-V characteristics of macroscopic films, with IVT between LB layers 2 through 15. The electrons must somehow jump between adjacent monolayers, and also get across the poorly transferred first monolayer (which is oriented the "wrong way", compared with the other 14 layers) [13].

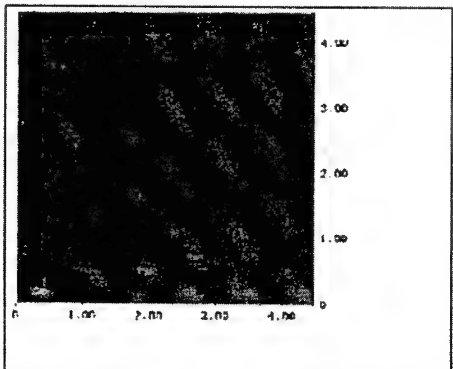


Fig. 5. STM of a LB monolayer of **1** on HOPG with Pt/Ir tip. Scan 4.5 nm × 4.5 nm, Z-range=2.3 pA, bias = -316 mV; setpoint current = 3.2 pA [14].

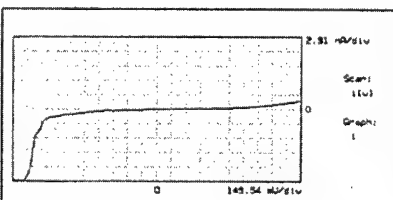


Fig. 6. STS I-V curve for an LB film of 15 Z-type monolayers of **1** on HOPG, with Pt/Ir tip. The higher current for V < -1.35 Volt corresponds to electron flow from HOPG through the molecules to the Pt/Ir tip [13].

An STS spectrum for a partial monolayer of **1** adhering with its alkyl tail on HOPG shows a slightly higher current at positive bias, in the expected direction [14].

DISCUSSION

The AR model of rectification [1] places a single molecule $D-\sigma-A$ (D = good electron donor, A = good electron acceptor, σ = covalent linkage between D and A) between two macroscopic metal electrodes M_1 and M_2 . Under "forward bias" an electron is transferred from M_2 to M_1 in two steps: $M_1 | D-\sigma-A | M_2 \rightarrow M_1^- | D^+-\sigma-A^- | M_2^+ \rightarrow M_1^- | D-\sigma-A | M_2^+$, where the first step involves elastic tunneling (ET) at resonance between the metal electrodes and the first excited state of the molecule $D^+-\sigma-A$ (maybe 1 to 2 eV above the ground state), and the second step is inelastic down-hill tunneling to the ground state $D-\sigma-A$ by IVT. The AR model can be adapted to a ground-state zwitterion $D^+-\pi-A^-$, whose first excited state is $D^0-\pi-A^0$, by assuming first IVT, then ET to the metal electrodes: $M_1 | D^+-\pi-A^- | M_2 \rightarrow M_1 | D^0-\pi-A^0 | M_2 \rightarrow M_1^- | D^+-\pi-A^- | M_2^+$ [14]. However, since **1** is not a molecule whose components have low ionization potentials (the molecule decomposes upon oxidation in solution [14]) or high electron affinity (its reversible reduction puts it on a par with p-benzoquinone), therefore one should probably consider its mechanism of action as that linking a state with high dipole moment with one with low dipole moment, through an allowed electronic transition. Another zwitterionic molecule, whose dipole moment was in the plane of the monolayer, instead of normal to it, and which did not exhibit hypsochromism, did not rectify [29]. Another molecule with an unpromising structure did, however, rectify [30].

There are other unsolved issues.

The long alkyl chain in **1**, which is needed to make LB films, has an unknown role in the mechanism of rectification.

Further, it is well known that Al is a "valve metal": after thick barrier oxide films are grown over Al in basic solutions, the $Al | Al_2O_3$ couple is a rectifier. Since the oxide is present on the Al in these studies, but is defective, and since "blank tests" with centrosymmetric arachidic acid show no rectification, it is very likely that the oxide, where present, is a barrier to conduction, and that the enhanced current in Figs. 2 and 4 occurs in the gaps between where the oxide is absent. This may be why the macroscopically measured currents reported here are only between 0.33 and 35 electrons molecule $^{-1}$ s $^{-1}$ [14,28], while STM currents are typically 1 nA molecule $^{-1}$ = 6×10^9 electrons molecule $^{-1}$ s $^{-1}$ [14].

Finally, one can be sure that the current really does go through molecule **1** only if one observes some spectroscopic signature of this process: this is why it is so important to proceed with 4.2 K studies (to detect inelastic electron tunneling through the chemical bonds) or low-temperature ultra-high-vacuum STM.

CONCLUSIONS

A monolayer of molecule **1** rectifies by intramolecular tunneling; monolayers and multilayers of **1** rectify both as macroscopic films (using Al for both electrodes) and nanoscopically, by STM.

ACKNOWLEDGMENTS

Thanks are due to the many coworkers who carried out most of the work.

REFERENCES

1. A. Aviram and M. A. Ratner, *Chem. Phys. Lett.* **29**: 277 (1974).
2. R. M. Metzger and C. A. Panetta, *New J. Chem.* **15**: 209 (1991).
3. R. M. Metzger, In *Molecular and Biomolecular Electronics*, R. R. Birge, Ed., ACS Adv. in Chem. Ser. **240** (American Chemical Society, Washington, DC 1994) p. 81.
4. R. M. Metzger, *Mater. Sci. & Engrg. C3*: 277 (1995).

5. N. J. Geddes, J. R. Sambles, D. J. Jarvis, W. G. Parker and D. J. Sandman, *Appl. Phys. Lett.* **56**: 1916 (1990).
6. N. J. Geddes, J. R. Sambles, D. J. Jarvis, W. G. Parker and D. J. Sandman, *J. Appl. Phys.* **71**: 756 (1992).
7. R. M. Metzger, N. E. Heimer and G. J. Ashwell, *Mol. Cryst. Liq. Cryst.* **107**: 133 (1984).
8. G. J. Ashwell, M. Szablewski and A. P. Kuczynski, in R. M. Metzger, P. Day, and G. C. Papavassiliou, Eds., Lower-Dimensional Systems and Molecular Electronics, NATO ASI Series (Plenum, New York, 1991) **B248**, p. 647.
9. G. J. Ashwell, in G. J. Ashwell and D. Bloor, Eds. Organic Materials for Nonlinear Optics, (Royal Soc. of Chem., Cambridge, 1993), p. 31.
10. G. J. Ashwell, J. R. Sambles, A. S. Martin, W. G. Parker and M. Szablewski, *J. Chem. Soc. Chem. Comm.* 1374 (1990).
11. A. S. Martin, J. R. Sambles and G. J. Ashwell, *Phys. Rev. Lett.* **70**: 218 (1993).
12. X.-L. Wu, M. Shamsuzzoha, R. M. Metzger and G. J. Ashwell, *Synth. Metals* **55-57**: 3836 (1993).
13. R. M. Metzger, H. Tachibana, X. Wu, U. Höpfner, B. Chen, M. V. Lakshmikantham and M. P. Cava, *Synth. Metals* **85**: 1359 (1997).
14. R. M. Metzger, B. Chen, U. Höpfner, M. V. Lakshmikantham, D. Vuillaume, T. Kawai, X. Wu, H. Tachibana, T. V. Hughes, H. Sakurai, J. W. Baldwin, C. Hosch, M. P. Cava, L. Brehmer and G. J. Ashwell, *J. Am. Chem. Soc.* **119**: 10455 (1997).
15. B. Chen and R. M. Metzger, *J. Phys. Chem.* **B103**: 4447 (1999).
16. D. Vuillaume, B. Chen, and R. M. Metzger, *Langmuir* **15**: 4011 (1999).
17. J. W. Baldwin, B. Chen, S. C. Street, V. V. Konovalov, H. Sakurai, T. V. Hughes, C. S. Simpson, M. V. Lakshmikantham, M. P. Cava, L. D. Kispert, and R. M. Metzger, *J. Phys. Chem.* **B103**: 4269 (1999).
18. O. Kwon, M. L. McKee, and R. M. Metzger, *Chem. Phys. Letters* **313**: 321 (1999).
19. R. M. Metzger, B. Chen, D. Vuillaume, U. Höpfner, J. W. Baldwin, T. Kawai, H. Tachibana, H. Sakurai, M. V. Lakshmikantham, and M. P. Cava, *MRS Proceedings* **488**: 335 (1998).
20. R. M. Metzger, B. Chen, D. Vuillaume, M. V. Lakshmikantham, U. Höpfner, T. Kawai, J. W. Baldwin, X. Wu, H. Tachibana, H. Sakurai, and M. P. Cava, *Thin Solid Films* **327-329**: 326 (1998).
21. R. M. Metzger and M. P. Cava, *Ann. N. Y. Acad. Sci.* **852**: 95 (1998).
22. R. M. Metzger, *Adv. Mater. Optics & Electronics* **8**: 229 (1998).
23. R. M. Metzger, *Mol. Cryst. Liq. Cryst.*, accepted and in press.
24. R. M. Metzger, *J. Materials Chem.* **9**: 2027 (1999).
25. R. M. Metzger, *J. Materials Chem.*, accepted and in press.
26. R. M. Metzger, *Synth. Metals*, accepted and in press.
27. R. M. Metzger, *Acc. Chem. Res.* **32**: 950 (1999).
28. B. Chen, Ph.D. dissertation, University of Alabama (1999).
29. T. V. Hughes, B. Mokijewski, B. Chen, M. V. Lakshmikantham, M. P. Cava, and R. M. Metzger, *Langmuir* **15**: 6295 (1999).
30. A. C. Brady, B. Hodder, A. S. Martin, J. R. Sambles, C. P. Ewels, R. Jones, P. R. Briddon, A. M. Musa, C. A. Panetta, and D. L. Mattern, *J. Mater. Chem.* **9**: 2271 (1999).

Fabrication Methods for Au Nanocluster Devices

**A.W. Snow, M.G. Ancona, W. Kruppa, D. Park, J.B. Boos and
G.G. Jernigan**

Naval Research Laboratory
Washington, DC 20375-5000 USA

ABSTRACT

The deposition chemistry of hexanethiol-stabilized gold nanoclusters self-assembled on Au and SiO₂ surfaces by reaction with a series of α,ω -alkanedithiols is studied using X-ray photoelectron spectroscopy and electrical measurements. Testing of micron-scale devices shows that high conductivity is achieved only for a narrow range of dithiols and with a sharp efficiency threshold. Nanoscale devices exhibit similar behavior though with much evidence of "granularity" in the deposition.

INTRODUCTION

Gold nanoclusters provide a combination of dimensionality, physics and chemistry that makes them attractive as a basis for nanometer-scale electronic devices. As a number of researchers have shown, gold nanoclusters with a variety of sizes are easily synthesized and stored. Much less well understood is the ways in which these clusters can be manipulated and deposited in a selective manner. From an electronic standpoint, smaller clusters (~2 nm in diameter) are of the most interest because they are small enough to exhibit Coulomb blockade effects at room temperature in an AFM configuration [1] yet still have enough atoms (~250) to be essentially metallic. In such a system gating effects, which have been observed at least for larger clusters [2], could be the basis of an electronics technology. Our general approach to nanoscale electronics is to develop device configurations that can exploit the Coulomb blockade of the clusters so as to achieve useful electronic functions at room temperature. To do this and to allow interfacing with conventional microelectronics we make hybrid devices formed by cluster depositions on e-beam defined nanostructures [3]. For the approach to be successful a way must be found to bridge the crucial gap between our ability to define features lithographically down to 10-15 nm and our ability to synthesize and manipulate molecules/clusters with attractive electronic properties that is limited to dimensions of about 2 nm [4]. We aim to do this by developing regionally-controlled cluster self-assembly techniques. Toward this end, in this report we discuss some aspects of the gold cluster -- alkanedithiol self-assembly chemistry that are critical to making the deposition work. The diagnostics used in this study are X-ray photoelectron spectroscopy (XPS) and electrical transport measurements through gold clusters deposited on lithographically-defined electrodes of various sizes.

EXPERIMENTAL DETAILS

The stabilized gold clusters we have investigated consist of gold cores encapsulated by a monolayer shell of alkanethiol or phenethylthiol. They are synthesized by the reduction of HAuCl₄ with NaBH₄ in the presence of the alkanethiol or phenethylthiol [5]. The diameter of the core is controlled by the gold to thiol stoichiometry and the

thickness of the shell is determined by selection of the hydrocarbon portion of the thiol [6]. We have synthesized a variety of these clusters where the core diameter varies from 1.3 to 5.0 nm and the shell thickness varies from that corresponding to butanethiol (0.4 nm) to that corresponding to hexadecanethiol (1.0 nm) [7]. For the present work we focus on two of these clusters: The first is designated Au:C6(1:1) and was prepared from a 1:1 HAuCl₄:hexanethiol stoichiometry, and the second is designated Au:C2C6(1:1) and was analogously prepared from HAuCl₄ and phenethylthiol.

To characterize the deposition chemistry of these clusters on SiO₂ and on Au we have used XPS and electrical transport measurements. The XPS was performed following depositions on thermally-oxidized Si substrates either with or without a gold coating. The electrical measurements were instead made following depositions on two types of substrates with pre-patterned electrodes, one of micron scale, the other of nanometer scale. The first substrate is a commercially-available gold interdigitated electrode array deposited on a quartz substrate with a chromium underlay (MSI P/N 302 device, Microsensor Systems, Inc.). It consists of 50 finger pairs with a spacing of 15 μm, a finger width of 15 μm, a finger thickness of 150 nm and an effective total width of 4800 μm. The second substrate was fabricated in-house using standard e-beam lithography with lift-off to create a pattern of Ti/Au finger electrodes on an Si/SiO₂/Si₃N₄ substrate. These electrodes were single finger pairs with a gap spacing ranging from 12 nm to 160 nm, a finger width of 50 nm and a finger thickness of 30 nm. An SEM micrograph of one of the smaller nanofinger devices is shown in Fig. 1. The nitride layer, used to reduce leakage currents, was deposited using plasma-assisted CVD followed by a dry oxidation at 900°C. The latter results in the exposed

upper surface being SiO₂ and so, from the point-of-view of surface chemistry, it can be presumed to be not much different from the quartz substrate used in the micron-scale devices.

The self-assembly chemistry involves a substitution reaction between a thiol functional group anchored to the electrode or substrate surface and a monothiol- stabilized gold cluster in solution as depicted in Fig. 2. The initial

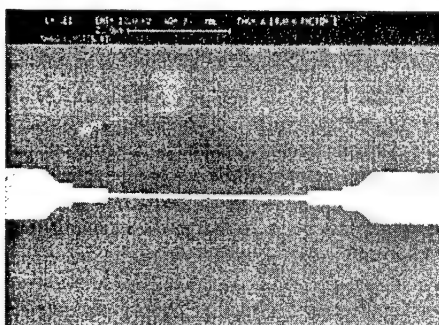


Fig. 1. SEM micrograph of the nanoscale finger electrode design.

alkanethiol functionalization of the substrate is accomplished using an α,ω -alkanedithiol for a gold electrode surface and/or a trimethoxysilane-terminated alkanethiol for the quartz surface. Next, gold clusters are self-assembled on the functionalized surfaces via a substitution

reaction. Ideally, a continuous layer of clusters would be deposited. In practice, we observe a partial coverage by the clusters.

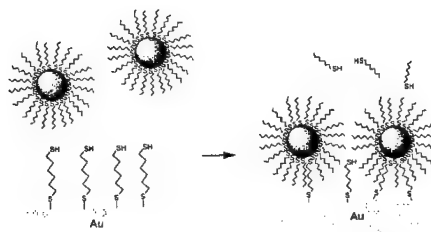


Fig. 2. Schematic representation of the gold cluster alkanethiol ligand substitution reaction in the self-assembly deposition process.

To obtain a more complete coverage, the initial cluster deposition is activated by treatment with the alkanedithiol for a second self-assembled cluster deposition. This two step cycle can be repeated many times to deposit a controlled quantity of clusters. In devising a deposition procedure that will be efficient and that will produce a deposition with useful electrical characteristics, the issues of critical importance are the thickness of the ligand shell, the chain length of the intercluster linking dithiol and the deposition conditions. The ligand shell functions as an insulator between adjacent clusters, and its thickness is a major determinant of the conductivity of a layer of clusters. We have observed the electrical conductivity to vary 6 orders in magnitude as the shell thickness varies from that corresponding to butanethiol to that corresponding to hexadecanethiol. The ligand shell thickness also has a very strong influence on the cluster's stability and on the efficiency with which it undergoes the alkanethiol ligand substitution reaction. While the butanethiol shell is very thin and very efficient at undergoing the thiol ligand substitution reaction, it is somewhat unstable to irreversible aggregation and nonspecific deposition particularly at temperatures approaching 100C. We have found that the hexanethiol shell has much better stability and acceptable ligand substitution reaction efficiency without becoming too strongly insulating to neighboring clusters. This is our rationale for selecting the Au:C6(1:1). The rationale for using Au:C2C6(1:1) is similar. The chain length of the interconnecting thiol is determined by at least two factors: (1) the need to bridge between two adjacent coated clusters and (2) the effect on the electrical resistance between adjacent clusters. Our findings from Langmuir-Blodgett measurements indicate that the thickness of the shell is much less than the extended chain length of the alkanethiol ligand surrounding the cluster [6]. We believe that the alkanethiol attached to the cluster surface has a random coil conformation and that the alkanedithiol must penetrate this shell to the core surface to displace the monofunctional ligand.

The deposition procedure for the 15 μ m electrode devices consists of plasma cleaning the surface, immersing the sample in 1.0% w/w alkanedithiol/CHCl₃, rinsing, immersing in 5% w/w (3-mercaptopropyl) trimethoxysilane/CHCl₃, rinsing, immersing again in 1.0% w/w alkanedithiol/ CHCl₃, rinsing and, finally, immersing in 0.50% w/w Au:C6(1:1)/ CHCl₃. On the first cycle the immersion times are 15 min. Subsequent depositions are conducted in a cycle of 2 min immersions in the 1.0% w/w alkanedithiol/CHCl₃ and in the 0.50% w/w Au:C6(1:1)/CHCl₃. DC electric current measurements were made after each deposition cycle. The deposition procedure for the nanometer scale electrode was identical except that a 10 min immersion in a boiling

$\text{H}_2\text{O}_2:\text{NH}_4\text{OH}:\text{H}_2\text{O}$ solution (1:1:3 by volume) was used to clean the electrode surface. In experiments on both types of electrodes the immersion in the 5% w/w (3-mercaptopropyl) trimethoxysilane/CHCl₃ solution was not always performed.

RESULTS AND DISCUSSION

Because of space limitations we discuss here only the electrical characterization results. Results from the XPS measurements will be presented at the meeting and discussed in detail elsewhere.

To determine an optimum alkanedithiol chain length, the micron-scale electrode substrates were used and self-assembly experiments were conducted with the dithiols listed in Table I. The current levels after each of 6 successive deposition cycles are listed in the table and two conclusions seem evident. First, the octanedithiol and the p-xylyldithiol cluster linkers, both involving 8 carbon atom chain lengths, maximize the electrical current at least after the initial phase. This observation continues to hold with more deposition cycles out to at least 20 at which point the 8 carbon dithiols exhibit about 6 times the current seen in the shorter (6 carbon) and longer (9 and 12 carbon) dithiols. It is striking that the optimum should be so narrowly centered on an alkanedithiol chain length of 8 carbon atoms. We speculate that the shorter dithiols are too short to provide an efficient bridging reaction between adjacent coated clusters and longer chains result in greater distances between bonded clusters and therefore reduced tunneling currents. The second conclusion concerns the early depositions. We observe that in the initial phase the alkanedithiol substitution self-assembly reaction is much more efficient when the alkanedithiol chain length is at least 9. That is, both the 9 and 12 carbon

Table I. Effect of alkanedithiol structure on electrical current measured following 6 successive deposition cycles of the Au:C6(1:1) clusters on the 15 μm gap electrode.

Dithiol	Current in pA					
	After 1 cycle	After 2 cycles	After 3 cycles	After 4 cycles	After 5 cycles	After 6 cycles
HS(CH ₂) ₆ SH	0	0	6	31	48	110
HS(CH ₂) ₈ SH	1	32	169	1240	4030	5750
HS(CH ₂) ₂ CH ₄ (CH ₂) ₂ SH	24	725	1930	3700	5700	7750
HS(CH ₂) ₉ SH	1040	985	1030	1260	1900	2300
HS(CH ₂) ₁₂ SH	780	710	685	775	822	1390

alkanedithiols display significant current on the first deposition cycle. One possible explanation for this behaviour, supported by the nanoscale measurements, is that the longer chain molecules show a greater level of non-specific adsorption to the SiO₂ substrate.

The XPS and the micron-scale device measurements are effective tools for characterizing the deposition chemistry and transport properties in an *area-averaged* sense. But of course if we are to create nanometer-scale electronic devices using this chemistry it is important to know whether the chemistry and the transport operate in

the same way at the nanoscale. We have performed a number of preliminary experiments on the nanometer-sized electrode substrates in an attempt to address this question. In this paper, however, only one such experiment is discussed.

We consider an experiment in which no initial exposure to silanethiol was performed to functionalize the SiO_2 surface. Ideally one would expect that in this case the clusters would selectively self-assemble onto the gold electrodes but not onto the SiO_2 surfaces. With repeated depositions layers of clusters would build up on the electrodes ultimately leading to a bridging of the gap and a turn-on in electrical conduction. Narrower gaps would bridge first and, based on this picture, one would expect our narrowest gaps to take at least 5 immersion cycles before bridging could occur. This expected behavior is *not* observed. Instead pre-mature bridging is seen and the behavior is reminiscent of that seen in the micron-scale devices. On average, as in the larger devices, when a 8 carbon dithiol is used no conduction is seen until the third immersion cycle, but when a 9 carbon dithiol is used, appreciable levels of conduction are seen after the first immersion. This pre-mature bridging suggests that non-specific adsorption of clusters on the SiO_2 surface is occurring. Since the clusters are the essentially identical, this finding indicates that the different dithiols vary in their adsorptive properties. Again these are results for the *average* device. When one looks at individual devices that are nominally the same one sees considerable variation. This suggests that the non-specific adsorption is occurring in a quasi-random fashion and that the device-to-device variations are a manifestation of the "granularity" in the underlying deposition process.

CONCLUSIONS

X-ray photoelectron spectroscopy and electrical measurements have been used to examine the deposition chemistry of hexanethiol-stabilized gold nanoclusters self-assembled on Au and SiO_2 surfaces by reaction with α,ω -alkanedithiols. The deposition chemistry is found to be efficient in terms of current measured only over a narrow range of chain lengths of the dithiol linker molecules. Experiments on nanodevices indicates that this deposition process is non-uniform at a nanometer scale.

REFERENCES

1. R.P. Andres, T. Bein, M. Dorogi, S. Feng, J.I. Henderson, C.P. Kubiak, W. Mahoney, R.G. Osifchin and R. Reifenberger, *Science*, **272**, 1323-1325 (1996); R.P. Andres, S. Datta, M. Dorogi, J. Gomez, J.I. Henderson, D.B. Janes, V.R. Kolagunta, C.P. Kubiak, W. Mahoney, R.F. Osifchen, R. Reifenberger, M.P. Samanta and W. Tian, *J. Vac. Sci. Technol.*, **A14**, 1178-1183 (1996); R.S. Ingram, M.J. Hostetler, R.W. Murray, T.G. Schaaff, J.T. Khouri, R.L. Whetten, T.P. Bigioni, D.K. Guthrie, and P.N. First, *J. Am. Chem. Soc.*, **119**, 9279-9280 (1997); T. Sato and H. Ahmed, *Appl. Phys. Lett.*, **70**, 2759-2761 (1997).
2. T. Sato, H. Ahmed, D. Brown, and B.F.G. Johnson, *J. Appl. Phys.*, **82**, 696-701 (1997).
3. A. Ulman, *An Introduction to Ultrathin Organic Films from Langmuir-Blodgett to Self-Assembly* (Academic Press, 1991) pp. 416-423.
4. D.L. Allara, T.D. Dunbar, P.S. Weiss, L.A. Bumm, M.T. Cygan, J.M. Tour, W.A. Reinerth, Y. Yao, M. Kozaki and L. Jones, II, *Annals N.Y. Acad. Sci.*, **852**, 348-370 (1998).
5. M. Brust, M. Walker, D. Bethell, D.J. Schiffrin, and R. Whyman, *J. Chem. Soc. Chem. Commun.*, 801-2 (1994).
6. M.J. Hostetler, J.E. Wingate, C.-J. Zhong, J.E. Harris, R.W. Hachet, M.R. Clark, D.J. Londono, S.J. Green, J.F. Stokes, G.D. Wignall, G.L. Glish, M.D. Porter, N.D. Evans, and R.W. Murray, *Langmuir*, **14**, 17-30 (1998); A.W. Snow and H. Wohltjen, *Chem. Mater.*, **10**, 947-949 (1998).
7. A.W. Snow, W.R. Barger and J.P. Armistead, *32nd Middle Atlantic Regional ACS Meeting*, **32**, 59 (1999).

Room Temperature Single Electron Charging in Gold Nanoparticle Networks Formed on Biopolymer Templates

M.N. Wybourne, L. Clarke[†], C.A. Berven, J.E. Hutchison¹, L.O. Brown¹ and J.L. Mooster¹

Department of Physics and Astronomy, Dartmouth College
Hanover, NH 03755, U.S.A.

¹Department of Chemistry, University of Oregon
Eugene, OR 97403, U.S.A.

ABSTRACT

We report the current-voltage characteristics of gold nanoparticle – biopolymer networks at room temperature. Above a threshold voltage the current-voltage relationship is almost linear. From the current-voltage scaling above threshold we argue that one-dimensional regions of the network dominate the transport. Periodic features in the conductance are found in many samples. Both the threshold voltage and the conductance features occur at voltages much greater than expected for the capacitance of the nanoparticles. Possible explanations for the structure are considered.

INTRODUCTION

It has been recognized that ligand-stabilized metal nanoparticles are well suited to the investigation of single electron charging effects.[1-5] By virtue of their low capacitance, nanoparticles of less than about one hundred atoms have a Coulomb charging energy that is at least an order of magnitude greater than the thermal energy ($k_B T$) at room temperature.[6] Experiments have confirmed that nanoparticles of this size can support single electron charging effects at 300 K, with the ligand shell forming a tunnel barrier of resistance greater than the resistance quantum.[7, 8] In addition to providing electrical isolation, the ligand shell can be chemically modified to facilitate coupling between nanoparticles or attachment to other molecules.[9]

We present transport measurements on metal nanoparticle arrays made by casting a film of the rigid biopolymer poly-L-lysine onto metal electrodes with subsequent exposure to 11-mercaptopoundecanoic acid stabilized gold nanoparticles. In principle, a network of nanoparticles is formed when they are attached to the rigid biopolymer through the interaction between the ligand shell acid groups and the biopolymer amine groups. The room temperature current-voltage (I-V) characteristics of all such samples show a distinct Coulomb gap at low bias voltages. In some samples current plateaus were observed at voltages above threshold. These features are similar to those associated with single electron effects,[10-15] but what is striking is the fact that the magnitude of the threshold voltage and the plateau structure is at least an order of magnitude greater than values reported in other quantum dot or mesoscopic samples.

EXPERIMENTAL DETAILS

The poly-L-lysine - 11-mercaptopoundecanoic acid stabilized gold nanoparticle system was fabricated on interdigitated gold electrodes deposited on glass. An electrode spacing of 15 μm was used. The samples were prepared as follows. First, a

2.2×10^{-5} mol/l solution of poly-L-lysine-hydrobromide complex (54,000 amu) in 10/90% water/methanol was drop cast onto the electrodes that had been pre-cleaned using a UV/ozone dry process followed by a rinse in nanopure water. The hydrobromide was removed from the amine side chains of the biopolymer by submerging the cast film in a solution of 1% sodium hydroxide in water for about 20 hr. The 11-mercaptoundecanoic acid stabilized gold nanoparticles were synthesized from Schmid-Au₅₅ nanoparticles[16] using ligand exchange.[9] TEM measurements showed that the radius of the metal core was 0.7 nm, with a variance of $\pm 20\%$. The radius of the core and ligand shell together is estimated to be 2.1 nm. Nanoparticle decoration of the biopolymer was accomplished by placing a concentrated solution of the nanoparticles in dimethylsulfoxide onto the poly-L-lysine film for about 20 minutes, after which it was rinsed in dimethylsulfoxide and then dichloromethane. From the molecular weight, the average length of the poly-L-lysine is about 30 nm. Each polymer can therefore accommodate a maximum of approximately seven nanoparticles.

Current-voltage measurements were made in an electrically shielded vacuum chamber at room temperature.[3] Radio frequency (RF) electric fields could be applied by means of a dipole antenna placed close to the sample. Control I-V measurements were made at many stages of sample preparation.

DISCUSSION

Representative room temperature I-V behavior of the biopolymer - nanoparticle samples is shown in figure 1. All of the samples studied had non-linear I-V characteristics, with some having structure that was equally spaced in voltage. Control experiments showed that the I-V characteristics of the undecorated biopolymer had no structure and was almost indistinguishable from the behavior of the cleaned interdigitated electrodes.

The structure is more easily seen in the conductance, as shown in figure 2. After subtraction of the measured conductance at zero bias, the I-V relationship is seen to

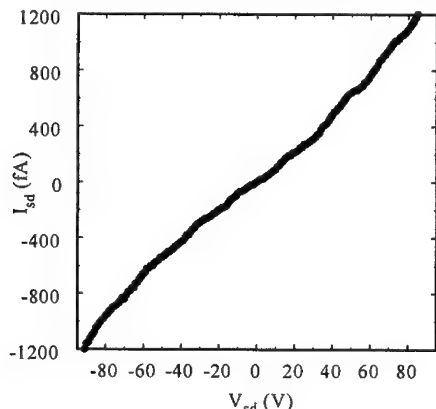


Figure 1. The I-V characteristic of a poly-L-lysine-nanoparticle sample.

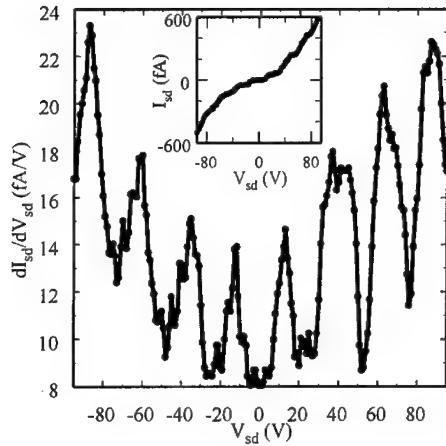


Figure 2. Conductance features as a function of applied voltage. The inset shows the original I-V data with the measured conductance at zero bias removed.

exhibit threshold behavior and current plateaus reminiscent of single electron behavior, as shown in the inset to figure 2. The threshold voltage V_T varied from sample to sample.

For the data shown in figure 2, V_T is 12 ± 1 V and the conductance oscillations have a spacing of $\Delta V = 25 \pm 3$ V. In general, for samples that show conductance oscillations the ratio $\Delta V/V_T$ was close to two. Above threshold, the scaling

$$I \propto (V/V_T - 1)^\gamma \quad (1)$$

was found to describe all sets of data, with $\gamma = 1.2 \pm 0.2$, as illustrated in figure 3. Here the error includes the uncertainty in the current measurement and the spread between different samples. The almost linear relationship between the current and voltage above threshold is unlike the quadratic dependence found in two-dimensional films containing gold nanoparticles.[3,7,8] It is much closer to the predictions of single electron transport in both ordered and disordered one-dimensional systems[17,18], where $\gamma \sim 1$. It is also consistent with the value $\gamma = 1.36 \pm 0.1$ obtained from experiments on one-dimensional chains of tunnel junctions.[19] Another difference between the present samples and thin films is the structure above threshold. Single electron systems are well known to be extremely sensitive to the RF environment. RF induced plateaus that are related to coherent transport effects have been reported in films containing gold nanoparticles.[3] To test the possibility that residual RF was causing the conductance structure, we introduced RF with frequencies below $0.1/R_T C$, where R_T is the tunnel resistance and C is the effective capacitance of a nanoparticle. No change in the structure was observed from which we conclude that RF induced coherent transport is not responsible for the conductance behavior.

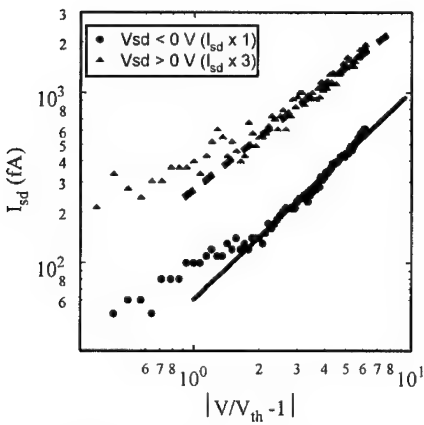


Figure 3. Current as a function of scaled voltage. The solid circles (triangles) are for negative (positive) bias voltages. For clarity, the current values for positive bias have been multiplied by 3. The solid and dash lines are least squares fits to the data and have slopes of 1.2 and 1.0, respectively.

While the threshold behavior and conductance oscillations suggest Coulomb blockade behavior, the voltage scales are considerably larger than normally found in such systems. The I-V scaling above threshold, and the fact that $\Delta V/V_T \sim 2$ suggest that regions of ordered, one-dimensional morphology are responsible for the features observed. Conventional Coulomb staircase phenomena have been reported at 287 K in long chains of small particles.[12] In the present samples, the nanoparticles are expected to be distant from a ground plane. Therefore, the capacitance to ground will be dominated by the geometry of the metal core, which we take to be a sphere of radius 0.7 nm. Taking the dielectric constant of the ligand shell to be 3, the capacitance to ground is estimated to be $C_g = 1.4 \times 10^{-1}$ aF. For a linear chain of identical, close-packed nanoparticles whose centers are separated by twice the radius of the gold core plus ligand shell (4.2 nm), the inter-particle capacitance is calculated to be $C_{dd} = 2.3 \times 10^{-2}$ aF. Using these capacitance values in the conventional Coulomb blockade model[18] we find the threshold voltage $V_T = 0.5$ V and the conductance periodicity $\Delta V \sim 1$ V, which are over an order of magnitude smaller than the measured values. Assuming the geometrical model for capacitance holds, reducing the physical size of the nanoparticles is unable to account for the differences since it would require unrealistically small particles.

The voltage scale discrepancy may be explained if the biopolymer-nanoparticle network contains sections that are not in Coulomb-blockade. These sections could form a bias network for those in blockade, thus reducing the voltage across each section in blockade. The idea that parts of the network are not in blockade seems reasonable since they may form poor conducting paths between the electrodes that contribute to the background conductance. The weakly conducting sections could be the result of either gold particles that have lost their ligand shell during sample preparation or regions in which the capacitance of the particles is increased. The size of the electrodes will

provide a considerable amount of spatial averaging over the network. Therefore, if this explanation is correct it suggests that the conductance oscillations are insensitive to the local arrangement of the poly-L-lysine network, implying that their origin must be related to a parameter that has a high degree of uniformity, such as the length (molecular weight) of the poly-L-lysine, or the size (capacitance) of the nanoparticles.

Quantum size effects can also produce conductance structure via resonant tunneling.[20] Optical studies of ligand-protected clusters with similar sizes to those used here have reported level structure with spacings of 600 and 900 meV.[21] Quantum size effects are highly dependent on the nature of the nanoparticles[22] and the ligand shell. The voltage scale of the conductance oscillations, and the energy scale of the level structure indicate that many nanoparticles would be involved, which suggests a low probability of finding regularly spaced structure. Therefore, we believe this explanation is unlikely in the present samples. However, quantum size effects cannot be ruled out completely. Work is continuing to understand the origin of the structure observed in these samples.

CONCLUSIONS

In summary, we have measured the room temperature transport in a biopolymer - nanoparticle system. The current-voltage characteristics are consistent with Coulomb-blockade effects. The almost linear relationship between current and voltage above threshold, the structure that is equally spaced in voltage and the observation that $\Delta V/V_T \sim 2$ is different to the behavior reported for thin film samples that do not contain the biopolymer template. These observations support the idea that the poly-L-lysine molecules act as a one-dimensional template for the gold nanoparticles. While the origin of the conductance behavior is unknown, the experiments indicate that the origin is insensitive to the local arrangement of the network, which implies that it must be related to a narrowly dispersed parameter of the system.

ACKNOWLEDGEMENTS

This work was supported in part by the Office of Naval Research and the National Science Foundation (DMR-9705343).

[†] Present address: Dept. of Physics, University of Colorado at Boulder, Boulder, CO.

REFERENCES

1. G. Schön and U. Simon, *Colloid. Polym. Sci.*, **273**, 202 (1995)
2. D.L. Feldheim and C.D. Keating, *Chem. Soc. Rev.*, **27**, 1 (1998)
3. L. Clarke, M.N. Wybourne, M. Yan, S.X. Cai, and J.F.W. Keana, *Appl. Phys. Lett.*, **71**, 617 (1997)
4. R.P. Andres, J. D. Beielefeld, J. I. Henderson, D. B. Janes, V. R. Kolagunta, C. P. Kubiak, W. J. Mahoney, and R. G. Osifchin, *Science*, **273**, 1690 (1996)
5. T. Sato, H. Ahmed, D. Brown, and B.F.G. Johnson, *J. Appl. Phys.*, **82**, 696 (1997)
6. R.P. Andres, T. Bein, M. Dorogi, S. Feng, J.I. Henderson, C.P. Kubiak, W. Mahoney, R.G. Osifchin, and R. Reisenberger, *Science*, **272**, 1323 (1996)

7. L. Clarke, M.N. Wybourne, M. Yan, S.X. Cai, L.O. Brown, J. Hutchison, and J.F.W Keana, *J. Vac. Sci. Technol. B*, **15**, 2925 (1997)
8. M.N. Wybourne, J.E. Hutchison, L. Clarke, L.O. Brown, and J.L. Mooster, *Microelec. Eng.*, **47**, 55 (1999)
9. L.O. Brown and J. E. Hutchison, *J. Am. Chem. Soc.*, **119**, 12,384 (1997)
10. D.V. Averin and K.K. Likharev, in *Mesoscopic Phenomena in Solids*, edited by B. Al'tshuler, P. Lee, and R.A. Webb (Elsevier, Amsterdam 1991)
11. N.S. Bakhvolov, G.S. Kazacha, K.K. Likharev, and S.I. Serdyukova, *Sov. Phys. JETP*, **68**, 581 (1989)
12. K. Kawasaki, M. Mochizuki, and K. Tsutsui, *Jpn. J. Appl. Phys.*, **38**, 418 (1999)
13. L.Y. Gorelik, A. Isacsson, M.V. Voinova, B. Kasemo, R.I. Shekter and M. Jonson, *Phys. Rev. Lett.*, **80**, 4526 (1998), A. Isacsson, L.Y. Gorelik, M.V. Voinova, B. Kasemo, R.I. Shekter, and M. Jonson, *Physica B*, **255**, 150 (1998)
14. M. Shin, S. Lee, K.W. Park, and E. Lee, *Phys. Rev. Lett.*, **80**, 5774 (1998)
15. D.C. Ralph, C.T. Black, and M. Tinkham, *Phys. Rev. Lett.*, **74**, 3241 (1995). M. Tinkham, *Am. J. Phys.*, **64**, 343 (1996)
16. G. Schmid, *Inorg. Synth.*, **27**, 214 (1990)
17. A.A. Middleton and N.S. Wingreen, *Phys. Rev. Lett.*, **71**, 3198 (1993)
18. G.Y. Hu and R.F. O'Connell, *Phys. Rev. B*, **49**, 16773 (1994)
19. A.J. Rimberg, T.R. Ho, and J. Clarke, *Phys. Phys. Rev. Lett.*, **74**, 4714 (1995)
20. D.C. Ralph, C.T. Black and M. Tinkham, *Phys. Rev. Lett.*, **74**, 3241 (1995)
21. S. Chen, R.S. Ingram, M.J. Hostetler, J.J. Pietron, R.W. Murray, T.G. Schaaff, J.T. Khouri, M.M. Alvarez, and R.L. Whetton, *Science*, **280**, 2098 (1998)
22. O.D. Häberlen, S.C. Chung, M. Stener, and N. Rösch, *J. Chem. Phys.*, **106** 5189 (1997)

AUTHOR INDEX

Allara, D.L., H9.2
Ancona, M.G., H12.5
Atwater, H.H., H10.5

Bawendi, M.G., H2.4
Belomoin, G., H11.4
Bennati, M., H2.4
Berven, C.A., H13.4
Boos, J.B., H12.5
Brongersma, M.L., H10.5
Brown, L.O., H11.1, H13.4
Bumm, L.A., H9.2
Burgin, T.P., H9.2

Chen, J., H3.2, H9.2
Clarke, L.I., H11.1, H13.4
Cronin, S.B., H10.3, H10.4
Cygan, M.T., H9.2

Deshpande, M.R., H9.2
Di Ventra, M., H3.3
Doty, R.C., H2.5
Dresselhaus, M.S., H10.3, H10.4
Dunbar, T.D., H9.2

Ebata, K., H10.2

Fujiki, M., H10.2
Furukawa, K., H10.2

Griffin, R.G., H2.4

Hall, D.A., H2.4
Hartman, J.W., H10.5
Hayashi, N., H6.4
Holmes, J.D., H2.5
Hutchison, J.E., H11.1, H13.4

Ishii, H., H6.4
Ito, E., H6.4

Jernigan, G.G., H12.5
Johnston, K.P., H2.5

Jones II, L., H9.2

Koga, T., H10.4
Korgel, B.A., H2.5
Kozaki, M., H9.2
Kruppa, W., H12.5
Kuno, M., H2.4

Lang, N.D., H3.3
Lin, Y.M., H10.3, H10.4

Metzger, R.M., H12.2
Mickelson, E.T., H9.2
Mikulec, F.V., H2.4
Mooster, J.L., H11.1, H13.4
Muller, C.J., H9.2

Nayfeh, M.H., H11.4

Oji, H., H6.4
Ouchi, Y., H6.4

Pantelides, S.T., H3.3
Park, D., H12.5
Price, D.W., H3.2

Rawlett, A.M., H3.2, H9.2
Reed, M.A., H3.2, H9.2
Reed, S.M., H11.1
Reinerth, W.A., H9.2

Schmidt, M.E., H11.1
Seki, K., H6.4
Snow, A.W., H12.5
Sun, X., H10.3

Therrien, J.M., H11.4
Tour, J.M., H3.2, H9.2

Wang, W., H3.2
Weiss, P.S., H9.2
Wybourne, M.N., H11.1, H13.4

Ying, J.Y., H10.3, H10.4
Yoshimura, D., H6.4

Zhou, C-W., H9.2
Ziegler, K.J., H2.5

Zhang, Z., H10.3

SUBJECT INDEX

- alumina, H10.3
- anodic, H10.3
- atomic contacts, H3.3
- band bending, H6.4
- Bi nanowires transport low dimensional, H10.4
- blue luminescence, H2.5
- CdMnSe, H2.4
- coherent transport, H10.5
- colloid, H2.4
- contact engineering, H3.3
- coulomb blockade, H11.1, H13.4
- deposition, H12.5
- dilute magnetic semiconductor, H2.4
- electroluminescence, H5.2
- energy level alignment, H6.4
- high speed, H10.5
- interfacial dipole, H6.4
- I-V spectrum, H11.4
- light emission, H5.2
- molecular electronics, H3.2
- switch, H3.2
- nanocluster(s), H12.5, H13.4
- nanocrystal(s), H2.5, H11.4
- nanodevices, H12.2
- nanoelectronics, H11.1
- nanostructures, H13.4
- one dimensional, H10.3
- photoemission, H6.4
- photonic device, H10.5
- plasmon, H10.5
- polysilane, H10.2
- quantum confinement, H2.5
- dot, H2.4
- rectifiers, H12.2
- resonant energy transfer, H10.5
- self-assembled monolayer, H3.2
- self-assembly, H2.5, H11.1, H12.5
- semiconductor clusters, H2.5
- semiflexible polymer, H10.2
- silicon, H11.4
- single electron, H11.4
- polymer, H10.2
- TOPO, H2.4
- transport, H12.5
- theory, H3.3
- tunneling electrons, H5.2
- unimolecular devices, H12.2
- work function, H6.4